# Toward a global search for new physics with isotope shifts

Elina Fuchs [*]
*Deutsches Elektronen-Synchrotron DESY, Notkestr. 85, 22607 Hamburg, Germany;*
*Institut für Theoretische Physik, Leibniz Universität Hannover, Appelstraße 2, 30167 Hannover, Germany;*
*and Physikalisch-Technische Bundesanstalt, Bundesallee 100, 38116 Braunschweig, Germany*

Fiona Kirk [†]
*Physikalisch-Technische Bundesanstalt, Bundesallee 100, 38116 Braunschweig, Germany*
*and Institut für Theoretische Physik, Leibniz Universität Hannover, Appelstraße 2, 30167 Hannover, Germany*

Agnese Mariotti [‡]
*Institut für Theoretische Physik, Leibniz Universität Hannover, Appelstraße 2, 30167 Hannover, Germany*

Jan Richter [§]
*Physikalisch-Technische Bundesanstalt, Bundesallee 100, 38116 Braunschweig, Germany*
*and Institut für Theoretische Physik, Leibniz Universität Hannover, Appelstraße 2, 30167 Hannover, Germany*

Matteo Robbiati [‖]
*Dipartimento di Fisica, Università degli Studi di Milano, Italy*
*and European Organization for Nuclear Research (CERN), Geneva 1211, Switzerland*

(Received 16 July 2025; accepted 23 October 2025; published 25 November 2025)

Isotope shifts have emerged as a sensitive probe of new bosons that couple to electrons and neutrons, and of nuclear structure. The recent Hz- or even sub-Hz-level isotope shift measurements across different elements call for a global assessment of all available data. In this work, we present the fit framework KIFIT that enables a combined analysis of isotope shift data from several elements, taking into account correlations. We provide a thorough comparison of analytical methods and the fit to analyze linear and nonlinear King plots and quantify their uncertainties. Finally, we provide recommendations for future measurements that could enhance the sensitivity to new physics and offer new insights into nuclear structure.

DOI: 10.1103/kzq9-x916

## I. INTRODUCTION

Atomic precision spectroscopy has emerged as a powerful tool for probing the standard model of particle physics (SM) and its extensions, which address long-standing questions such as the properties of dark matter [1–3]. The groundbreaking developments of laser cooling [4–7], optical frequency combs [8,9], optical tweezers [10–12], optical lattices [13–16] and quantum logic spectroscopy [17–20] have increased the relative precision of optical atomic clocks to the level of $10^{-18}$ [21,22]. As a result of this unparalleled precision, clock comparisons and other differential spectroscopic measurements probe relevant parts of the parameter space of light dark matter and dark portal models.

A prime example for such developments is isotope-shift spectroscopy, a well-established technique commonly used to determine nuclear charge radii [23–27], but more recently proposed as a method to search for hypothetical new bosons mediating an additional interaction between neutrons and electrons [28,29]. Isotope shifts can probe bosons in the eV to MeV mass range, allowing them to bridge the gap between fifth force searches via the Casimir effect [30], beam dump experiments [31–33], and searches for exotic meson decays at colliders [34,35]. New vector or scalar bosons, such as the ones probed by isotope shift spectroscopy [36], are predicted by a wide range of extensions of the SM. These include models that gauge baryon minus lepton number ($B - L$), which result in a new vector boson $Z'$, or so-called portal models that introduce new light scalar or vector mediators between the SM and dark matter [37].

The new physics search proposed in Refs. [28,29] is based on the so-called King plot method [23,24], which at leading order predicts a linear relation between isotope shifts in different electronic transitions. Using King plots reduces the reliance on atomic structure calculations, which are

[*]Contact author: elina.fuchs@itp.uni-hannover.de
[†]Contact author: fiona.kirk@itp.uni-hannover.de
[‡]Contact author: agnese.mariotti@itp.uni-hannover.de
[§]Contact author: jan.richter@ptb.de
[‖]Contact author: matteo.robbiati@cern.ch

limited in precision by nonperturbative and many-body effects, particularly within the nucleus. This approach allows new physics signals to be constrained using isotope shift data.

Given the long history of remarkably linear King plots, King plot searches for new physics attracted a lot of attention and significant progress was made in improving the precision of the isotope shift and nuclear mass measurements, with notable advancements in neutral Ca [38,39], $Ca^+$ [26,40–43] and $Ca^{14+}$ [43], as well as in neutral Yb [44–47] and $Yb^+$ [48–50]. The first observation of a nonlinear King plot was reported in Ref. [48], which employed the $^2S_{1/2} \to {}^2D_{3/2}$ vs $^2S_{1/2} \to {}^2D_{5/2}$ transitions in $Yb^+$, measured at a precision of about 300 Hz. This so-called "King nonlinearity" was confirmed by subsequent measurements [49,50] and is currently found to be at the level of 20.17(2) kHz [50]. Recently, nonlinear isotope shifts have also been observed in the $^3P_0 \to {}^3P_1$ transition, measured at sub-Hz precision in $Ca^{14+}$, and in the $^2S_{1/2} \to {}^2D_{5/2}$ transition, measured in $Ca^+$, combined with nuclear mass ratios with relative uncertainties below $4 \times 10^{-11}$ [43].

Although the presence of nonlinearities complicates King plot searches for new physics, it is by no means a showstopper: Progress in atomic and nuclear structure theory has facilitated the identification of the leading higher-order effects in Yb [49–51] and in Ca King plots [43,52], whereas the development of the generalized King plot [53] showed that the data-driven King plot approach can be generalized so as to provide constraints on new physics, even in the presence of higher-order nuclear effects. For a recent review of the relevance of (nonlinear) King plots for the search for new (nuclear) physics, see Ref. [54].

The King plot analysis is often restricted to even isotopes to avoid the effects of the nuclear spin, namely, hyperfine interactions, which are expected to introduce additional nonlinear effects in the King plot [55]. Reference [56] discusses the challenges associated with using odd Yb isotopes in King plot analyses. Another example is provided by Refs. [57,58]: although the King plots for Cd and Zn are linear, the hyperfine interactions would potentially be observable at Hz precision.

With a wealth of high-precision isotope shift data now available for different elements and charged states, a systematic approach is needed to assess the constraints on new physics contributions, which are expected to be governed by the same couplings to electrons and to neutrons, irrespective of the element under consideration. In this work, we first review the (generalized) King plot [29,53], the no-mass (generalized) King plot [53] and the projection [41] methods, which follow a purely algebraic approach (Sec. II), before presenting our code KIFIT, which provides a framework to combine all linear King plots across elements in one global constraint on new physics (Sec. III). The framework provided by KIFIT is based on the fit presented in Ref. [36] but was significantly extended to handle contemporary high-precision isotope shift data. KIFIT performs a fit to linear King plots plus new physics, while the incorporation of higher-order nuclear effects, which would be necessary to analyze nonlinear King plots, is left to future work. Nonetheless, KIFIT presents an important step toward a global view of isotope shift data. In Sec. IV we compare KIFIT with the algebraic methods introduced in Sec. II, before concluding in Sec. V. In the Appendixes we provide further details on the electronic structure calculations with AMBiT [59] (Appendix A), how the choice of transitions used in King plots affects the sensitivity to new physics (Appendix B), the impact of experimental uncertainties on the margin for new physics (Appendix C), a short manual for our code KIFIT and a list of implemented validation checks (Appendix D), an analysis of the impact of data sparsity on the fit (Appendix E), as well as a summary of the available state-of-the-art isotope shift data and isotope masses (Appendix F).

## II. SEARCHING FOR NEW PHYSICS WITH KING PLOTS

An isotope shift $\nu_i^{AA'} \equiv \nu_i^A - \nu_i^{A'}$ corresponds to the frequency difference between the electronic transition $i$ measured in isotopes $A$ and $A'$. Isotope shifts are dominated by two effects, both of which can be described by a product of an electronic coefficient ($K_i$, $F_i$) and a nuclear quantity ($\mu^{AA'}$, $\delta\langle r^2\rangle^{AA'}$), respectively [23,60–62],

$$\nu_i^{AA'} \approx K_i \mu^{AA'} + F_i \delta\langle r^2\rangle^{AA'}. \tag{1}$$

The first term in Eq. (1), which is proportional to the difference of inverse nuclear masses,[1] $\mu^{AA'} \equiv \frac{1}{m^A} - \frac{1}{m^{A'}}$, is known as the first-order *mass shift* (MS) and describes the nuclear-recoil correction to the electron kinetic energy [63]. The second term, referred to as the first-order *field shift* (FS), accounts for the nuclear charge radius variance $\delta\langle r^2\rangle^{AA'} \equiv \langle r^2\rangle^A - \langle r^2\rangle^{A'}$ and describes the energy shift due to changes in the nuclear charge distribution between the different isotopes [64].

Since we will mostly be dealing with isotope pairs in the following, we introduce the isotope pair index $a = AA'$.

Thanks to the factorization of the isotope shifts into electronic and nuclear quantities at leading order, we can combine isotope shift measurements for two different transitions to eliminate the nuclear charge radius, which is neither experimentally nor theoretically precisely determined [23,65]. We obtain a linear relation between the isotope shifts of the two transitions labeled 1 and 2 [23],[2]

$$\tilde{\nu}_2^a|_{\text{lin.}} = K_{21} + F_{21}\tilde{\nu}_1^a, \tag{3}$$

where we defined the so-called mass-normalized isotope shifts [62,66,67] $\tilde{\nu}_i^a \equiv \frac{\nu_i^a}{\mu^a}$ and introduced the electronic

[1]The measured mass $m^{A^0}$ of a neutral atom $A^0$ can be translated into a nuclear mass $m^A$ by subtracting the masses $m_e$ and binding energies $E_i^b$ of the $N_e$ electrons [41]:

$$m^A = m^{A^0} - N_e m_e + \sum_{i=1}^{N_e} E_i^b.$$

[2]Instead of the mass-normalized isotope shifts in Eq. (3), it is possible to normalize the isotope shifts by those of the reference transition $\nu_1^a$. The King relation for *frequency-normalized* isotope shifts takes the form

$$\bar{\nu}_2^a \equiv \frac{\nu_2^a}{\nu_1^a} = F_{21} + K_{21}\bar{\mu}^a, \tag{2}$$

where $\bar{\mu}^a \equiv \mu^a/\nu_1^a$, while the electronic coefficients appear in the same combinations as in Eq. (4).

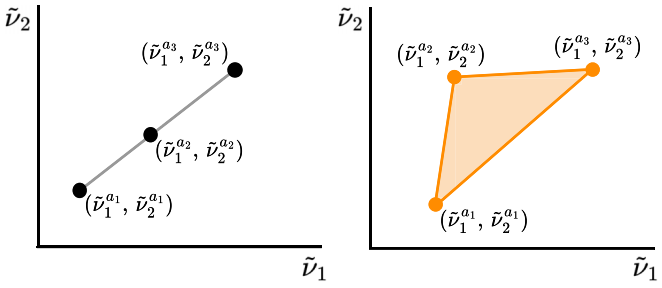


FIG. 1. (left) Linear two-dimensional King plot. The isotope shifts follow the relation given in Eq. (1). (right) In the presence of higher-order nuclear or new physics contributions to the isotope shifts, the data points deviate from the King line and define a nonzero volume.

coefficients

$$F_{21} \equiv \frac{F_2}{F_1}, \quad K_{21} \equiv K_2 - F_{21} K_1. \tag{4}$$

The subscript "lin." indicates that Eq. (3) only describes the leading linear behavior.

If multiple isotope pairs ($a = 1, \ldots, n$) can be probed, it is useful to arrange the isotope shifts $\tilde{\nu}_i^a$, $i = 1, 2$, into vectors in isotope-pair space. Defining the $n$-vectors $\tilde{\boldsymbol{\nu}}_i = (\tilde{\nu}_i^1, \ldots, \tilde{\nu}_i^n)$ and $\mathbf{1} = (1, \ldots, 1)$, one obtains

$$\tilde{\boldsymbol{\nu}}_2|_{\text{lin.}} = K_{21}\mathbf{1} + F_{21}\tilde{\boldsymbol{\nu}}_1. \tag{5}$$

Equation (5) can be visualized in a so-called King plot [23], illustrated in the left half of Fig. 1. The electronic coefficients $K_{21}$ and $F_{21}$, corresponding to the intercept and slope of the *King line*, can be determined via a linear fit to the isotope shift data. Alternatively, the isotope shift data can be arranged in isotope pair space. Figure 2 shows the *plane of King linearity*, which is spanned by the vectors $\mathbf{1}$ and $\tilde{\boldsymbol{\nu}}_1$. If $\tilde{\boldsymbol{\nu}}_2$ is described by Eq. (5), it will lie in this plane.

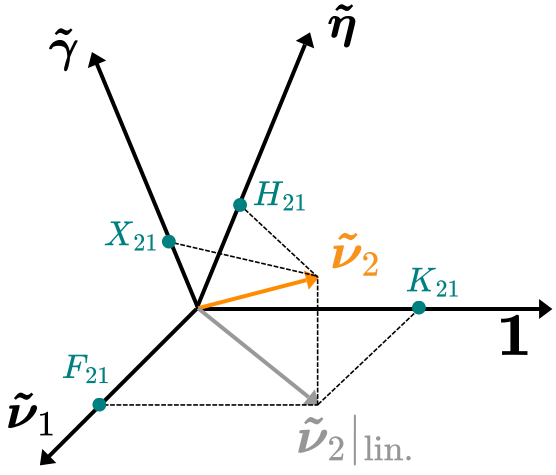


FIG. 2. Illustration of the "King plane" spanned by the vectors $\boldsymbol{\nu}_1$ and $\mathbf{1}$ in isotope pair space. If Eq. (5) holds, $\boldsymbol{\nu}_2$ lies in this plane, while a nonlinearity in the King plot would lead to an out-of-plane component for $\boldsymbol{\nu}_2$. Both new physics, here assumed to be proportional to $\tilde{\boldsymbol{\gamma}}$, and higher-order SM terms, represented by the vector $\tilde{\boldsymbol{\eta}}$ [see Eq. (22)], can lead to this kind of effect.

### A. Algebraic methods for linear King plots

In the following, we distinguish linear and nonlinear King plots. As King nonlinearities, we understand any deviation from the linear King relation in Eq. (5). As long as these are smaller or comparable to the experimental uncertainties, the King plot is considered linear.

Nonlinearities may be caused by higher-order nuclear or electronic corrections, or by new physics contributions. As long as the higher-order SM contributions are negligible or can be determined by additional experimental and theoretical input, King plots can be used to place constraints on the mass and couplings of a new boson $\phi$ inducing a new interaction between the bound electrons and the neutrons inside the nucleus [29]. Assuming $\phi$ couples linearly to neutrons and electrons, this effect can be described by a Yukawa potential [28,68]

$$V_{\text{NP}}(r, m_\phi) = -\alpha_{\text{NP}}(A - Z)\frac{e^{-m_\phi r}}{r}, \tag{6}$$

expressed here in relativistic units ($c = \hbar = 1$). Here, $\alpha_{\text{NP}} = (-1)^s \frac{y_e y_n}{4\pi}$ is defined as the product of the new physics couplings to electrons ($y_e$) and to neutrons ($y_n$), while $s = 0, 1, 2$ denotes the spin, $m_\phi$ corresponds to the mass of the new light boson $\phi$, and $A$ and $Z$ are respectively the mass and atomic numbers of the considered isotope. This introduces a new term in the isotope shifts [29]

$$\nu_i^a\big|_{\text{pred.}} = K_i \mu^a + F_i \delta\langle r^2\rangle^a + \frac{\alpha_{\text{NP}}}{\alpha_{\text{EM}}} X_i \gamma^a, \tag{7}$$

where we introduced the subscript "pred" to indicate the predicted isotope shift in the presence of new physics. Assuming a linear King plot, we can use Eq. (7) to set a bound on the new physics coupling $\alpha_{\text{NP}}$, expressed in units of the fine-structure constant $\alpha_{\text{EM}}$.[3] The factor $\gamma^a \equiv A - A'$ is the difference in neutron number between the isotopes $A$ and $A'$, while the electronic coefficients $X_i$ quantify the sensitivity of the transition frequency $\nu_i$ to shifts induced by the new physics potential in Eq. (6). The leading behavior can be understood in a perturbative approach, in which the radial wave functions $\Psi_i^{\text{init,fin}}(r)$ of the states involved in the transition $i$ are assumed to be unchanged compared with the SM. In this case, the coefficient $X_i$ corresponds to the difference between the overlap of the new physics potential [Eq. (6)] with the final- and initial-state wave functions:

$$X_i(m_\phi) = \int \frac{e^{-m_\phi r}}{r}\left[\left|\Psi_i^{\text{fin}}(r)\right|^2 - \left|\Psi_i^{\text{init}}(r)\right|^2\right]\mathrm{d}r. \tag{8}$$

The overlap with the new physics potential is particularly pronounced for $S$-state wave functions. Consequently, narrow transitions involving $S$ states are favorable for isotope-shift-based searches for new physics.

As discussed in Appendix A, for the numerical calculation of the new physics electronic coefficients, we follow Ref. [29] and use the public code AMBIT [59], which applies a nonperturbative finite field method that adds the new physics potential directly to the Hamiltonian in the Dirac equation.

[3]Note that alternative conventions exist in the literature. An equivalent relation in terms of $y_e y_n$ rather than $\alpha_{\text{NP}}/\alpha_{\text{EM}}$ can be obtained by rescaling the $X$ coefficients (see Appendix A).

Combining Eq. (7) for the transitions $i = 1, 2$, we obtain the modified King relation

$$\tilde{\boldsymbol{\nu}}_2|_{\text{pred.}} = K_{21}\mathbf{1} + F_{21}\tilde{\boldsymbol{\nu}}_1 + \frac{\alpha_{\text{NP}}}{\alpha_{\text{EM}}} X_{21}\tilde{\boldsymbol{\gamma}}, \tag{9}$$

where we defined $X_{21} \equiv X_2 - F_{21}X_1$ and $\tilde{\boldsymbol{\gamma}}$ with elements $\tilde{\gamma}^a \equiv \frac{\gamma^a}{\mu^a}$. Equation (9) implies that $\tilde{\boldsymbol{\nu}}_2|_{\text{pred.}}$ has a component along $\tilde{\boldsymbol{\gamma}}$, which pushes it out of the King plane, as visualized in Fig. 2.

If $n = 3$ isotope pairs are probed, the system of isotope-shift equations (9) can be solved for the new physics coupling [29]:

$$\frac{\alpha_{\text{NP}}}{\alpha_{\text{EM}}} = \frac{\det(\tilde{\boldsymbol{\nu}}_1, \tilde{\boldsymbol{\nu}}_2, \mathbf{1})}{\varepsilon_{ij}\det(X_i\tilde{\boldsymbol{\gamma}}, \tilde{\boldsymbol{\nu}}_j, \mathbf{1})} = \frac{\text{V}_{\text{dat}}}{\text{V}_{\text{pred}}}, \tag{10}$$

where $\varepsilon_{ij}$ is the two-dimensional Levi-Civita symbol and summation over repeated indices is implied. $\det(\mathbf{u}, \mathbf{v}, \mathbf{w})$ denotes the determinant of the square matrix whose columns are the vectors $\mathbf{u}$, $\mathbf{v}$, and $\mathbf{w}$. In the following, we refer to Eq. (10) as the *minimal King plot (KP)* formula.[4] Note that the normalization of the vectors entering Eq. (10) does not affect the result, meaning that $(\tilde{\boldsymbol{\nu}}_1, \tilde{\boldsymbol{\nu}}_2, \mathbf{1})$ can be replaced by $(\boldsymbol{\nu}_1, \boldsymbol{\nu}_2, \boldsymbol{\mu})$ or by frequency-normalized counterparts. Geometrically, $\text{V}_{\text{dat}}$ can be visualized either as the volume spanned by data points in the King plot (see Fig. 1) or as the volume of the parallelepiped spanned by $\tilde{\boldsymbol{\nu}}_1$, $\tilde{\boldsymbol{\nu}}_2$, and $\mathbf{1}$ (see Fig. 2). Similarly, $\text{V}_{\text{pred}}$ measures the predicted volume spanned by the data vectors in the presence of new physics contributions.

It is instructive to split $\text{V}_{\text{dat}}$ and $\text{V}_{\text{pred}}$ into their respective electronic and nuclear contributions. Assuming the isotope shifts satisfy Eq. (7) and defining

$$\mathcal{M} = \begin{pmatrix} X_1 & F_1 \\ X_2 & F_2 \end{pmatrix}, \quad \mathcal{N} = \begin{pmatrix} \tilde{\gamma}^1 & \delta\langle\widetilde{r^2}\rangle^1 & 1 \\ \tilde{\gamma}^2 & \delta\langle\widetilde{r^2}\rangle^2 & 1 \\ \tilde{\gamma}^3 & \delta\langle\widetilde{r^2}\rangle^3 & 1 \end{pmatrix}, \tag{11}$$

where $\delta\langle\widetilde{r^2}\rangle^a \equiv \delta\langle r^2\rangle^a/\mu^a$ denotes the mass-normalized charge radius variance, we can rewrite $\text{V}_{\text{pred}}$ as

$$\begin{aligned} \text{V}_{\text{pred}} &= \varepsilon_{ij}\det(X_i\tilde{\boldsymbol{\gamma}}, \tilde{\boldsymbol{\nu}}_j, \mathbf{1}) = \det(\mathcal{M})\det(\mathcal{N}) \\ &= (F_1X_2 - F_2X_1)\det(\tilde{\boldsymbol{\gamma}}, \boldsymbol{\delta\widetilde{\langle r^2\rangle}}, \mathbf{1}). \end{aligned} \tag{12}$$

This equation explicitly shows that King plots are sensitive to the new physics coupling when the nuclear and electronic quantities simultaneously "open up" new dimensions in isotope-pair space and in transition space.

The solution of $\alpha_{\text{NP}}$ in Eq. (10) corresponds to the value of the coupling required to reproduce the central values of the King plot points $\tilde{\nu}_i^a$, $i = 1, 2$, $a = 1, 2, 3$. However, the King plot method cannot exclude higher-order SM contributions to the isotope shifts and thus cannot identify an observed nonlinearity as being purely of new physics origin. In other words, it is not a discovery tool but can only be used to set bounds on the coupling $\alpha_{\text{NP}}$. The $N\sigma$ bounds on $\alpha_{\text{NP}}$ can be estimated as

$$\langle\alpha_{\text{NP}}\rangle + N\sigma[\alpha_{\text{NP}}]. \tag{13}$$

With $\langle\alpha_{\text{NP}}\rangle$ we denote the absolute value of $\alpha_{\text{NP}}$ obtained for the experimental central values of the input parameters (isotope shifts $\nu_i^a$ and nuclear masses $m^A$). The uncertainty on $\alpha_{\text{NP}}$, $\sigma[\alpha_{\text{NP}}]$, can either be estimated using (linear) error propagation or with a Monte Carlo approach. The latter involves the generation of samples[5] of the input parameters from a normal distribution fixed by the respective experimental central values and uncertainties:

$$\nu_i^a \sim \mathcal{N}\left(\langle\nu_i^a\rangle, \sigma\left[\nu_i^a\right]\right), \quad m^A \sim \mathcal{N}(\langle m^A\rangle, \sigma[m^A]) \tag{14}$$

and similarly for the reference isotope masses $m^{A'}$. Then, $\sigma[\alpha_{\text{NP}}]$ is estimated as the standard deviation of the corresponding $\alpha_{\text{NP}}$ values. In this case, one should pay attention to whether the distribution of the $\alpha_{\text{NP}}$ values can be accurately described by a Gaussian.

As already discussed in Ref. [29], the $m_\phi$-range that King plots are particularly sensitive to is dictated by the $m_\phi$-dependence of the $X$ coefficients [see Eqs. (6) and (8) or Fig. 15]: In the *"massless" limit*, the Yukawa potential [Eq. (6)] takes the form $V_{\text{NP}} \propto 1/r$ and the electronic coefficients $X$, and consequently the bounds on $\alpha_{\text{NP}}$, become independent of $m_\phi$ [see Figs. 15 and 16, respectively]. This corresponds to the case where the interaction range of the mediator $\phi$ [Compton wavelength $\lambda_\phi = h/(m_\phi c)$] exceeds the size of the atom or ion, and the overlap of the Yukawa potential with the electronic wave functions saturates at maximal King plot sensitivity to new physics.

In the *intermediate $m_\phi$ region*, the values of the $X$ coefficients are sensitive to the value of $m_\phi$ and the combination of electronic coefficients that enters $\text{V}_{\text{pred}}$ [see Eq. (12)] may cancel for specific values of $m_\phi$, leading to the characteristic peaks that are visible, e.g., in Fig. 16.

In the *large-$m_\phi$ limit,* the Yukawa potential can be approximated by $V_{\text{NP}} \propto \delta(r)/(m_\phi r)^2$. This limit corresponds to the case where the Compton wavelength of $\phi$ is smaller than the nuclear charge radius and the interaction mediated by $\phi$ becomes a contact interaction. In this case the King plot method is no longer able to distinguish the new physics shift from the field shift induced by changes in the nuclear radius. The $X$ coefficients align themselves with the electronic field shift coefficients[6] $F_i \propto |\Psi_i^{\text{fin}}(0)| - |\Psi_i^{\text{init}}(0)|$ in such a way that $X_i/X_j \to F_i/F_j$, and, consequently, the new physics parameters $\frac{\alpha_{\text{NP}}}{\alpha_{\text{EM}}}\gamma^a$ can no longer be distinguished from the charge radius variance $\delta\langle r^2\rangle^a$. The resulting suppression of the sensitivity to new physics can be observed, e.g., in Fig. 16.

In Appendix B, a King plot analysis is applied to selected transitions in $Ca^+$ to illustrate the behavior of the electronic

[4] In the `KIFIT` code, Eq. (10) corresponds to the three-dimensional case of the generalized King plot formula, presented in Sec. II B 2. Here, "three" refers to the number of isotope pairs, i.e., to the number of data points in the King plot.

[5] In the `KIFIT` code, the number of samples `num_det_samples` is a hyperparameter that can be set by the user.

[6] Note that uncertainties in the $X$ coefficients, which are predicted by means of atomic structure calculations, generally spoil this behavior. However, it can easily be restored by rescaling the $X_i$ coefficients in such a way that $X_i/X_j \to F_{ij}|_{\text{dat}}$, where $F_{ij}|_{\text{dat}}$ is the slope of best-fit line to the King plot data.

part of $V_{pred}$ across different transitions. Moreover, the impact of the uncertainties on the $X$ coefficients is briefly discussed therein.

#### *Additional algebraic methods*

For completeness, let us briefly introduce the *no-mass King plot* and the *projection method*, which provide alternatives to Eq. (10) that can be beneficial, respectively, in the case of large nuclear mass uncertainties and in the case of isotope shift datasets for two transitions but more than three isotope pairs.

*No-mass King plot.* The no-mass King plot (NMKP) uses isotope shift data not only to eliminate the charge radius variance $\delta\langle r^2\rangle$ from Eq. (7) but also the nuclear masses. This requires isotope shift measurements for an additional transition $\boldsymbol{\nu}_3$, yielding [53][7]

$$\frac{\alpha_{NP}}{\alpha_{EM}} = \frac{2\det(\boldsymbol{\nu}_1, \boldsymbol{\nu}_2, \boldsymbol{\nu}_3)}{\varepsilon_{ijk}\det(X_i\boldsymbol{\gamma}, \boldsymbol{\nu}_j, \boldsymbol{\nu}_k)}. \tag{15}$$

The denominator takes a particularly symmetric form in this case:

$$V_{pred} = \tfrac{1}{2}\varepsilon_{ijk}\det(X_i\boldsymbol{\gamma}, \boldsymbol{\nu}_j, \boldsymbol{\nu}_k) = \det(\mathcal{M})\det(\mathcal{N}), \tag{16}$$

with

$$\mathcal{M} = \begin{pmatrix} X_1 & K_1 & F_1 \\ X_2 & K_2 & F_2 \\ X_3 & K_3 & F_3 \end{pmatrix}, \quad \mathcal{N} = \begin{pmatrix} \gamma^1 & \mu^1 & \delta\langle r^2\rangle^1 \\ \gamma^2 & \mu^2 & \delta\langle r^2\rangle^2 \\ \gamma^3 & \mu^3 & \delta\langle r^2\rangle^3 \end{pmatrix}. \tag{17}$$

The no-mass King plot formula allows us to mitigate uncertainties on the nuclear masses when their effect on the uncertainty estimation in Eq. (13) dominates over that of the isotope shift uncertainties.

*Projection method.* The projection method presented in Ref. [41] yields a bound on new physics using isotope shift data for two transitions measured in $n$ isotope pairs. Introducing the $(n \times 2)$ matrix

$$D_{\mathbf{w}} \equiv (\tilde{\boldsymbol{\nu}}_1, \mathbf{w}), \tag{18}$$

where $\mathbf{w}$ is a generic $n$-vector in isotope-pair space, we can define the projection of the vector $\mathbf{1}$ on the plane spanned by the vectors $\tilde{\boldsymbol{\nu}}_1$ and $\mathbf{w}$ as

$$\mathbf{p}_{\mathbf{w}} = D_{\mathbf{w}}(D_{\mathbf{w}}^{\top}D_{\mathbf{w}})^{-1}D_{\mathbf{w}}^{\top}\mathbf{1}, \tag{19}$$

where $\top$ denotes the transpose. Then, $\alpha_{NP}$ can be expressed as

$$\left|\frac{\alpha_{NP}}{\alpha_{EM}}\right| = \frac{V(\mathbf{1}, \tilde{\boldsymbol{\nu}}_1, \tilde{\boldsymbol{\nu}}_2)}{|X_{21}|V(\mathbf{1}, \tilde{\boldsymbol{\nu}}_1, \tilde{\boldsymbol{\gamma}})}, \tag{20}$$

where

$$V(\mathbf{1}, \tilde{\boldsymbol{\nu}}_1, \mathbf{w}) = \|\mathbf{1} - \mathbf{p}_{\mathbf{w}}\|\sqrt{\|\tilde{\boldsymbol{\nu}}_1\|^2\|\mathbf{w}\|^2 - (\tilde{\boldsymbol{\nu}}_1 \cdot \mathbf{w})^2}, \tag{21}$$

is the volume of the parallelepiped spanned by the vectors $\mathbf{1}$, $\tilde{\boldsymbol{\nu}}_1$, and $\mathbf{w}$. Notice that Eq. (20) reduces to an equation similar to the minimal King plot formula [Eq. (10)] for $n = 3$ isotope pairs; however, it is insensitive to the sign of $\alpha_{NP}$. When sampling $\alpha_{NP}$ [see discussion around Eq. (13)], this insensitivity to the sign can lead to a distortion of the distribution.

### B. Algebraic methods for nonlinear King plots

In the previous section, we discussed how isotope shifts that produce linear King plots can be used to set bounds on the new physics coupling. However, the increasing sensitivity of isotope shift and nuclear mass measurements has resolved deviations from Eq. (1) [see, e.g., samarium (Sm) [23,69,70] and ytterbium (Yb) [47–50,71,72] King plots, and the combination of singly and highly charged calcium (Ca) [43][8]], calling for a more detailed analysis of the SM background. Assuming factorizability[9] of the electronic and nuclear contributions, we denote the next-to-leading SM contribution by $H_i\eta^a$, such that

$$\nu_i^a = K_i\mu^a + F_i\delta\langle r^2\rangle^a + H_i\eta^a + \cdots + \frac{\alpha_{NP}}{\alpha_{EM}}X_i\gamma^a, \tag{22}$$

where the ellipsis is a placeholder for unresolved higher-order SM contributions. In the presence of King plot nonlinearities, methods beyond the ones discussed in the previous section are needed. In the following section, we discuss how the main sources of nonlinearity can be identified and eliminated, either in a data-driven way or using additional theoretical input, and why King plots remain a useful tool to search for new physics.

#### *1. The nonlinearity decomposition*

If at least four isotope pairs are probed, there is a clear hierarchy between the King nonlinearities and predictions for their nuclear structure are available. The *nonlinearity decomposition plot* [48,49] can provide useful insights into the origin of the dominant King nonlinearity. The main idea is to project the isotope shift data onto the $n$ basis vectors $(\mathbf{1}, \tilde{\boldsymbol{\nu}}_1, \boldsymbol{\Lambda}^1, \ldots, \boldsymbol{\Lambda}^{n-2})$, where $\mathbf{1}$ and $\tilde{\boldsymbol{\nu}}_1$ define the plane of "King linearity", and the linearly independent vectors $\{\boldsymbol{\Lambda}^\ell\}_{\ell=1}^{(n-2)}$, which can be chosen to be orthogonal[10] to $\mathbf{1}$ and

[7] In the KIFIT code, this formula is referred to as the "dimension 3 no-Mass generalized King plot."

[8] After a nonlinearity had been measured recently in cadmium (Cd) [73], linearity was restored in Ref. [57].

[9] In simple systems, the application of perturbation theory leads to the separation of the nuclear and electronic scales, and consequently to the factorisation of higher-order mass- and field shifts into nuclear parameters and electronic coefficients. While this is generally a good approximation, the separation of scales tends to be more subtle for heavier atoms. For example, it has been shown in the case of $Ca^+$ that non-factorisable corrections to the quadratic field shift ($\propto \delta\langle r^2\rangle^2$) and the term $\propto \delta\langle r^4\rangle$ are negligible, while nuclear polarisability is not factorisable [52,74,75].
Here we follow the pragmatic approach of assuming factorizability, but admitting that there may be nonfactorizable terms, which, however, can be described by a sum of factorized terms, in the worst case, as many as there are isotope pairs.

[10] The results in this section can, of course, be generalized to the case where the vectors $\boldsymbol{\Lambda}^\ell$ are not orthogonal to the basis vectors $\mathbf{1}$ and $\tilde{\boldsymbol{\nu}}_1$. In this case, the projections of the higher-order terms, such as $H_i\eta^a$ onto $\mathbf{1}$ and $\tilde{\boldsymbol{\nu}}_1$ need to be taken into account.

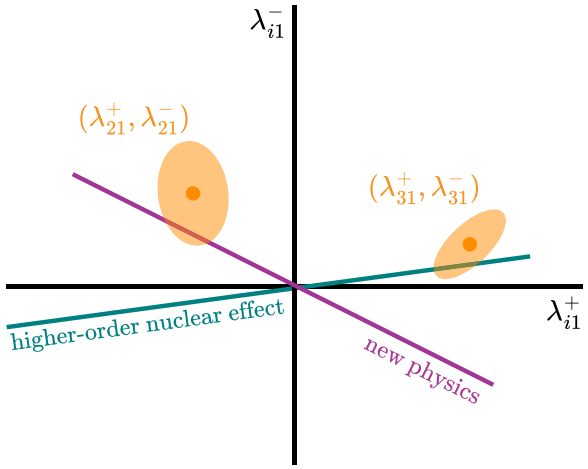


FIG. 3. Schematic illustration of the nonlinearity decomposition plot in the minimal case of four isotope pairs. The two orange points with uncertainty ellipses represent the nonlinearities observed in the King plots constructed from the isotope shift data for the transition pairs (1, 2) and (1, 3). The purple and teal lines show the predicted slopes of the new physics term and a higher-order SM contribution to the isotope shift, respectively.

$\tilde{\boldsymbol{\nu}}_1$, define a basis for the "King nonlinearity space":

$$\tilde{\boldsymbol{\nu}}_i = K_{i1}\mathbf{1} + F_{i1}\tilde{\boldsymbol{\nu}}_1 + \sum_{\ell=1}^{n-2} \lambda_{i1}^{\ell} \boldsymbol{\Lambda}^{\ell}. \tag{23}$$

In the minimal case of 4 isotope pairs, as in Refs. [48–50] and Ref. [43], which considered the five even stable isotopes of Yb and Ca, respectively, the basis vectors of the King nonlinearity space can be expressed as [49]

$$\begin{aligned} \boldsymbol{\Lambda}^+ &\sim \left(\tilde{\nu}_1^3 - \tilde{\nu}_1^2, \tilde{\nu}_1^1 - \tilde{\nu}_1^4, \tilde{\nu}_1^4 - \tilde{\nu}_1^1, \tilde{\nu}_1^2 - \tilde{\nu}_1^3\right), \\ \boldsymbol{\Lambda}^- &\sim \left(\tilde{\nu}_1^4 - \tilde{\nu}_1^2, \tilde{\nu}_1^1 - \tilde{\nu}_1^3, \tilde{\nu}_1^2 - \tilde{\nu}_1^4, \tilde{\nu}_1^3 - \tilde{\nu}_1^1\right), \end{aligned} \tag{24}$$

and Eq. (23) reads

$$\tilde{\boldsymbol{\nu}}_i = K_{i1}\mathbf{1} + F_{i1}\tilde{\boldsymbol{\nu}}_1 + \lambda_{i1}^+ \boldsymbol{\Lambda}^+ + \lambda_{i1}^- \boldsymbol{\Lambda}^-. \tag{25}$$

The projections $\lambda_{i1}^+$ and $\lambda_{i1}^-$ are used as coordinates in the nonlinearity decomposition plot, which in the case of four isotope pairs is two-dimensional, as illustrated in Fig. 3: Each point $(\lambda_{i1}^+, \lambda_{i1}^-)$, $i = 2, 3$ in the nonlinearity decomposition plot represents the nonlinearities in the two-dimensional King plot constructed from the transitions $i$ and 1. If its uncertainty ellipse contains the origin of the $(\lambda_{i1}^+, \lambda_{i1}^-)$ plane, the associated King plot can be considered to be linear; else additional terms need to be added to the isotope shift equations to describe the data.

The nonlinearity decomposition plot is particularly useful when there is a strong hierarchy between the nonlinearities. In the case of one dominant King nonlinearity that can be factorized into electronic and nuclear contributions [such as, e.g., $H_i$ and $\eta^a$ in Eq. (22)], the data points approximately lie on one line in the nonlinearity decomposition plot. Indeed, in this case the slope $\lambda_{i1}^-/\lambda_{i1}^+$ defined by the projections onto the space of King nonlinearity is transition independent:

$$\frac{\lambda^-}{\lambda^+} \equiv \frac{\lambda_{i1}^-}{\lambda_{i1}^+} = \frac{(\tilde{\boldsymbol{\eta}} \cdot \boldsymbol{\Lambda}^-)(\boldsymbol{\Lambda}^+ \cdot \boldsymbol{\Lambda}^+) - (\tilde{\boldsymbol{\eta}} \cdot \boldsymbol{\Lambda}^+)(\boldsymbol{\Lambda}^- \cdot \boldsymbol{\Lambda}^+)}{(\tilde{\boldsymbol{\eta}} \cdot \boldsymbol{\Lambda}^+)(\boldsymbol{\Lambda}^- \cdot \boldsymbol{\Lambda}^-) - (\tilde{\boldsymbol{\eta}} \cdot \boldsymbol{\Lambda}^-)(\boldsymbol{\Lambda}^- \cdot \boldsymbol{\Lambda}^+)}, \tag{26}$$

and a comparison with predictions for different nuclear parameters $\tilde{\boldsymbol{\eta}}$ can be used to identify the origin of the dominant nonlinearity in the data.

The purple line through the origin in Fig. 3 illustrates how the new physics hypothesis introduced in Eq. (7) can be tested with the help of the nonlinearity decomposition plot: If all uncertainty ellipses overlap with this purple line, the observed nonlinearities are compatible with the new physics hypothesis (or any other effect that is proportional to the neutron number). A similar statement can be made for higher-order nuclear contributions. The slopes of the corresponding lines can either be determined via nuclear structure calculations or using complementary experimental input.

Note that more than one source of nonlinearity, as well as input for their electronic structure, is needed to describe the data that does not lie on a line through the origin of the $(\lambda_{i1}^+, \lambda_{i1}^-)$ plane.

*Generalization to n isotope pairs.* If isotope shift data for $n$ isotope pairs is available, more than one nonlinearity can be identified in this data-driven way. We define the vector of coordinates associated with the King plot for the transitions $i$ and 1 as $\boldsymbol{\lambda}_{i1} = (\lambda_{i1}^1, \ldots, \lambda_{i1}^{n-2})^\top$ and introduce the $[n \times (n-2)]$-matrix $\boldsymbol{\Omega} = (\boldsymbol{\Lambda}^1, \ldots, \boldsymbol{\Lambda}^{n-2})$ of vectors that span the nonlinearity space. Equation (23) can then be generalized using $\sum_{\ell=1}^{n-2} \lambda_{i1}^{\ell} \boldsymbol{\Lambda}^{\ell} = \boldsymbol{\Omega}\boldsymbol{\lambda}_{i1}$.

Using the Moore-Penrose pseudoinverse of $\boldsymbol{\Omega}$ to solve for the coordinates $\lambda_{i1}^{\ell}$, one obtains the generalization of Eq. (27)

$$\frac{\lambda_{i1}^{\ell'}}{\lambda_{i1}^{\ell}} = \frac{[(\boldsymbol{\Omega}^\top\boldsymbol{\Omega})^{-1}\boldsymbol{\Omega}^\top\tilde{\boldsymbol{\eta}}]^{(\ell')}}{[(\boldsymbol{\Omega}^\top\boldsymbol{\Omega})^{-1}\boldsymbol{\Omega}^\top\tilde{\boldsymbol{\eta}}]^{(\ell)}}, \quad \ell' \neq \ell, \tag{27}$$

where $[\cdot]^{(\ell)}$ is to be understood as the $\ell^{\text{th}}$ entry of $[\cdot]$. Since $\ell, \ell'$ run from 1 to $n-2$, and $\ell' \neq \ell$, this method can resolve $n-3$ sources of King plot nonlinearity, i.e., one in the case of four isotope pairs.

Note that while the slope of the predicted nonlinearity in the King plane is transition-independent, the coordinates $\lambda_{i1}^{\ell}$ are not and their magnitude

$$\|\boldsymbol{\lambda}_{i1}\| = \sqrt{\sum_{\ell} \left(\lambda_{i1}^{\ell}\right)^2} = |H_{i1}|\sqrt{\tilde{\boldsymbol{\eta}}^\top\boldsymbol{\Omega}(\boldsymbol{\Omega}^\top\boldsymbol{\Omega})^{-2}\boldsymbol{\Omega}^\top\tilde{\boldsymbol{\eta}}}, \tag{28}$$

or

$$\begin{aligned} \lambda_{i1}^+ &= H_i\tilde{\boldsymbol{\eta}} \cdot \frac{\boldsymbol{\Lambda}^+(\boldsymbol{\Lambda}^- \cdot \boldsymbol{\Lambda}^-) - \boldsymbol{\Lambda}^-(\boldsymbol{\Lambda}^- \cdot \boldsymbol{\Lambda}^+)}{(\boldsymbol{\Lambda}^+ \cdot \boldsymbol{\Lambda}^+)(\boldsymbol{\Lambda}^- \cdot \boldsymbol{\Lambda}^-) - (\boldsymbol{\Lambda}^- \cdot \boldsymbol{\Lambda}^+)^2}, \\ \lambda_{i1}^- &= H_i\tilde{\boldsymbol{\eta}} \cdot \frac{\boldsymbol{\Lambda}^-(\boldsymbol{\Lambda}^+ \cdot \boldsymbol{\Lambda}^+) - \boldsymbol{\Lambda}^+(\boldsymbol{\Lambda}^- \cdot \boldsymbol{\Lambda}^+)}{(\boldsymbol{\Lambda}^+ \cdot \boldsymbol{\Lambda}^+)(\boldsymbol{\Lambda}^- \cdot \boldsymbol{\Lambda}^-) - (\boldsymbol{\Lambda}^- \cdot \boldsymbol{\Lambda}^+)^2} \end{aligned} \tag{29}$$

in the case of four isotope pairs, can be used to extract the electronic coefficients $H_{i1}$ from data.

### 2. *Generalized King plots*

In the recent Yb [47–50,71,72] and Ca [43] King plots, the leading nonlinearity is not compatible with the new physics

term and so-called *generalized King plots* [53] were employed to set bounds on $\alpha_{\rm NP}$. These generalize Eqs. (10) and (15) to higher dimensions, i.e., they use additional measurements to eliminate higher-order nuclear contributions to the isotope shift equations.

For concreteness, let us assume the isotope shift equations take the form of Eq. (22): As discussed in the case of the *minimal King plot*, isotope shift data for two transitions, $i = 1, 2$, allow us to eliminate the charge radius variance, $\delta\langle r^2\rangle$, resulting in

$$\tilde{\nu}_2^a = K_{21} + F_{21}\tilde{\nu}_1^a + H_{21}\tilde{\eta}^a + \cdots + \frac{\alpha_{\rm NP}}{\alpha_{\rm EM}} X_{21}\tilde{\gamma}^a, \tag{30}$$

where $H_{21} \equiv H_2 - F_{21}H_1$.

If isotope shifts are measured in a third transition $i = 3$, they can be used to eliminate the higher-order SM term $\tilde{\eta}^a$, leading to

$$\tilde{\nu}_3^a = K_{321} + F_{321}\tilde{\nu}_1^a + H_{321}\tilde{\nu}_2^a + \cdots + \frac{\alpha_{\rm NP}}{\alpha_{\rm EM}} X_{321}\tilde{\gamma}^a, \tag{31}$$

with $H_{321} \equiv H_{31}/H_{21}$ and $P_{321} = P_{31} - H_{321}P_{21}$, with $P \in \{K, F, X\}$. Assuming the higher-order SM terms represented by the ellipsis are negligible, the isotope shift data can be used to set bounds on the new physics term (see fit in Ref. [49]). Note, however, that any direct extraction of $\alpha_{\rm NP}$ from Eq. (31) will be affected by the large theoretical uncertainties associated with the prediction for the electronic coefficient $X_{321}$, corresponding to a difference of the $X$ coefficients introduced in Eq. (7).

One of the main strengths of the generalized King plot formulas is that they directly use the $X$ coefficients introduced in Eq. (7) rather than relying on differences thereof. Assuming isotope shifts for $m$ transitions are measured in $n = m + 1$ isotope pairs, solving the system of $m \times n$ isotope shift equations for $\alpha_{\rm NP}$ leads to the generalized King plot (GKP) formula [53][11]

$$\frac{\alpha_{\rm NP}}{\alpha_{\rm EM}} = \frac{(n-2)!\,\det(\tilde{\mathbf{v}}_1, \ldots, \tilde{\mathbf{v}}_{n-1}, \mathbf{1})}{\varepsilon_{i_1,\ldots,i_{n-1}} \det\left(X_{i_1}\tilde{\boldsymbol{\gamma}}, \tilde{\mathbf{v}}_{i_2}, \ldots, \tilde{\mathbf{v}}_{i_{n-1}}, \mathbf{1}\right)}, \tag{32}$$

As briefly suggested in Ref. [53], if higher-order SM contributions are present and the uncertainties on the nuclear masses are a limiting factor, it can be advantageous to combine the benefits of the GKP and NMKP [Eq. (15)] formulas, obtaining a *no-mass generalized King plot (NMGKP)* formula:

$$\frac{\alpha_{\rm NP}}{\alpha_{\rm EM}} = \frac{(n-1)!\,\det(\boldsymbol{\nu}_1, \boldsymbol{\nu}_2, \ldots, \boldsymbol{\nu}_n)}{\varepsilon_{i_1,i_2,\ldots,i_n} \det\left(X_{i_1}\boldsymbol{\gamma}, \boldsymbol{\nu}_{i_2}, \ldots, \boldsymbol{\nu}_{i_n}\right)}. \tag{33}$$

#### 3. Subtracting SM nonlinearities

For lighter systems such as Ca, where the mass shift dominates over the field shift, the next-to-leading order SM contribution to Eq. (3) might be the second-order mass shift [52], $\nu_i^a|_{\rm MS(2)} = K_i^{(2)}\mu^{a(2)}$, where $\mu^{a(2)} \equiv 1/(m^A)^2 - 1/(m^{A'})^2$ is the difference of the squared inverse nuclear masses and $K_i^{(2)}$ is an electronic coefficient. Since in this case the nuclear parameters (namely, the isotope masses) can be determined experimentally at high precision, the second-order mass shift can be kept explicit in the isotope shift equations, such that

$$\tilde{\nu}_2^a = K_{21} + F_{21}\tilde{\nu}_1^a + \frac{\alpha_{\rm NP}}{\alpha_{\rm EM}} X_{21}\tilde{\gamma}^a + K_{21}^{(2)}\tilde{\mu}^{a(2)}. \tag{34}$$

If the frequency shifts $\nu_i^a$, $i = 1, 2$, are measured in four isotope pairs, Eq. (34) can then be solved for $\alpha_{\rm NP}$, yielding

$$\frac{\alpha_{\rm NP}}{\alpha_{\rm EM}} = \frac{\det(\tilde{\mathbf{v}}_1, \tilde{\mathbf{v}}_2, \mathbf{1}, \tilde{\boldsymbol{\mu}}^{(2)})}{\varepsilon_{ij}\det(X_i\tilde{\boldsymbol{\gamma}}, \tilde{\mathbf{v}}_j, \mathbf{1}, \tilde{\boldsymbol{\mu}}^{(2)})}, \tag{35}$$

where all bold symbols are 4-vectors in isotope-pair space. In this case, one higher-order effect can be taken into account without adding an additional transition. We refer to this equation as the *nuclear input King plot (NIKP)* formula.

Alternatively, if the electronic coefficients $K_i^{(2)}$ can be predicted with sufficient accuracy (see, e.g., Refs. [43,52], where a 10% uncertainty is assigned to the prediction of $K_i^{(2)}$), the second-order mass shift can be subtracted from the measured isotope shift [43], yielding an isotope shift equation which resembles Eq. (3):

$$\left(\tilde{\nu}_2^a - K_{21}^{(2)}\tilde{\mu}^{a(2)}\right) = K_{21} + F_{21}\tilde{\nu}_1^a + \alpha_{\rm NP}X_{21}\tilde{\gamma}^a. \tag{36}$$

Now $\alpha_{\rm NP}$ can be obtained using Eq. (10) with the modification $\tilde{\nu}_2^a \to (\tilde{\nu}_2^a)' = \tilde{\nu}_2^a - K_{21}^{(2)}\tilde{\mu}^{a(2)}$. Since $K_i^{(2)}$ depends only on the electronic structure, it induces correlations between the objects $\{(\tilde{\nu}_2^a)'\}_{a=1}^n$, which in turn reduce the impact of the uncertainty on the coefficients $K_i^{(2)}$ on $\sigma[\alpha_{\rm NP}]$ [43].

The strategy of subtracting higher-order SM contributions until relations such as Eq. (36) arise, could be promising to bridge the gap between light elements such as hydrogen, deuterium, or helium [76–79], where spectroscopic bounds can be derived from a direct comparison of predictions and measurements, and heavy elements such as Yb, where corrections to the charge distribution, such as nuclear deformation, are sizable but hard to predict from first principles [50].

#### 4. Combining datasets

In Sec. II, we discussed the algebraic methods summarized in Table I. The advantage of these methods is their simplicity. However, they can only be applied to datasets of the specific dimensions given in Table I. If the available datasets come in different shapes, we are forced to derive bounds using subsets of the data, and how these resulting bounds are best combined is unclear.

In the following section, we follow an alternative approach consisting of a fit to isotope shift data. This strategy is more flexible regarding the dimensions of the input data and, in particular, enables a fit to isotope shift data from different elements.

## III. THE KING PLOT FIT

The King plot fit presented in this section is inspired by Ref. [36] but significantly extended such that it can handle the

[11] In the KIFIT code this formula is referred to as the "dimension-$n$ generalized King plot," where $n$ is the number of isotope pairs. Using frequency-normalized quantities, i.e., $\bar{\tau}^a \equiv \tau^a/\nu_1^a$, $\tau \in \{\nu_i, \mu, \gamma\}$, $i = 1, \ldots, m$, Eq. (32) takes the form:

$$\frac{\alpha_{\rm NP}}{\alpha_{\rm EM}} = \frac{(n-2)!\,\det(\bar{\mathbf{v}}_1, \ldots, \bar{\mathbf{v}}_{n-1}, \bar{\boldsymbol{\mu}})}{\varepsilon_{i_1,\ldots,i_{n-1}}\det(X_{i_1}\bar{\boldsymbol{\gamma}}, \bar{\mathbf{v}}_{i_2}, \ldots, \bar{\mathbf{v}}_{i_{n-1}}, \bar{\boldsymbol{\mu}})}.$$

TABLE I. Summary of the number of transitions and isotope pairs that are required by the different algebraic methods presented in Sec. II and by the King plot fit KIFIT introduced in Sec. III. (Note that $m$ and $n$ are independent integers.) For the GKP and the NMGKP we also give the number of higher-order nuclear parameters (spurions) that are eliminated while setting a bound on the coupling $\alpha_{\mathrm{NP}}$. KP and NMKP are the minimal cases of GKP and NMGKP, respectively.

| | KP Eq. (10) | NMKP Eq. (15) | GKP Eq. (32) | NMGKP Eq. (33) | KIFIT Sec. III |
|---|---|---|---|---|---|
| Isotope pairs | 3 | 3 | $3 \leqslant n$ | $3 \leqslant n$ | $3 \leqslant n$ |
| Transitions | 2 | 3 | $n-1$ | $n$ | $2 \leqslant m$ |
| Spurions | | | $n-3$ | $n-3$ | |

contemporary precision of isotope shift data and potentially large hierarchies between the levels of uncertainty of different subsets of the data. In the following, we describe the theoretical framework and the main steps of the algorithm, which is structured into a *build phase*, a *search phase*, an *experiment phase,* and a *consolidation phase*, as illustrated in Fig. 6. An implementation of this procedure is provided in the form of the PYTHON package KIFIT, which is publicly available [80]. More instructions on how to use the package can be found in Appendix III. The data provided by the current version of KIFIT is summarized in Appendix F.

### A. Geometric construction (build phase)

One of the advantages of the King plot fit is that it is more flexible than the algebraic methods described in Sec. II A (see Table I for an overview) in regard to the number of transitions and isotope pairs that it can combine. As in Sec. II B, $m$ denotes the number of transitions and $n$ the number of isotope pairs considered for a given element.

Depending on the application, it can be advantageous to arrange the same isotope shift data in terms of isotope pairs or transitions: For the construction of the determinants discussed in Sec. II A, it is beneficial to describe the data in terms of the vectors $\mathbf{1}$, $\tilde{\boldsymbol{\nu}}_i$, and $\tilde{\boldsymbol{\gamma}}$, which are fixed by the transition frequency and mass measurements, as well as the neutron number difference. For the fit, which is performed directly on the level of the King plot and constrains deviations from the King line defined by the electronic coefficients $F_{i1}$, $K_{i1}$, $i = 2, \ldots, m$, it is more natural to work in transition space.

Fixing $i = 1$ as the reference transition and assuming the isotope shift data to be linear, we can construct $(m-1)$ relations of the form of Eq. (3), and arrange them into $n$ linear $m$-vector equations, one for every isotope pair $a$ [36]:

$$\tilde{\boldsymbol{\nu}}^a|_{\mathrm{lin.}} \equiv \begin{pmatrix} \tilde{\nu}_1^a \\ \tilde{\nu}_2^a|_{\mathrm{lin.}} \\ \vdots \\ \tilde{\nu}_m^a|_{\mathrm{lin.}} \end{pmatrix} = \begin{pmatrix} 0 \\ K_{21} \\ \vdots \\ K_{m1} \end{pmatrix} + \tilde{\nu}_1^a \begin{pmatrix} 1 \\ F_{21} \\ \vdots \\ F_{m1} \end{pmatrix} \equiv \boldsymbol{\mathcal{K}} + \tilde{\nu}_1^a \boldsymbol{\mathcal{F}}. \tag{37}$$

Here we introduced the $m$-dimensional electronic coefficient vectors $\boldsymbol{\mathcal{K}}$ and $\boldsymbol{\mathcal{F}}$. Note that the isotope shift vectors introduced in Eq. (5) and used in Secs. II A and II B were vectors in isotope pair space, meaning that we had one for each transition, whereas the vectors that appear in Eq. (37) are vectors in transition space, meaning that we have one for each isotope pair.

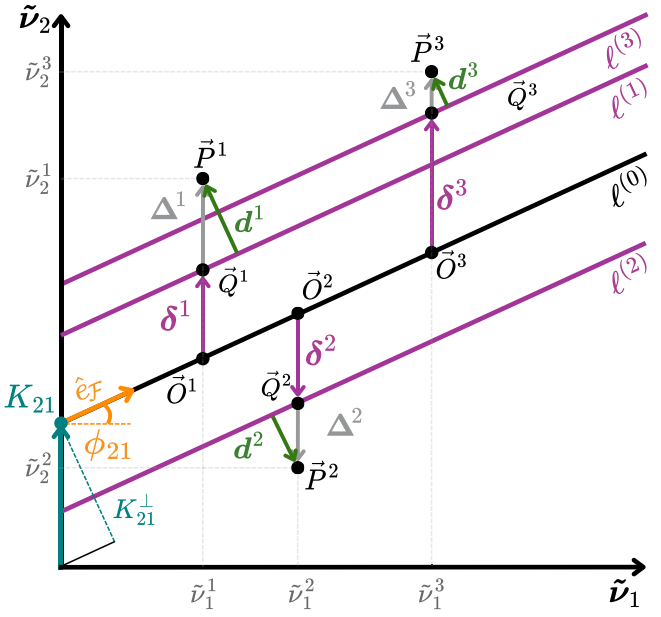


FIG. 4. Illustration of the KIFIT construction in the simplest case of $m = 2$ transitions and $n = 3$ isotope pairs. We use the notation $\vec{O}^a = (\tilde{\nu}_1^a, \tilde{\nu}_2^a|_{\mathrm{lin.}})$, $a = 1, 2, \ldots, n$ for the linear prediction [Eq. (37)], $\vec{Q}^a = (\tilde{\nu}_1^a, \tilde{\nu}_2^a|_{\mathrm{pred.}})$ for the nonlinear prediction including new physics [Eq. (42)] and $\vec{P}^a = (\tilde{\nu}_1^a, \tilde{\nu}_2^a)$ for the data points, and indicate the endpoints of the respective vectors with black dots. The King line obtained from the initial fit to the isotope shift data is denoted $\ell^{(0)}$ and described by the fit parameters $K_{21}^{\perp}$ and $\phi_{21}$, whereas the parallel line associated with the isotope pair $a$ is denoted $\ell^{(a)}$.

Figure 4 is a two-dimensional illustration of Eq. (37) for the case of $m = 2$ transitions and $n = 3$ isotope pairs: By construction, the points $\vec{O}^a = (\tilde{\nu}_1^a, \tilde{\nu}_2^a|_{\mathrm{lin.}})$, $a = 1, 2, 3$ lie on a *King line* $\ell^{(0)}$ with intercept $K_{21}$ and slope $F_{21}$. In the KIFIT code, the vector $\boldsymbol{\mathcal{F}}$ of electronic field shift coefficients is expressed in terms of the inclination angles $\phi_{j1}$ of the King lines in the $(\tilde{\boldsymbol{\nu}}_1, \tilde{\boldsymbol{\nu}}_j)$ plane. This is reasonable, since only its orientation matters. The unit vector $\hat{\boldsymbol{e}}_{\boldsymbol{\mathcal{F}}}$, directed along the King line $\ell^{(0)}$ (orange vector in Figs. 4 and 5) takes the form

$$\hat{\boldsymbol{e}}_{\boldsymbol{\mathcal{F}}} \equiv \frac{\boldsymbol{\mathcal{F}}}{\|\boldsymbol{\mathcal{F}}\|} = \frac{1}{\sqrt{1 + \sum_{j=2}^{m} \tan^2 \phi_{j1}}} \begin{pmatrix} 1 \\ \tan\phi_{21} \\ \vdots \\ \tan\phi_{m1} \end{pmatrix}. \tag{38}$$

We can define an angle $\phi$ that satisfies

$$\cos\phi = \frac{1}{\sqrt{1 + \sum_{j=2}^{m} \tan^2 \phi_{j1}}}, \tag{39}$$

and corresponds to the angle between the direction $\hat{\boldsymbol{e}}_{\mathbf{1}} = (1, 0, \ldots, 0)$ fixed by the reference transition 1 and the King line. In the case of two transitions, $\phi = \phi_{21}$ (see also Fig. 4).

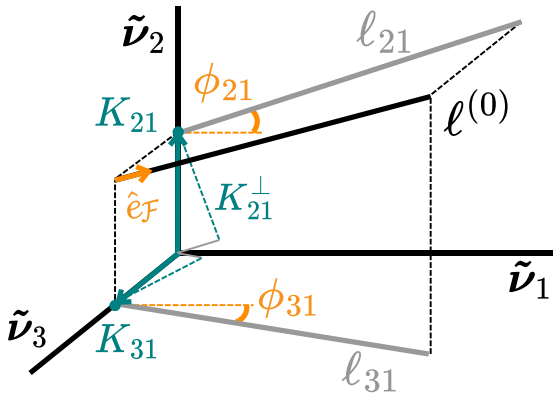


FIG. 5. Illustration of a three-dimensional King plot with a King line $\ell^{(0)}$ (black), fixed by the fit parameters $\phi_{j1}$ [see Eq. (38)] and $K_{j1}^{\perp}$, $j = 2, 3$ [see Eq. (40)] and oriented in the direction of the unit vector $\hat{\boldsymbol{e}}_{\boldsymbol{\mathcal{F}}}$. The lines $\ell_{j1}$, $j = 2, 3$, represent the King lines of the two-dimensional King plots constructed for the transition pairs (1, 2) and (1, 3), respectively.

Instead of taking the $m-1$ intercepts $\{K_{j1}\}_{j=2}^{m}$ to be fit parameters, we introduce

$$\mathcal{K}^{\perp} \equiv \begin{pmatrix} K_{11}^{\perp} \\ K_{21}^{\perp} \\ \vdots \\ K_{m1}^{\perp} \end{pmatrix} = \begin{pmatrix} -\sum_{j=2}^{m} \sin\phi_{j1} K_{j1} \\ \cos\phi_{21} K_{21} \\ \vdots \\ \cos\phi_{m1} K_{m1} \end{pmatrix}, \tag{40}$$

which is orthogonal to $\hat{\boldsymbol{e}}_{\boldsymbol{\mathcal{F}}}$, and fit to the $m-1$ projected intercepts $\{K_{j1}^{\perp}\}_{j=2}^{m}$. This parametrization is crucial for the numerical stability of the fit in the limit where $\hat{\boldsymbol{e}}_{\boldsymbol{\mathcal{F}}}$ and $\mathcal{K}$ approach collinearity and $K_{j1}^{\perp} \ll K_{j1}$.

The initial guesses $\{\langle K_{j1}^{\perp}\rangle, \langle\phi_{j1}\rangle\}_{j=2}^{m}$ for the $2(m-1)$ fit parameters and their covariance matrix $\boldsymbol{\Sigma}_{K\phi}^{(j1)}$ are determined by a set of $(m-1)$ linear fits. Since King plots are constructed from pairs of isotope shifts, all of which have uncertainties, we perform orthogonal distance regression (ODR) [81] that is implemented in the `scipy.odr` method of the Scipy package [82].

Once the background (i.e., the linear King plot) is fixed, we can proceed with the parametrization of the signal: the new physics term introduced in Eq. (9) leads to isotope-pair dependent shifts of the data points in transition space (i.e., in the King plot):

$$\boldsymbol{\delta}^{a} = \frac{\alpha_{\mathrm{NP}}}{\alpha_{\mathrm{EM}}} \tilde{\gamma}^{a} \boldsymbol{\mathcal{X}}, \quad \boldsymbol{\mathcal{X}} = (0, X_{21}, \ldots, X_{m1})^{\top}. \tag{41}$$

Here, $X_{j1} \equiv X_j - F_{j1} X_1 = X_j - \tan\phi_{j1} X_1$, $j = 2, \ldots, m$, are the electronic coefficients that are constructed from the fit parameter $\phi_{j1}$ and the coefficients $X_i$, $i = 1, \ldots, m$ determined by means of atomic structure calculations (see Sec. II A and Appendix A). The predictions $\tilde{\boldsymbol{\nu}}^{a}|_{\mathrm{pred.}}$ incorporating the linear isotope shift behavior plus the shifts predicted by the new physics term are simply given by

$$\tilde{\boldsymbol{\nu}}^{a}|_{\mathrm{pred.}} = \tilde{\boldsymbol{\nu}}^{a}|_{\mathrm{lin.}} + \boldsymbol{\delta}^{a}, \quad a = 1, \ldots, n. \tag{42}$$

For each isotope pair $a$, Eq. (42) defines a parallel line $\ell^{(a)}$ to the King line $\ell^{(0)}$. In Fig. 4, $\vec{Q}^{a} = (\tilde{\nu}_1^{a}, \tilde{\nu}_2^{a}|_{\mathrm{pred.}})$, $a = 1, 2, 3$, and the vectors $\boldsymbol{\delta}^{a}$ with their associated lines $\ell^{(a)}$ are depicted in purple.

Since it is impossible to distinguish a constant shift of all points $\tilde{\nu}_i^{a}$, $1 < i \leqslant m$, from a variation of the mass shift coefficients $K_{i1}$, we only include the variations $\boldsymbol{\sigma}[\boldsymbol{\delta}^{a}]$ with respect to the mean new physics-induced shift in our new physics predictions. The elements of $\boldsymbol{\sigma}[\boldsymbol{\delta}^{a}]$ can be estimated as

$$\sigma\left[\delta_j^{a}\right] = \frac{\alpha_{\mathrm{NP}}}{\alpha_{\mathrm{EM}}} (\tilde{\gamma}^{a} - \langle\tilde{\gamma}\rangle^{j}) X_{j1}, \tag{43}$$

where

$$\langle\tilde{\gamma}\rangle^{j} = \frac{\sum_{a=1}^{n} \tilde{\gamma}^{a} \sigma\left[\tilde{\nu}_j^{a}\right]}{\sum_{b=1}^{n} \sigma\left[\tilde{\nu}_j^{b}\right]}, \quad j = 2, \ldots, m \tag{44}$$

is the average value of the new physics nuclear parameter $\tilde{\gamma}^{a}$, weighted by the uncertainties on the mass-normalized isotope shifts. [Note that, by construction, $\sigma[\delta_1^{a}] = 0\ \forall\ a$, since $X_{11} = 0$, see Eq. (41)]. In this way, the constant shift induced by the quantities $\langle\tilde{\gamma}\rangle^{i}$ is effectively absorbed in the fit parameters $\{K_{j1}^{\perp}\}_{j=2}^{m}$, leading to a corrected mass shift vector

$$\mathcal{K}' = \mathcal{K} + \langle\tilde{\boldsymbol{\gamma}}\rangle, \tag{45}$$

with $\langle\tilde{\boldsymbol{\gamma}}\rangle = (\langle\tilde{\gamma}\rangle^{1}, \ldots, \langle\tilde{\gamma}\rangle^{n})^{\top}$. Using these definitions, we obtain for the isotope shift

$$\tilde{\boldsymbol{\nu}}^{a}|_{\mathrm{pred.}} = \mathcal{K}' + \tilde{\nu}_1^{a} \boldsymbol{\mathcal{F}} + \boldsymbol{\sigma}[\boldsymbol{\delta}^{a}], \quad a = 1, \ldots, n. \tag{46}$$

For simplicity, we will omit the prime in $\mathcal{K}'$ in the following.

Note that in general Eq. (44) induces a slight asymmetry under exchange of transitions. To cross-check the parametrization, we implement in the `KIFIT` code a transition-independent version of $\boldsymbol{\sigma}[\boldsymbol{\delta}^{a}]$, with

$$\langle\tilde{\gamma}\rangle \equiv \frac{1}{n} \sum_{a=1}^{n} \tilde{\gamma}^{a} = \langle\tilde{\gamma}\rangle^{i} \quad \forall\ i. \tag{47}$$

The invariance of the `KIFIT` construction under exchange of transitions is discussed in more detail in Appendix D 3.

#### 1. Construction of the log-likelihood

The aim of the King plot fit is to minimize the distances of the experimental data points $\tilde{\boldsymbol{\nu}}^{a}$ (denoted $\vec{P}^{a}$ in Fig. 4) from the parallel lines $\ell^{(a)}$. These distances are given by

$$\boldsymbol{d}^{a} = \boldsymbol{\Delta}^{a} - (\boldsymbol{\Delta}^{a} \cdot \hat{\boldsymbol{e}}_{\boldsymbol{\mathcal{F}}}) \hat{\boldsymbol{e}}_{\boldsymbol{\mathcal{F}}}, \quad a = 1, \ldots, n, \tag{48}$$

with $\hat{\boldsymbol{e}}_{\boldsymbol{\mathcal{F}}}$ as defined in Eq. (38) and the vectors $\boldsymbol{\Delta}^{a}$ that connect the predictions $\tilde{\boldsymbol{\nu}}^{a}|_{\mathrm{pred.}}$ with the data points $\tilde{\boldsymbol{\nu}}^{a}$:[12]

$$\boldsymbol{\Delta}^{a} \equiv \tilde{\boldsymbol{\nu}}^{a} - \tilde{\boldsymbol{\nu}}^{a}|_{\mathrm{pred.}} = \tilde{\boldsymbol{\nu}}^{a} - \left(\mathcal{K} + \tilde{\nu}_1^{a} \boldsymbol{\mathcal{F}} + \boldsymbol{\sigma}[\boldsymbol{\delta}^{a}]\right). \tag{49}$$

[12]Here we are assuming that we only ever compare one data point $\tilde{\boldsymbol{\nu}}^{a}$ with a given prediction $\tilde{\boldsymbol{\nu}}^{a}|_{\mathrm{pred.}}$. In presence of $s$ measurements of the same isotope shift $\nu_i^{a}$, $s$ different copies of the element $\Delta_i^{a}$ would need to be taken into account. In the current version of the `KIFIT` code, we assume these complementary measurements to be independent, such that they can be combined in a similar way to separate elements [see Eq. (57)].

More explicitly,

$$d_1^a = -\frac{1}{\|\boldsymbol{\mathcal{F}}\|^2}\sum_{k=2}^{m}\tan(\phi_{k1})\Delta_{k1}^a,$$
$$d_{j\neq 1}^a = \Delta_{j1}^a + \tan(\phi_{j1})d_1^a, \tag{50}$$

where $\|\boldsymbol{\mathcal{F}}\|^2 = 1+\sum_{j=2}^{m}\tan^2\phi_{j1}$ [see Eq. (38)] and

$$\Delta_{j1}^a = \tilde{\nu}_j^a - \left(K_{j1} + \frac{\tan\phi_{j1}}{\|\boldsymbol{\mathcal{F}}\|}\tilde{\nu}_1^a + \sigma\left[\delta_{j1}^a\right]\right). \tag{51}$$

Assuming that the Euclidean norms $\|\boldsymbol{d}^a\| = [\sum_{i=1}^{m}(d_i^a)^2]^{1/2}$ approximately follow a multivariate normal distribution, we define the negative log-likelihood

$$-\ln\mathcal{L} \propto \frac{1}{2}\sum_{a=1}^{n}\sum_{b=1}^{n}\left[\ln\Sigma^{ab} + \|\boldsymbol{d}^a\|\left(\Sigma_{\boldsymbol{d}}^{ab}\right)^{-1}\|\boldsymbol{d}^b\|\right], \tag{52}$$

where $\Sigma_{\boldsymbol{d}}^{ab} \equiv \mathrm{Cov}(\|\boldsymbol{d}^a\|, \|\boldsymbol{d}^b\|)$ denotes the covariance of the norms $\|\boldsymbol{d}^a\|$ and $\|\boldsymbol{d}^b\|$. In vector notation,

$$-\ln\mathcal{L} \propto \tfrac{1}{2}\left[\ln\det\boldsymbol{\Sigma}_{\boldsymbol{d}} + \mathbf{d}\boldsymbol{\Sigma}_{\boldsymbol{d}}^{-1}\mathbf{d}\right], \tag{53}$$

where $\mathbf{d} \equiv (\|\boldsymbol{d}^1\|, \ldots, \|\boldsymbol{d}^n\|)^\top$ and $\boldsymbol{\Sigma}_{\boldsymbol{d}}$ is the associated covariance matrix. The latter can be estimated in different ways. For an order-of-magnitude estimate, linear error propagation is sufficient. Assuming the frequency measurements are independent,

$$\begin{aligned}\Sigma_{\boldsymbol{d}}^{ab} = &\sum_{i=1}^{m}\sum_{c=1}^{n}\left(\frac{\partial\|\boldsymbol{d}^a\|}{\partial\nu_i^c}\sigma\left[\nu_i^c\right]\right)^2\delta^{ab}\\ &+\sum_{A}\frac{\partial\|\boldsymbol{d}^a\|}{\partial m^A}\sigma[m^A]^2\frac{\partial\|\boldsymbol{d}^b\|}{\partial m^A}\\ &+\sum_{A'}\frac{\partial\|\boldsymbol{d}^a\|}{\partial m^{A'}}\sigma[m^{A'}]^2\frac{\partial\|\boldsymbol{d}^b\|}{\partial m^{A'}}\\ &+\sum_{j=2}^{m}(\boldsymbol{\nabla}_{\boldsymbol{K\phi}}^{\boldsymbol{j1}}\|\boldsymbol{d}^a\|)^\top\boldsymbol{\Sigma}_{K\phi}^{(j1)}(\boldsymbol{\nabla}_{\boldsymbol{K\phi}}^{\boldsymbol{j1}}\|\boldsymbol{d}^b\|),\end{aligned} \tag{54}$$

where the small indices run over isotope pairs and the capital ones run over isotopes. Here we introduced the notation $\boldsymbol{\nabla}_{\boldsymbol{K\phi}}^{\boldsymbol{j1}} \equiv (\partial_{K_{j1}^\perp}, \partial_{\phi_{j1}})^\top$ and the $2\times 2$ covariance matrix $\boldsymbol{\Sigma}_{K\phi}^{(j1)}$ of the fit parameters $K_{j1}^\perp$ and $\phi_{j1}$, which is determined by performing ODR on the data points $\{(\tilde{\nu}_1^a, \tilde{\nu}_j^a)\}_{a=1}^n$, as explained in the previous paragraph.

Rather than linear error propagation, the KIFIT code estimates the covariance matrix $\boldsymbol{\Sigma}_{\boldsymbol{d}}$ by means of a simple Monte Carlo approach, in which the input parameters $m^A$, $m^{A'}$, and $\nu_i^a$, $a = 1, \ldots, n$ are sampled from Gaussian distributions fixed by the experimental central values and uncertainties [see Eq. (14)], whereas the fit parameters $\{K_{j1}^\perp, \phi_{j1}\}_{j=2}^m$ are sampled from the Gaussian distribution fixed by the best-fit results $\{\langle K_{j1}^\perp\rangle, \langle\phi_{j1}\rangle\}_{j=2}^m$ and the covariance matrix $\boldsymbol{\Sigma}_{\boldsymbol{K\phi}}{}^{(j1)}$:

$$(K_{j1}^\perp, \phi_{j1}) \sim \mathcal{N}(\langle K_{j1}^\perp\rangle, \langle\phi_{j1}\rangle, \boldsymbol{\Sigma}_{\boldsymbol{K\phi}}^{(\boldsymbol{j1})}). \tag{55}$$

For better numerical stability, the Cholesky decomposition [83] $\boldsymbol{\Sigma}_{\boldsymbol{d}} = \mathbf{L}\mathbf{L}^\top$ into two uniquely determined, lower-triangular matrices $\mathbf{L}$, is performed and Eq. (53) is reformulated as

$$-\ln\mathcal{L} \propto \frac{1}{2}\left[2\sum_{a=1}^{n}\ln(L_{aa})\,\mathbf{x} + \mathbf{x}^\top\mathbf{x}\right], \tag{56}$$

where $\mathbf{x} = \mathbf{L}^{-1}\mathbf{d}$ and $L_{aa}$ are the diagonal elements of $\mathbf{L}$.

The numerical stability can be further improved by employing a regularized version of the covariance matrix, $\boldsymbol{\Sigma}_{\boldsymbol{d}}^{(\lambda)} = \boldsymbol{\Sigma}_{\boldsymbol{d}} + \lambda\mathbf{I}_n$, where $\mathbf{I}_n$ is the identity matrix and $\lambda \ll 1$ is a regulator with the default value $\lambda = 0$. We explicitly checked that the spectral decomposition and the Cholesky decomposition lead to comparable results, that these are stable and that the associated numerical uncertainties are negligible.

Since the Fisher information $I(\alpha_{\mathrm{NP}}) = -\mathbb{E}[\frac{\partial^2\ln\mathcal{L}}{\partial\alpha_{\mathrm{NP}}^2}]$, i.e., the curvature of the log-likelihood with respect to $\alpha_{\mathrm{NP}}$, is invariant under linear rescaling of $\mathbf{d}$, so are the confidence intervals for $\alpha_{\mathrm{NP}}$. This was checked explicitly in the KIFIT code by varying the normalization of $\mathbf{d}$.

Having defined the log-likelihood for one set of independent isotope shifts, the generalization to a combined log-likelihood is straightforward: Assuming zero correlation between the datasets, the total log-likelihood corresponds to the direct sum of the log-likelihoods $\ln\mathcal{L}^{(E)}$, associated with the chemical elements (or independent datasets) $E = 1, 2, \ldots$:

$$-\ln\mathcal{L}(\alpha_{\mathrm{NP}}) = -\sum_{E}\ln\mathcal{L}^{(E)}(\alpha_{\mathrm{NP}}). \tag{57}$$

For a fixed value of $\alpha_{\mathrm{NP}}$ and a set of input and fit parameter samples [see Eqs. (14), (55)], the code evaluates this sum and computes the $\Delta\chi^2$ values

$$\Delta\chi^2 \equiv 2(x - Q[x, p]), \tag{58}$$

where $x = -\ln\mathcal{L}(\alpha_{\mathrm{NP}})$ and $Q[x, p]$ denotes the $p^{\mathrm{th}}$ percentile of the negative log-likelihood values of the full set of $\alpha_{\mathrm{NP}}$ samples. The value of $p$ is a hyperparameter that can be fixed by the user (`min_percentile`, in KIFIT). For $p = 0$, the minimum of the negative log-likelihood, $\min[-\ln\mathcal{L}(\alpha_{\mathrm{NP}})]$, is computed. The use of small values of $p$ can reduce the sensitivity to numerical outliers but too large $p$ values will lead to an excessive downward shift of the $\Delta\chi^2$ values and thus to an overly conservative confidence interval.

In the next section, we illustrate how the window of favored $\alpha_{\mathrm{NP}}$ values is determined in the KIFIT code, while in Sec. III C we discuss how the confidence intervals and their uncertainties are estimated.

The general structure of the KIFIT code is illustrated in Fig. 6.

### B. Determining the search window (search phase)

The purpose of the *search phase* is to determine a favored range of $\alpha_{\mathrm{NP}}$ values. These will serve as a pool for the Monte Carlo sampling that KIFIT uses to estimate the confidence interval. In the code, two different search options are implemented:

(1) The generally faster `detlogrid` option constructs a logarithmic grid of $\alpha_{\mathrm{NP}}$ values, with limits fixed by

$$\left[\alpha_{\mathrm{NP}}\big|_{\mathrm{min}}^{\mathrm{alg}} - \texttt{logrid\_frac}, \alpha_{\mathrm{NP}}\big|_{\mathrm{max}}^{\mathrm{alg}} + \texttt{logrid\_frac}\right], \tag{59}$$

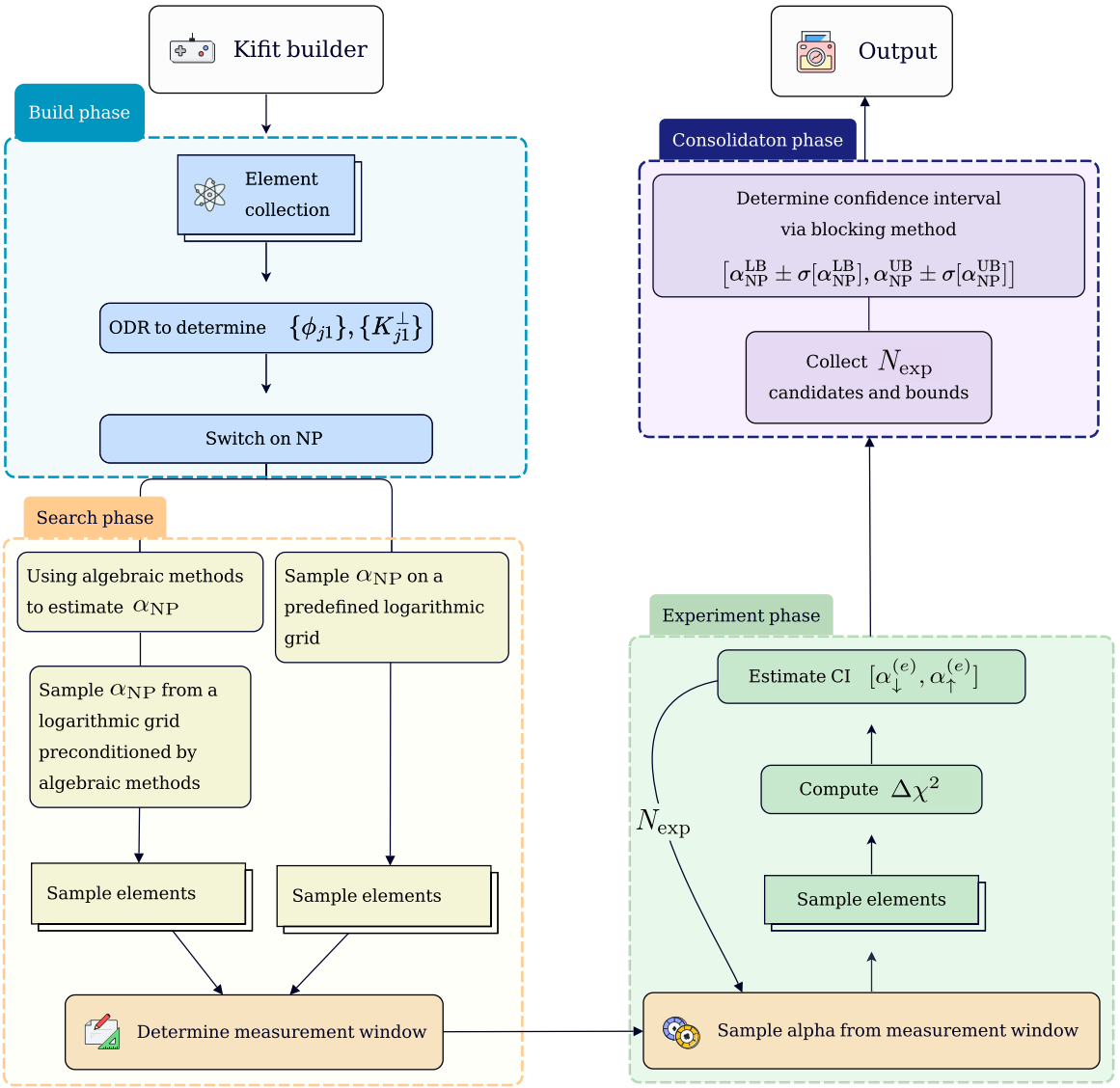


FIG. 6. Illustration of the KIFIT algorithm used to determine a confidence intervals for $\alpha_{\rm NP}$. The algorithm is composed of a *build phase*, a *search phase*, and *experiment phase* and a *consolidation phase*. See Sec. III for a description of the individual steps.

where $\alpha_{\rm NP}|^{\rm alg}_{\rm min}$ and $\alpha_{\rm NP}|^{\rm alg}_{\rm max}$ are the minimum and maximum values found by the algebraic methods [see Eqs. (10), (15), (32), and (33)], for all possible combinations of the experimental input data, while `logrid_frac` is a user-defined additional number of orders of magnitude used to enlarge the $\alpha_{\rm NP}$ scan region.

(2) The `globalogrid` option performs an even more agnostic search on a logarithmic grid between $\alpha_{\rm NP} = 10^{-15}$ and a maximal exponent which increases with $m_\phi$.

As described in the previous section, evaluating the log-likelihood for a given value of $\alpha_{\rm NP}$ involves sampling both the input and the fit parameters.

The number of $\alpha_{\rm NP}$ samples used in the search phase, and the number of input parameters and fit parameters $\{K^{\perp}_{j1}, \phi_{j1}\}^{m}_{j=2}$ per $\alpha_{\rm NP}$ sample can be set by the user. The search window $[\alpha_{\downarrow}, \alpha]$ is then fixed by the minimum and maximum $\alpha_{\rm NP}$ values, $\alpha_{\downarrow}$ and $\alpha$, whose $\Delta\chi^2$ values lie below a $\Delta\chi^2$ value that is sufficiently large to capture all potentially interesting regions in $\alpha_{\rm NP}$ space (see Fig. 7).

Although several orders of magnitude have to be scanned and the Monte Carlo approach only gives reliable results if sufficient statistics are available, we find that both search strategies work and give comparable results (see Fig. 11).

### C. Estimating the confidence interval (experiment phase)

Once the *search window* $[\alpha_{\downarrow}, \alpha]$ is fixed, $N_{\rm expt}$ *experiments* are performed with the aim of determining a reliable confidence interval for $\alpha_{\rm NP}$. In each experiment:

(1) A user-defined number $N_\alpha$ of $\alpha_{\rm NP}$ samples are drawn from the normal distribution

$$\alpha_{\rm NP} \sim \mathcal{N}(\alpha_*, \max(|\alpha_* - \alpha_{\downarrow}|, |\alpha - \alpha_*|)),$$

where $\alpha_*$ is the $\alpha_{\rm NP}$ value within the search window with the lowest negative log-likelihood.

(2) For each of the $\alpha_{\rm NP}$ samples, the input and fit parameters are sampled as described in Eq. (14) and (55).

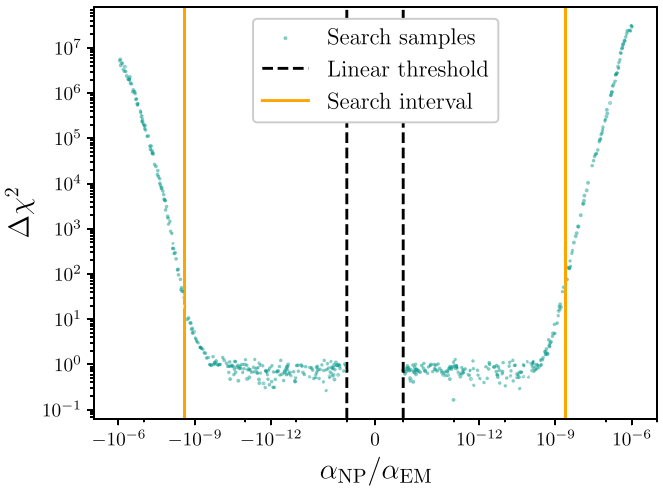


FIG. 7. Output of the *search phase* for a short run of $N_\alpha = 500$ $\alpha_{\rm NP}$ samples and only $N_{\rm expt} = 10$ experiments. The blue scatter shows the $[\alpha_{\rm NP}, \Delta\chi^2(\alpha_{\rm NP})]$ pairs obtained through the procedure described in Sec. III B. The upper and lower limits of the search window are indicated by vertical orange lines, the black dashed lines mark the thresholds between which the $\alpha_{\rm NP}$-scaling is linear.

(3) Values of $\Delta\chi^2$ (Eq. (58)) are computed using the samples determined in the previous steps. Per experiment, we obtain $N_\alpha$ points in the $(\alpha_{\rm NP}, \Delta\chi^2)$ plane (see Fig. 8).

(4) For each experiment $e$, a confidence interval $[\alpha^e_\downarrow, \alpha^e_\uparrow]$ is determined by finding the minimum and maximum $\alpha_{\rm NP}$ samples whose $\Delta\chi^2$ values are below the critical $\Delta\chi^2$ value associated with $2m+1$ degrees of freedom and the number $N$ of $\sigma$ ($N = 2$ being the default value, see red horizontal lines in Fig. 8).

(5) For each experiment $e$, a *best-fit value* $\alpha^e_*$ is determined, defined as the $\alpha_{\rm NP}$ value with the smallest associated negative log-likelihood.

The number of experiments, $N_{\rm expt}$, the number of input and fit parameter samples, the number $N_\alpha$ of $\alpha_{\rm NP}$ samples, and the number $N$ of $\sigma$ are hyperparameters that can be fixed by the user. For a stability analysis, see Appendix D 1.

Finally, the results of the $N_{\rm expt}$ experiments are collected and the final estimation of the confidence interval for $\alpha_{\rm NP}$ is determined in the consolidation phase.

### D. Producing results (consolidation hase)

Since numerical simulations are used in KIFIT to estimate the new physics bounds, we need a robust strategy to compute both the estimation and its uncertainty. To do so, we apply a technique inspired by the *blocking average method* (BAM), which is commonly used to compute statistically independent estimations starting from a simulated set of possibly correlated data [84]. To facilitate the following discussion, we refer to the illustration presented in Fig. 9.

The BAM involves executing the simulation experiment $N_{\rm expt}$ times, thus collecting $N_{\rm expt}$ raw estimations. These are then divided into $B$ blocks of size $N_b$ (purple subsets in the top right of Fig. 9) and each block is used to produce a single estimation of the target variable. To mitigate eventual correlations among simulated data, it is important to choose

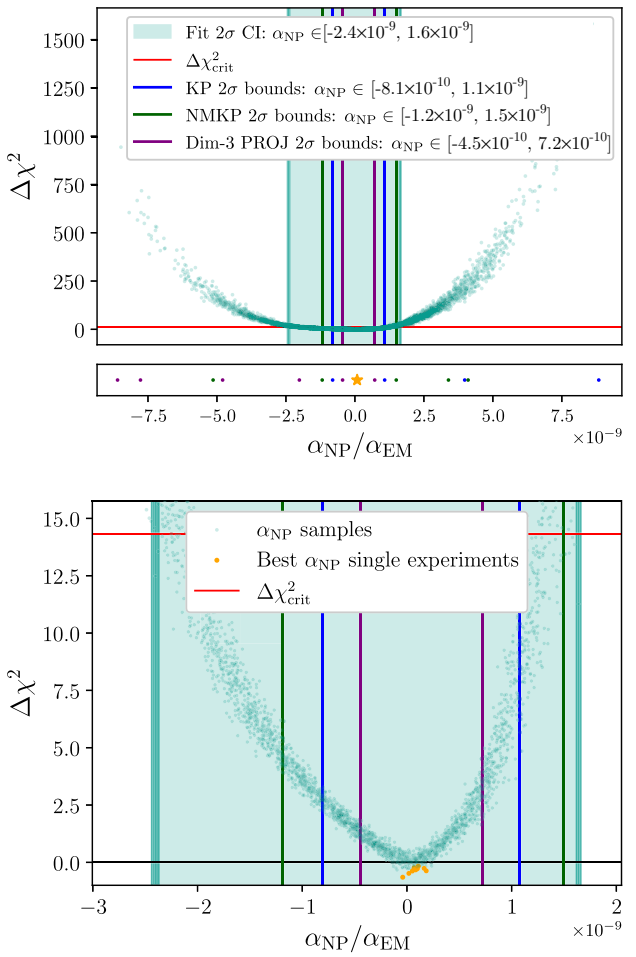


FIG. 8. Output of the *experiment phase* for a short run of $N_\alpha = 500$ $\alpha_{\rm NP}$ samples and only $N_{\rm expt} = 10$ experiments. The teal scatter shows the $[\alpha_{\rm NP}, \Delta\chi^2(\alpha_{\rm NP})]$ pairs obtained through the procedure described in Sec. III C. Some of the $\Delta\chi^2$ values are negative due to the choice of $p = 1$, [see Eq. (58)]. The confidence interval, also shown in teal, is defined as the region in which there are $\Delta\chi^2(\alpha_{\rm NP})$ values below the "critical" $\Delta\chi^2$ value $\Delta\chi^2_{\rm crit}$, indicated by the horizontal red line. The dark teal vertical bars show the uncertainties on the confidence interval. These are estimated by means of the *blocking method* (see Sec. III D). The best-fit $\alpha_{\rm NP}$ value is represented by an orange star, its uncertainty being smaller than its width. The lower plot is an enlargement of the confidence interval in the upper plot. The best $\alpha_{\rm NP}$ values of the $N_{\rm expt}$ experiments are shown in orange.

the size of the blocks such that the estimation computed from each block can be assumed to be independent from those of the other blocks. This is relevant because, if those estimators are independent, their average value and uncertainty stabilizes for increasing number of blocks, according to the central limit theorem.

In our case, the raw estimations correspond to confidence intervals of the form $[\alpha^e_\downarrow, \alpha^e_\uparrow]$, where the superscript refers to the result of the experiment $e$, $1 \leqslant e \leqslant N_{\rm expt}$. In Ref. [84], and more in general in the context of numerical simulations, the estimation for each block is defined as the average value of the data in the block. We use instead a more conservative approach, with the intention of estimating bounds in the least aggressive way possible. Taking the estimation of the lower

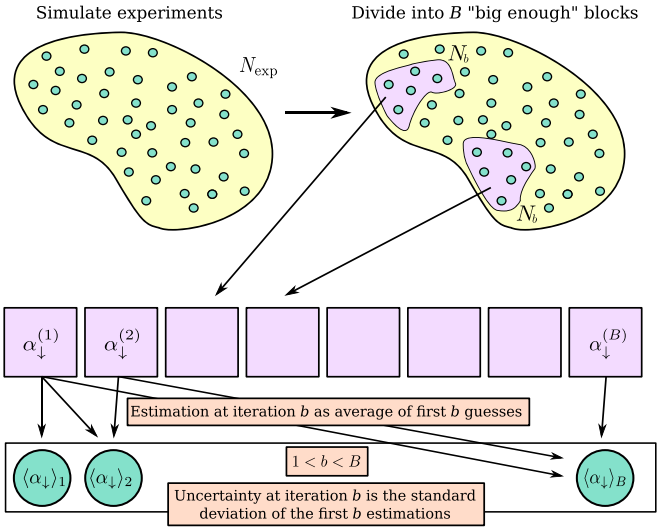


FIG. 9. Illustration of the blocking method applied to the estimation of the lower bound (for upper bound: $\alpha_\downarrow \to \alpha$). The $N_{\text{expt}}$ simulated experiments are divided into $b = 1, \ldots, B$ blocks, for each of which the minimum lower bound on $\alpha_{\text{NP}}$, $\alpha_\downarrow^{(b)}$, is computed. The estimations $\{\alpha_\downarrow^{(b)}\}_{b=1}^{B}$ are then used to compute an iterative average, the final estimation for the lower bound being $\langle\alpha_\downarrow\rangle_B$.

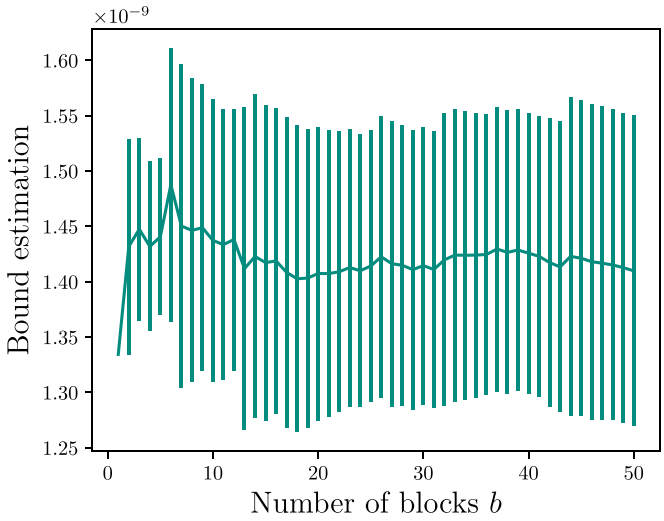


FIG. 10. Blocking method applied to the estimation of the upper bound on $\alpha_{\text{NP}}/\alpha_{\text{EM}}$ after executing the procedure described in Sec. III D. These results have been collected from $N_{\text{expt}} = 500$ experiments divided into $B = 50$ blocks.

bound as an example, we define an estimator as the minimum of values collected in the block $b$:

$$\alpha_\downarrow^{(b)} \equiv \min_{e \in b} \alpha_\downarrow^{e}. \tag{60}$$

A similar procedure can be used to compute the upper bound, considering instead the maximum value in the block. Since the $N_{\text{expt}}$ experiments are considered to be independent (contrary to the time-series simulation in Ref. [84]), we can also assume the estimators in Eq. (60) to be statistically independent.

The estimation of the lower bound and its uncertainty based on $B$ blocks are computed as follows:

$$\langle\alpha_\downarrow\rangle_B \equiv \frac{1}{B}\sum_{b=1}^{B} \alpha_\downarrow^{(b)}, \tag{61}$$

$$\sigma[\alpha_\downarrow]_B \equiv \sqrt{\frac{1}{B-1}\sum_{b=1}^{B}(\alpha_\downarrow^{(b)} - \langle\alpha_\downarrow\rangle_b)^2}, \tag{62}$$

where $\langle\alpha_\downarrow\rangle_b$ in the second equation corresponds to the estimator defined in the first equation, computed iteratively for any $b \leqslant B$. A similar approach is used to compute the final estimation and uncertainty for the upper bound. The evolution of $\langle\alpha_\downarrow\rangle_B$ and $\sigma[\alpha_\downarrow]_B$ for increasing number of blocks is shown in Fig. 10. Ideally, if the block size ensures that the estimates obtained from each block are independent of one another, the target variable estimator stabilizes and the variance estimator converges to the true variance of the mean (see Sec. 4 of Ref. [84]). The number of blocks $B$ is computed from the number of experiments and the block size, both of which can be set by the user. The ideal values for $N_{\text{expt}}$ and the block size are ones that ensure the stability of the code. See Appendix D 1 for a more detailed discussion.

The final confidence intervals for $\alpha_{\text{NP}}$ provided by KIFIT take all $B$ blocks into consideration. We apply the following conservative definition:

$$\left[\alpha_{\text{NP}}^{\text{LB}}, \alpha_{\text{NP}}^{\text{UB}}\right] = \left[\langle\alpha_\downarrow\rangle_B - N\,\sigma[\alpha_\downarrow]_B, \langle\alpha\rangle_B + N\,\sigma[\alpha]_B\right], \tag{63}$$

where $N$ corresponds the number of $\sigma$ of the confidence interval. In Fig. 8, the uncertainties on the $2\sigma$ confidence interval are shown as darker teal bands.

Besides the confidence interval, the KIFIT code provides a *best* $\alpha_{\text{NP}}$ value (orange star in the upper plot of Fig. 8). This corresponds to the median of the best $\alpha_{\text{NP}}$ values $\{\alpha_*^e\}_{e=1}^{N_{\text{expt}}}$ (marked by orange dots in the lower plot in Fig. 8) found in the *experiment phase* (Sec. III C). The uncertainty in the *best* $\alpha_{\text{NP}}$ value is estimated by the standard deviation of the same set of values $\{\alpha_*^e\}_{e=1}^{N_{\text{expt}}}$.

Exclusion plots such as the one shown in Fig. 11 are obtained by repeating the procedure described in Secs. III A–III D for multiple values of the mediator mass $m_\phi$, i.e., for different values of the $X$ coefficients [see, e.g., Eq. (8)].

Figure 11 compares the $2\sigma$ bounds obtained by the KIFIT algorithm (orange) to those obtained using the algebraic methods for subsets of the isotope shift data. The results using the minimal King plot formula [Eq. (10)] are shown in blue, the no-mass King plot results [Eq. (15)] in green, and the results using the projection method [Eq. (20)] with $n = 3$ in purple. For each of these methods, the most stringent limits on $\alpha_{\text{NP}}$ are connected by lines of matching color. The horizontal black dashed lines indicate the thresholds between which the plot scale is linear.

As in Fig. 8, the orange stars and bars represent the best-fit points and their $1\sigma$ uncertainties, as obtained by KIFIT. Note that, at high-mass values, the KIFIT sampling becomes more challenging: the points drawn to evaluate the likelihood are more widely spread around the curve that they trace, and consequently the confidence intervals produced by the experiments exhibit greater variance than at low masses. To mitigate this effect, it is advisable to improve the Monte Carlo sampling, for example by increasing the number of

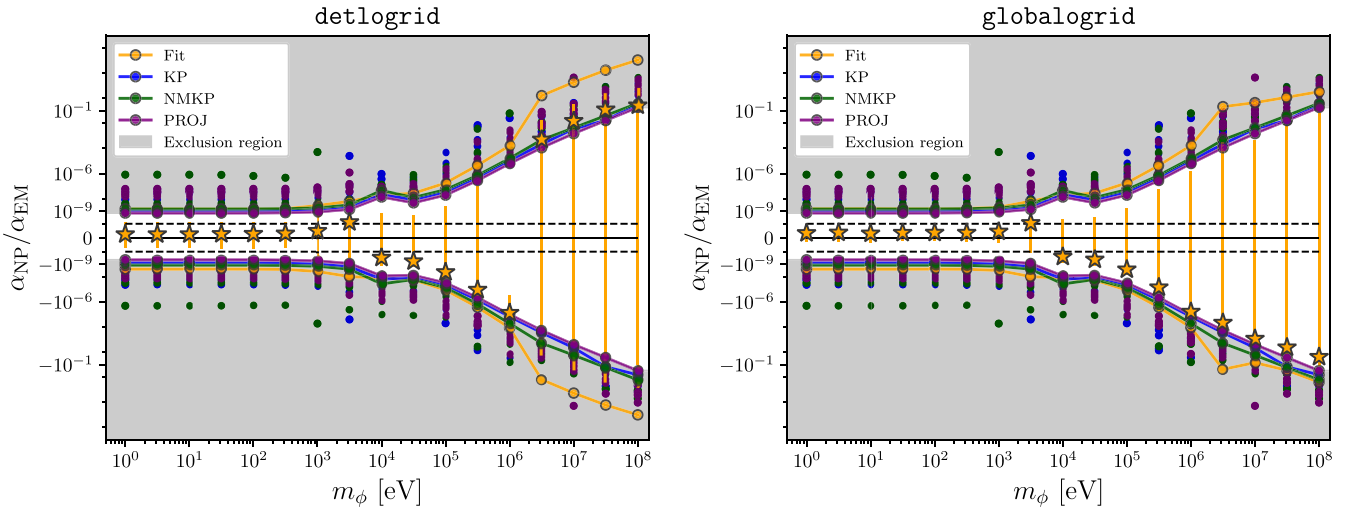


FIG. 11. Output of the KIFIT code for the Ca_WT_Aarhus_PTB_2024 dataset, showing the $2\sigma$ upper and lower bounds on the new physics coupling $\alpha_{\rm NP}/\alpha_{\rm EM}$ as a function of the mass $m_\phi$ of the new boson with orange connected round markers. The estimation is repeated for the two different *search phase* approaches (see Sec. III B): Left detlogrid, adopting the algebraic-induced logarithmic grid, and right globalogrid, using the global logarithmic grid. The orange stars and bars indicate the best-fit points and the associated uncertainties. The bound obtained via the KIFIT algorithm (orange) is compared with the algebraic results: minimal KP [Eq. (10)] in blue, NMKP [Eq. (15)] in green and projection method [Eq. (20)] with $n = 3$ in purple. The solutions for the different permutations are illustrated by single markers, whereas the envelopes of the most stringent limits are indicated with lines of the same color. Since the three algebraic methods lead to very similar results, only the purple markers are visible in most cases. For better readability, the regions excluded by any of the plotted bounds are shaded gray. The horizontal black dashed lines indicate the thresholds between which the plot scale is linear.

sampled points, using variance reduction techniques, or adopting adaptive strategies in which computational effort grows in proportion to the mass under analysis. In this example we have kept the simulation parameters fixed, so what we observe at high masses is, unsurprisingly, larger error bars. Finally, since we employed a very conservative technique to define the bounds estimates, it is also reasonable to see the bounds widen at high masses.

### E. Comparison to a previous King plot fit

As already mentioned in the introduction, the geometric construction used by KIFIT (see Sec. III A) is inspired by the King plot fit proposed in Ref. [36], but there are some notable differences in the definition of the log-likelihood and the fit parameters. These differences will be discussed in this section.

The fit in Ref. [36] was developed for the case of similar uncertainties across all transitions and isotope pairs (which was the case for the isotope shift data available at that time) and under the (strong) assumptions of uncorrelated uncertainties. In our notation, the $\chi^2$ function proposed in Ref. [36] takes the form

$$\chi_a^2 = \sum_{i=1}^{m} \left( \frac{\hat{d}_i^a}{\sigma[\tilde{\nu}_i^a]} \right)^2, \quad \hat{d}_i^a = \tilde{\nu}_i^a - \left( K_{i1} + \frac{\alpha_{\rm NP}}{\alpha_{\rm EM}} \tilde{\gamma}^a X_{i1} \right). \tag{64}$$

To illustrate the main difference between this definition of $\chi^2$ and Eq. (58), let us consider the two-dimensional setup illustrated in Fig. 4, which is characterized by one inclination angle $\phi_{21}$. In this case the elements $\hat{d}_i^a$ take the particularly simple form

$$\hat{d}_1^a = \|\boldsymbol{d}^a\| \sin\phi_{21}, \quad \hat{d}_2^a = \|\boldsymbol{d}^a\| \cos\phi_{21}, \tag{65}$$

such that Eq. (64) reads

$$\chi_a^2 = \|\boldsymbol{d}^a\|^2 \left\{ \left( \frac{\sin\phi_{21}}{\sigma[\tilde{\nu}_1^a]} \right)^2 + \left( \frac{\cos\phi_{21}}{\sigma[\tilde{\nu}_2^a]} \right)^2 \right\}, \tag{66}$$

where $\|\boldsymbol{d}^a\|^2 = \|\boldsymbol{\Delta}^a\| \cos\phi_{21}$.

Equation (66) explicitly shows how separately normalizing the components of $\boldsymbol{d}^a$ by the uncertainties $\sigma[\tilde{\nu}_i^a]$ distorts the fit: If the dataset under consideration has a direction with significantly smaller uncertainties, e.g., $\sigma[\tilde{\nu}_1^a] \gg \sigma[\tilde{\nu}_2^a]$, the minimization of Eq. (66) will lead to a rotation of the King line, even if this does not reduce the overall distance of the points to the fitted line. Instead, KIFIT minimizes $\|\boldsymbol{d}^a\|(\Sigma_{\boldsymbol{d}}^{ab})^{-1}\|\boldsymbol{d}^b\|$, where $\Sigma_{\boldsymbol{d}}^{ab}$ is an estimate of the covariance of $\|\boldsymbol{d}^a\|$ and $\|\boldsymbol{d}^b\|$. In this way all directions are treated equally, while correlations between the uncertainties are taken into account.

Note also that Eq. (66) does not take into account the fact that a King plot fit cannot capture new physics-induced constant shifts of all data points [see discussion around Eqs. (43)–(45)] and will therefore tend to lead to overly aggressive bounds on $\alpha_{\rm NP}$.

Further improvements with respect to the fit proposed in Ref. [36] are the estimation of the uncertainties on the best-fit point and the confidence interval by means of the blocking average method (see Secs. III C and III D); the development of an extensible code framework that allows us to combine the isotope shift data of several elements in a single fit; an extensive set of numerical tests that ensure the internal consistency

of the code and compare KIFIT results in PYTHON with results obtained with *Mathematica*.

In the following section, we provide a comparison of the KIFIT results with results obtained by means of the algebraic methods discussed in Sec. II.

## IV. COMPARISON OF FIT AND ALGEBRAIC METHODS

In Sec. II, we reviewed the algebraic methods to extract bounds on $\alpha_{\rm NP}$ from King plots, whereas in Sec. III, we presented the King plot fit KIFIT. Although both methods are based on the King plot formalism, they adopt different strategies when it comes to setting bounds on $\alpha_{\rm NP}$. This becomes most evident by stating the questions that either method addresses:

*Algebraic methods*

(1) $\langle\alpha_{\rm NP}\rangle$: Given a dataset of dimension as specified in Table I, which value of $\alpha_{\rm NP}$ is required to perfectly describe the experimental central values of the data points in the King plot?

(2) $\sigma[\alpha_{\rm NP}]$: How large is the impact of the experimental uncertainties on the value of $\alpha_{\rm NP}$?

*King plot fit*

(1) $\{K_{j1}^{\perp}, \phi_{j1}\}_{j=2}^{m}$: What is the best linear fit, given the central values and uncertainties on the data points in the King plot (mass-normalized isotope shifts)?

(2) Given the central values and uncertainties on the fit parameters and on the data points, what is the likelihood [Eq. (52)] associated with the set of sample $\alpha_{\rm NP}$ values?

(3) $[\alpha_{\rm NP}^{\rm LB}, \alpha_{\rm NP}^{\rm UB}]$: What are the minimum and maximum $\alpha_{\rm NP}$ values whose $\Delta\chi^2$ values are below the critical $\Delta\chi^2$ value associated with $2m+1$ degrees of freedom and $N\sigma$?

In the rest of the section, we contrast these approaches in more detail, discuss their respective advantages and disadvantages, present our results, and suggest when to apply which method.

### A. Blind directions

Since both approaches are based on the King plot formalism, they inherit the blind directions of the King plot: As discussed in Sec. II A, in particular in Eqs. (11) and (12), the King plot method is only sensitive to effects that have a component orthogonal to the mass shift or the field shift, i.e., that lead to a "misalignment" both in transition space and in isotope pair space. In a standard King plot in transition space such a misalignment manifests itself in a deviation from the King line [Eq. (5)]. This is the effect that the King plot fit looks for. Equivalently, it can be viewed as a component orthogonal to the plane of King linearity fixed by the basis vectors $\boldsymbol{\mu}$ and $\boldsymbol{\delta\langle r^2\rangle}$ (or equivalently $\mathbf{1}$ and $\tilde{\mathbf{v}}_1$, as in Fig. 2) in isotope-pair space. This is the effect exploited by the algebraic methods and the nonlinearity decomposition [Eq. (23)].

The blind directions of the King plot method and their manifestations in the algebraic methods and on the King plot fit KIFIT are summarized in Table II: Using the notation of Eq. (12), they can be described by vanishing determinants of the matrix of electronic or nuclear factors or, in KIFIT, either by an alignment of the electronic coefficients $X_j/X_1$ and $F_{j1} = F_j/F_1$ leading to a vanishing coefficient $X_{j1} \to 0$, or by a global shift of the King line, which cannot be distinguished from a redefinition of the electronic mass shift coefficient $\mathcal{K}$ (see Fig. 4).

TABLE II. Blind directions of the King plot method and how they manifest themselves in the algebraic methods and in the fit. The matrices $\mathcal{M}$ and $\mathcal{N}$ are defined in Eq. (12) and (16) for the cases of the simple King plot and the no-mass King plot, respectively, whereas $X_{j1}$ and $\langle\tilde{\gamma}\rangle$ are defined in Eqs. (41) and (43), respectively.

| Algebraic methods | KIFIT |
|---|---|
| $\det(\mathcal{N}) \to 0$ | $\tilde{\gamma}^a \to \langle\tilde{\gamma}\rangle\ \forall\ a$ |
| $\det(\mathcal{M}) \to 0$ | $X_{j1} \to 0\ \forall\ j$ |

Another common feature of the fit and the algebraic methods, which is inherited from the King plot, is the insensitivity to the experimental uncertainties parallel to the King line: Whereas this is true by construction for the King plot fit (see Fig. 4), it is less obvious in the case of the algebraic methods. In Appendix C, we check explicitly that the effect of the isotope shift uncertainties parallel to the King line has a negligible impact on $\sigma[\alpha_{\rm NP}]$.

### B. Geometric construction and form of datasets

The most obvious difference lies in the geometric constructions. The algebraic methods compare volumes constructed from a combination of data points and predictions (see Fig. 1), providing one constraint on $\alpha_{\rm NP}$ per dataset. It is for this reason that the datasets used by the algebraic methods must have a fixed size (see Table I).

The fit, on the other hand, minimizes the distances $\|\boldsymbol{d}^a\|$ of the data points $\tilde{\boldsymbol{\nu}}^a$ from the set of King lines $\{\ell^{(a)}\}_{a=1}^{n}$, which are determined by a combination of the best linear fit to data, $\ell^{(0)}$, and the predicted nonlinearity induced by new physics (see Fig. 4). Since the fit is based on a log-likelihood, which sums over the data points [Eq. (52)], it can handle datasets of dimension $(n, m)$, with $3 \leqslant n$ and $2 \leqslant m$, but where $n$ and $m$ are independent (see Table I), and also combine multiple datasets, enabling global fits to data. This makes the fit particularly valuable for the search for new physics, which is expected to couple in the same way to electrons and neutrons, irrespective of the element.

#### 1. Size of datasets

Whereas the algebraic methods work best for small datasets, the fit relies on the presence of sufficiently large and diverse datasets. When this is not the case, there is a risk of overfitting. Overfitting happens when a statistical model is too expressive for a given dataset. The optimal fit parameters are obtained by learning the statistical fluctuations or any other source of error. For example, using a dataset with two points only, we would obtain a perfect interpolation and could define a margin for new physics in the form of a finite value for $\sigma[\alpha_{\rm NP}]$, but at the same time, we would be performing maximum over-fitting: All data are used to fix the fit parameters $\{K_{j1}^{\perp}, \phi_{j1}\}_{j=2}^{m}$ and the bound on the remaining fit parameter $\alpha_{\rm NP}$ is meaningless. Indeed, in order to fit $2(m-1)+1 = 2m-1$ degrees of freedom with $n$ data points, each of which

TABLE III. Estimates of the $1\sigma$ confidence interval for $\alpha_{\rm NP}$ for $m_\phi = 1$ eV. The first column shows the central value of $\alpha_{\rm NP}$ [Eq. (10)] and its uncertainty obtained using linear error propagation [Eq. (C11)]. The uncertainties in the second column were estimated using a Monte Carlo approach [see Eqs. (14) to (10)] with 2000 samples. Both for column 1 and column 2, those subsets of the data were employed that lead to the most stringent bounds on $\alpha_{\rm NP}$. The KIFIT results are listed in the last column. These were obtained using a search phase on a `detlogrid` with `logrid_frac`=2500 $\alpha_{\rm NP}$ samples and 200 input and fit parameter samples per $\alpha_{\rm NP}$ sample. The experiment phase consisted of 150 experiments, with 1000 $\alpha_{\rm NP}$ samples each and 500 input and fit parameter samples per $\alpha_{\rm NP}$ sample. The experiments were divided into blocks of size 25.

| Dataset | $(\alpha_{\rm NP} \pm \sigma[\alpha_{\rm NP}])\vert^{(1)}_{\rm KP}$ | $(\alpha_{\rm NP} \pm \sigma[\alpha_{\rm NP}])\vert^{\rm MC}_{\rm KP}$ | $[\alpha^{\rm LB}_{\rm NP} \pm \sigma[\alpha_\downarrow]_B,\ \alpha^{\rm UB}_{\rm NP} \pm \sigma[\alpha]_B]$ |
|---|---|---|---|
| `Ca3pointTEST` | $(1.36 \pm 4.84) \times 10^{-10}$ | $(1.36 \pm 4.81) \times 10^{-10}$ | $[-3.51 \pm 0.16, 3.59 \pm 0.13] \times 10^{-11}$ |
| `Ca4pointTEST` | $(-0.14 \pm 4.50) \times 10^{-11}$ | $(-0.14 \pm 4.50) \times 10^{-11}$ | $[-3.44 \pm 0.15, 3.29 \pm 0.09] \times 10^{-11}$ |
| `Ca10pointTEST` | $(0.19 \pm 1.35) \times 10^{-10}$ | $(0.19 \pm 1.31) \times 10^{-10}$ | $[0.32 \pm 0.07, 1.65 \pm 0.08] \times 10^{-10}$ |
| `Ca_PTB_2015` | $(0.65 \pm 1.10) \times 10^{-8}$ | $(0.65 \pm 1.10) \times 10^{-8}$ | $[-7.04 \pm 0.20, 8.04 \pm 0.50] \times 10^{-10}$ |
| `Camin` | $(1.36 \pm 1.12) \times 10^{-9}$ | $(1.36 \pm 1.1) \times 10^{-9}$ | $[-0.91 \pm 0.03, 1.0 \pm 0.05] \times 10^{-10}$ |
| `Ca24min` | $(1.36 \pm 4.70) \times 10^{-10}$ | $(1.36 \pm 4.74) \times 10^{-10}$ | $[-2.66 \pm 0.13, 2.55 \pm 0.07] \times 10^{-11}$ |
| `Ca_WT_Aarhus_PTB_2024` | $(1.36 \pm 4.70) \times 10^{-10}$ | $(1.36 \pm 4.72) \times 10^{-10}$ | $[-1.99 \pm 0.04, 1.45 \pm 0.05] \times 10^{-9}$ |

contributes an additional scalar constraint (distance $\|\boldsymbol{d}^a\|$), $n \geqslant 2m - 1$ data points are required (see also Table I).

datasets with just 2 transitions and 2 isotope pairs are not considered in King plots for precisely this reason. However, since the statistical uncertainty associated with the spread of the points is expected to scale as $1/\sqrt{n}$, the fit, which minimizes the distances from the data points to the King line, will significantly underestimate the bounds on $|\alpha_{\rm NP}|$ in the limit of sparse data.

In Appendix E, we generate mock data starting from a set of linear relations. This allows us to study the impact of data sparsity on the fit results in more detail.

### 2. *Numerical comparisons*

To explicitly compare results obtained using the algebraic methods and the fit, we list in Table III the values of $\sigma[\alpha_{\rm NP}]$ estimated by means of linear error propagation through Eq. (10) ($\sigma[\alpha_{\rm NP}]\vert^{(1)}_{\rm KP}$, first column) and the Monte Carlo approach outlined in Sec. II A, in particular in Eqs. (13) and (14) ($\sigma[\alpha_{\rm NP}]\vert^{\rm MC}_{\rm KP}$, second column), as well as the $1\sigma$ confidence interval determined in KIFIT by the BAM, Eq. (63) (last column). We observe good agreement between the linear uncertainty propagation and the Monte Carlo approach. In contrast, the KIFIT results show some deviations. Notably, for all minimal datasets (two transitions and three isotope pairs), the fit results are roughly an order of magnitude stronger. However, we notice that the discrepancy is lifted for larger datasets, such as `Ca4pointTEST` and `Ca10pointTEST` (each with two transitions and four or ten isotope pairs) and `Ca_WT_Aarhus_PTB_2024` (four transitions and three isotope pairs). For a description of these datasets and the relevant references, see Appendix F.

This behavior can also be observed in the exclusion plot in Fig. 12, which shows the bounds on $\alpha_{\rm NP}$ for the minimal dataset `Ca24min`. Here the fit bounds (orange) appear to be nearly two orders of magnitude more stringent than the bounds obtained using the minimal algebraic method [Eq. (10), blue] and the projection method [Eq. (20), purple]. Figure 13 shows the same fit result as Fig. 12, but complemented with those using the minimal dataset `Ca_PTB_2015` and `Ca_WT_Aarhus_PTB_2024`, which combines `Ca_PTB_2015` and `Ca24min` to a dataset for three isotope pairs and four transitions. The fit and the algebraic results using `Ca_WT_Aarhus_PTB_2024` show significantly better agreement.

A similar situation can be observed in Fig. 14, which combines `Ca_WT_Aarhus_PTB_2024` with `Yb_Kyoto_MIT_GSI_MPIK_2024`, a set of Yb isotope shifts for four isotope pairs and five transitions. The fit result for Yb must be interpreted with caution since it is known to contain SM nonlinearities, which are, however, not taken into account by the current version of KIFIT. In Appendix E, we discuss the impact of data sparsity in more detail.

In Figs. 13 and 14, the fit appears to lose sensitivity more quickly than the algebraic methods at the high-mass end. We trace this behavior back to the `Ca_PTB_2015` dataset, which starts to lose sensitivity comparatively rapidly at around $m_\phi = 10^{-6}$ eV. Since the algebraic bound in Fig. 13 shows the

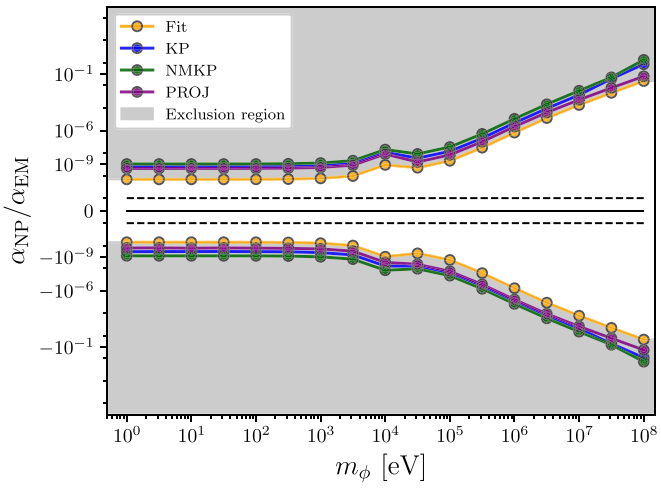


FIG. 12. Comparison of the fit results with the algebraic results [KP: Eq. (10), NMKP: Eq. (15), PROJ: Eq. (20)] for the minimal dataset (three isotope pairs, two transitions) `Ca24min`. For better readability, the regions excluded by any of the plotted bounds are shaded gray, even if these are considered too aggressive in the case of `Ca24min` (see text for discussion). The black dashed lines indicate the thresholds between which the scaling in the plot is linear.

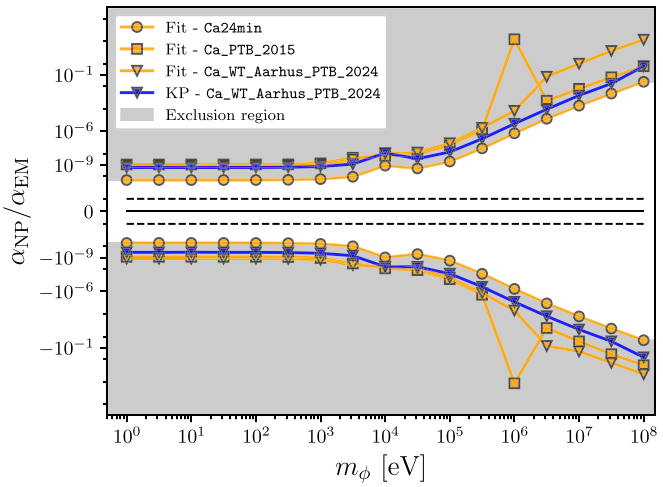


FIG. 13. Fit results for two datasets of dimensions $(n, m) = (3, 2)$ (`Ca24min`, `Ca_PTB_2015`) and their combination of dimensions $(3, 4)$ (`Ca_WT_Aarhus_PTB_2024`). The most stringent algebraic bounds [KP: Eq. (10)] for `Ca_WT_Aarhus_PTB_2024` correspond to the algebraic bounds for `Ca24min` and are shown in blue. Whereas the difference between the fit results and the algebraic results is sizable for the $(3, 2)$-dimensional datasets, the agreement is better for `Ca_WT_Aarhus_PTB_2024`.

envelope of the bounds, and the algebraic bounds for `Ca24min` turn out to be more stringent, the behavior of the `Ca_PTB_2015` bound is not visible in the algebraic results plotted in Figs. 13 and 14. Nonetheless, the robustness of the fit in the high-mass region could be improved by ameliorating the Monte Carlo sampling discussed in Sec. III D and by increasing the resolution in $m_\phi$. For completeness, we performed a series of higher-resolution simulations executing the algebraic KP method on the `Ca_PTB_2015` dataset (equivalent to the blue curve in Fig. 13, but considering eighty mass values in the same range) and we were able to resolve similar spikes to the one shown in the KIFIT bound in Fig. 13.

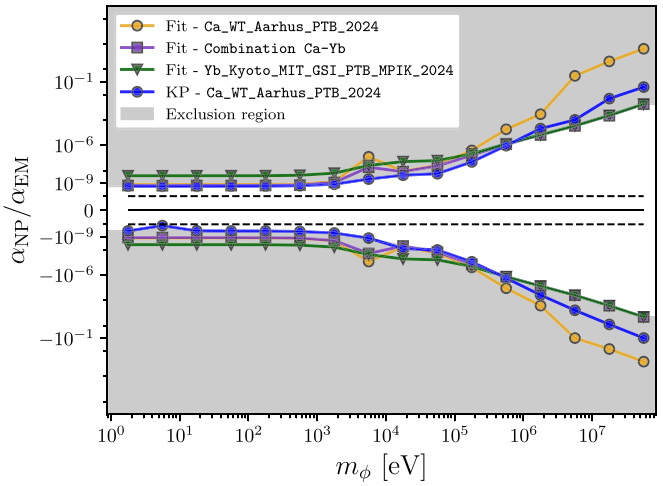


FIG. 14. Fit results for a Ca dataset, a Yb dataset, and the combination thereof. The (most stringent) algebraic results for the Ca dataset are also shown.

## V. CONCLUSIONS AND OUTLOOK

Over the past few years, several precision isotope shift measurements have been performed, spurring the development of a wide range of King-plot–inspired methods to search for new physics and study nuclear structure. In this work, we systematically compare the available analysis methods, complementing them with the no-mass generalized King plot and the nuclear input King plot formulas, and taking a first step toward a global analysis of isotope shift data with our novel fit framework KIFIT.

The key strengths of KIFIT originate from its construction based on a log-likelihood: While the algebraic methods require datasets with $n = m$ or $n = m + 1$ isotope pairs for $m$ transitions, the fit is flexible with respect to $n$ and $m$. It thus avoids the omission of data or cherry-picking the subset that yields the most stringent bound on new physics. Under the assumption of uncorrelated measurements, it further allows us to combine isotope shifts from different elements.

This is particularly valuable for the search for new bosons whose couplings to atomic nuclei do not introduce element-dependent parameters. The standard model extension consisting of a new boson coupling linearly to neutrons and electrons, which is commonly investigated using King plots, is particularly predictive. KIFIT can, for the first time, test this model across elements, setting *global* bounds on the product of the new boson's couplings to neutrons and to electrons, for new boson masses spanning eight orders of magnitude.

The fit does, however, rely on the existence of sufficiently large datasets, since it tends to underestimate the margin for new physics when data is sparse. For this reason, measuring isotope shifts and nuclear masses in larger arrays of isotopes would not only provide new opportunities to resolve higher-order nuclear effects, but also allow more stable and reliable bounds on new physics to be established. Example systems with a large number of even stable isotopes are Zn (five stable isotopes of which four are even, see Ref. [58] for recent isotope shift data), Sn [85] (ten stable isotopes of which seven are even, plus one trace radioisotope with $\tau_{1/2} \sim 10^5$ y), Ba (six stable isotopes of which four are even, plus one even isotope with a half-life $\tau_{1/2} \sim 10^{21}$ y, measured so far with 100–400 MHz uncertainty [86]) and Cd (six stable isotopes of which five are even, plus one even isotope with $\tau_{1/2} \sim 10^{19}$ y; Ref. [57] reached a resolution of few MHz for isotope shifts in two transitions), plus the hitherto unexploited metastable isotopes in Ca and Yb, among others.

Recently, several additional isotope shift measurements were completed: Ref. [87] achieved a precision below 10 Hz in the 431 nm transition in neutral Yb, Ref. [88] reduced the uncertainty of isotope shifts in the 369 and 935 nm transitions in $Yb^+$ to the sub-MHz level, Ref [89] measured isotope shifts in four metastable state transitions in $Yb^+$ at 30 MHz and sub-MHz level. The isotope shift in the fine-structure splitting of $P$ states in $Kr^+$ was measured at sub-MHz precision in Ref. [90]. Isotope shifts measured at sub-10 MHz precision in $Th^{3+}$ were reported in Ref. [91]. Reference [92] reported Hg, as well as the aforementioned Cd, as a promising candidate for King plots, having seven stable isotopes of which five are even. Reference [93] measured isotope shifts among three even isotope pairs in the 254 nm transition at a precision of

0.3 MHz (improved to 20 kHz by Ref. [94] for 1 isotope pair) and constructed a King plot using the 546 nm isotope shifts measured in Ref. [95] at a precision of 50 kHz. The 266 nm transition was measured in two isotope pairs in Refs. [96–98]. Reference [99] determined isotope shifts in three isotope pairs in Rydberg transitions of Sr (including the odd isotope $^{87}$Sr) at a sub-MHz precision, while Ref. [100] measured isotope shifts in the same isotope pairs for two optical transitions at 20 and kHz precision, and performed a King plot analysis revealing a nonlineairity. Reference [101] extended the King plot analysis to isotope shifts in diatomic molecules. Theoretical studies have identified several suitable clock transitions in highly charged ions, thereby extending the pool of transitions suitable for future isotope shift investigations [102,103]. These developments add to the growing treasure of isotope shift data and pave the path toward high-precision isotope shifts in a multitude of elements and even molecules.

Whereas the current version of the KIFIT code is limited to King plots that are linear within uncertainties, King plot nonlinearities could be included in future versions, e.g., by subtracting them as in Ref. [43], provided accurate predictions or complementary experimental input are available. The framework provided by the KIFIT code might even be applied to obtain insights into higher-order nuclear effects in a data-driven way, as was suggested in Ref. [50].

Note that all King plot searches for new physics, including KIFIT, rely on predictions for the electronic coefficients that enter the new physics term, while the analysis of nonlinear King plots using KIFIT-like setups would additionally require predictions for higher-order SM terms. For this reason, it may be beneficial to focus on elements whose dominant King nonlinearities are higher-order mass shifts, in which case the nuclear contributions can be determined from experimental data and the electronic coefficients can be predicted with comparatively good precision [43,52]. In systems where the second-order mass shift is the only resolvable King nonlinearity, the nuclear input King plot formula presented in this work can be employed to extract the new physics coupling from isotope shift data for just two transitions and four isotope pairs.

In conclusion, we encourage experimentalists to measure isotope shifts across additional transitions and isotopes, even if the initial precision is lower than that of the best current measurements. Additional data points can help eliminate higher-order effects in the isotope shift equations and stabilize the bounds on new physics. They also provide new insights into nuclear structure and can thus be used to refine nuclear models. If new isotope shifts are measured before the corresponding isotope masses, the no-mass King plot and its generalized version facilitate a first analysis of the new data and indicate the required precision of the mass measurements to achieve competitive sensitivity to new physics and the nuclear shape. Ultimately, it is the combination of new measurements, advancements in atomic and nuclear structure theory, and global (King plot) analyses that will enhance the sensitivity to new physics and to nuclear effects.

## ACKNOWLEDGMENTS

We thank Julian Berengut for providing the $X$ coefficients of Yb that he calculated using the open-source atomic structure code AMBIT [59], and for allowing us to make them publicly available in KIFIT. F.K. would like to thank Peter Stangl for fruitful discussions during the early stages of this project. We thank our collaborators in the $Yb^+$ [50] and $Ca^+/Ca^{14+}$ [43] King plot analyses for the insightful discussions. E.F., F.K., and J.R. acknowledge funding by the Deutsche Forschungsgemeinschaft (DFG, German Research Foundation) under Germany's Excellence Strategy—EXC-2123 QuantumFrontiers—390837967. A.M. is partially funded by the DFG via the Project No. B10 of the Collaborative Research Cluster 1227 (DQ-mat)—Project-ID 274200144 and also acknowledges support by the EXC-2123 QuantumFrontiers. E.F. was funded by CERN in the initial phase of this work and thanks CERN-TH and the CERN QTI for the stimulating environment. F.K. thanks CERN-TH for its hospitality during the early stages of this project and for support via the CERN-TH visitor program. A.M. thanks the Graduate Academy of Leibniz University Hannover for financial support of an extended research stay at CERN during the early stages of the project and CERN-TH for its hospitality. M.R. is supported by CERN through the CERN Quantum Technology Initiative (QTI). This work has been partially funded by the Deutsche Forschungsgemeinschaft (DFG, German Research Foundation) - 491245950. This collaboration came about thanks to the CERN QTI Forum.

All authors contributed to the writing of the manuscript. A.M., F.K. and J.R. further developed and compared the algebraic King plot methods. F.K. and A.M. conceptualized the overall framework. F.K. developed the initial code. M.R. and F.K. collaborated on the code implementation, while M.R. also carried out the simulations. A.M. compiled and organized the data from the literature and cross-checked results of the code. J.R. performed the atomic structure calculations. E.F. and F.K. supervised and coordinated the project. Following the convention of particle physics, the authors are listed in alphabetical order.

## DATA AVAILABILITY

The data that support the findings of this article are openly available [80].

## APPENDIX A: CALCULATION OF ELECTRONIC COEFFICIENTS IN $Ca^+$

In this section we present some details of the calculation of the electronic new physics coefficients in $Ca^+$.[13] Similar to Ref. [29], we applied the finite field method. In this approach, the new physics potential

$$V_{\mathrm{NP}}(r, m_\phi) = \lambda \frac{1}{4\pi r} e^{-m_\phi r} \tag{A1}$$

is directly added to the Hamiltonian in the Dirac equation, including a dimensionless scaling parameter $\lambda$. Then, the eigenenergies of the considered states are calculated by solving the Dirac equation for different values of the parameter

[13]The $X$ coefficients for Yb used in this paper were calculated in Refs. [47–49] and obtained from J. Berengut via personal communication.

TABLE IV. Transition energies $\Delta E$ and electronic field shift $F_i$, mass shift $K_i$ and new physics coefficients $X_i$ for three transitions in $Ca^+$. Values of $\Delta E$, $F_i$, and $X_i$ were calculated using the CI + MBPT method implemented in AMBIT [59] (see also Appendix A). The latter are reported for two different values of the mediator mass $m_\phi$. The results are in good agreement with the transition energies given in Ref. [108] and the electronic coefficients of Ref. [52]. The values for $K_i$ are taken from Ref. [52]. Values for $\nu_{\rm DSIS}$ can be obtained from the difference of $\nu_{729}$ and $\nu_{732}$. In Ref. [52], the uncertainties on $F_i$ and $K_i$ are estimated to be 5% and 10%, respectively. For $X_i$, we estimate the uncertainty to be about 10%.

| Transition ($i$) | $\Delta E$ [eV] | $F_i$ [eV/fm$^2$] | $K_i$ [eV u] | $X_i(m_\phi = 1\ \text{keV})$ [eV] | $X_i(m_\phi = 10^4\ \text{keV})$ [eV] |
|---|---|---|---|---|---|
| $\nu_{397}$: $3p^6 4s\ ^2S_{1/2} \to 3p^6 4p\ ^2P_{1/2}$ | 3.16 | $-1.19 \times 10^{-6}$ | | 1.11 | $1.29 \times 10^{-4}$ |
| | 3.12 [108] | $-1.18 \times 10^{-6}$ [52] | $-1.59 \times 10^{-3}$ [52] | | |
| $\nu_{732}$: $3p^6 4s\ ^2S_{1/2} \to 3p^6 3d\ ^2D_{3/2}$ | 1.677 | $-1.559 \times 10^{-6}$ | | −2.95 | $1.71 \times 10^{-4}$ |
| | 1.692 [108] | $-1.567 \times 10^{-6}$ [52] | $-1.017 \times 10^{-2}$ [52] | | |
| $\nu_{729}$: $3p^6 4s\ ^2S_{1/2} \to 3p^6 3d\ ^2D_{5/2}$ | 1.685 | $-1.557 \times 10^{-6}$ | | −2.93 | $1.70 \times 10^{-4}$ |
| | 1.700 [108] | $-1.565 \times 10^{-6}$ [52] | $-1.012 \times 10^{-2}$ [52] | | |

$\lambda$. Finally, the $X$ coefficient can be extracted by taking the numerical derivative of the eigenenergies with respect to $\lambda$:

$$X_i = \left.\frac{\partial E_i(\lambda)}{\partial \lambda}\right|_{\lambda=0}. \tag{A2}$$

In a similar manner, the FS coefficients $F_i$ are evaluated by calculating the energies for different nuclear radii and taking the numerical derivative of the eigenenergies with respect to $\delta\langle r^2\rangle$:

$$F_i = \left.\frac{\partial E_i(\lambda)}{\partial \delta\langle r^2\rangle}\right|_{\delta\langle r^2\rangle=0}. \tag{A3}$$

To obtain the eigenenergies, electronic structure calculations are performed using the AMBIT code, which is based on a combination of configuration interaction (CI) and many-body perturbation theory (MBPT) (see, e.g., Refs. [104–107]) and is thoroughly described in Ref. [59]. The specifics of the calculations for $Ca^+$ are overviewed in the Appendixes of Ref. [43].

The results for the $X$ and $F$ coefficients are summarized in Table IV and Fig. 15 and are in good agreement with reference values from Ref. [52].

As discussed in the main text, in the high-mass regime, the ratio of the $X$ coefficients approaches the ratio of field shift coefficients, leading to the loss of sensitivity to new physics. Since even a small discrepancy between the experimental and theoretical values of the field shift ratio $F_j/F_i$ can significantly impact the high-mass behavior of the bounds on new physics, the $X$ coefficients are rescaled so that in the high-mass limit, the ratio $X_j/X_i$ approaches the experimental field shift ratio $F_j^{\rm expt}/F_i^{\rm expt}$, which is obtained from a linear fit to King plot measurements.

Note that the conventions for the new physics coefficients (referred to as $D$ coefficients, e.g., in Refs. [48,49]) vary in the literature. For instance, one can include all prefactors of the Yukawa potential of Eq. (A1) in the calculation of the new physics coefficients. As a result, when utilizing these coefficients to derive constraints on new physics, the obtained bounds are expressed in terms of $y_e y_n$. However, in other conventions a factor of $1/(4\pi\alpha_{\rm EM})$ is factored out from the $X$ coefficient, resulting in bounds being expressed in terms of $y_e y_n/(4\pi\alpha_{\rm EM}) = \frac{\alpha_{\rm NP}}{\alpha_{\rm EM}}$. In this work, the $X$ coefficients are always presented in the latter convention.

## APPENDIX B: SENSITIVITY TO NEW PHYSICS

To gain an understanding of how the choice of transitions can affect the bounds on the new physics coupling, we compare bounds obtained by applying Eqs. (10) and (13) to subsets of isotope shift measurements in $Ca^+$. We fix $\nu_{729}$: $3p^6 4s^2 S_{1/2} \to 3p^6 3d\ ^2D_{5/2}$ as the reference transition $\nu_1$ and combine it with either of the transitions

(1) $\nu_{397}$: $3p^6 4s\ ^2S_{1/2} \to 3p^6 4p\ ^2P_{1/2}$,
(2) $\nu_{732}$: $3p^6 4s\ ^2S_{1/2} \to 3p^6 3d\ ^2D_{3/2}$,
(3) $\nu_{\rm DD}$: $3p^6 3d\ ^2D_{3/2} \to 3p^6 3d\ ^2D_{5/2}$,

where the subscripts correspond to the transition wavelength in nm, while DD is associated with fine-structure splitting. A comprehensive list of available isotope shift data in Ca can be found in Table IX.

### 1. Identifying King plot candidates

The shape of $V_{\rm pred}$ can hint at the best transitions for new physics searches: a combination of electronic coefficients

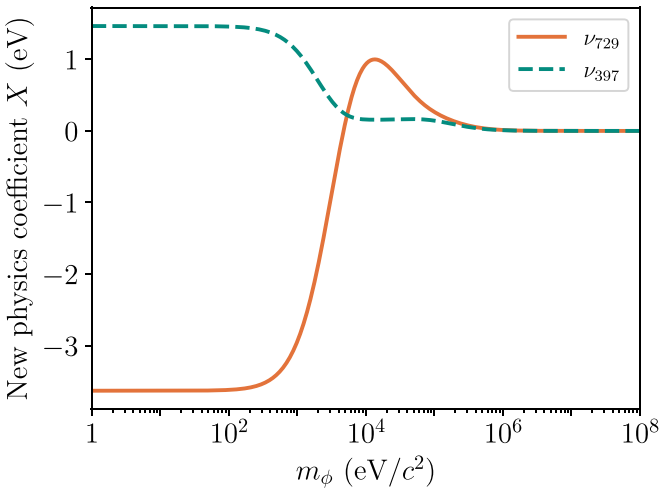


FIG. 15. Dependence of the electronic new physics coefficients of the $\nu_{729}$ and $\nu_{397}$ transitions in $Ca^+$ on the mediator mass $m_\phi$. The coefficient of the $\nu_{732}$ transition is nearly identical to that of $\nu_{729}$ and is therefore not displayed in the figure.

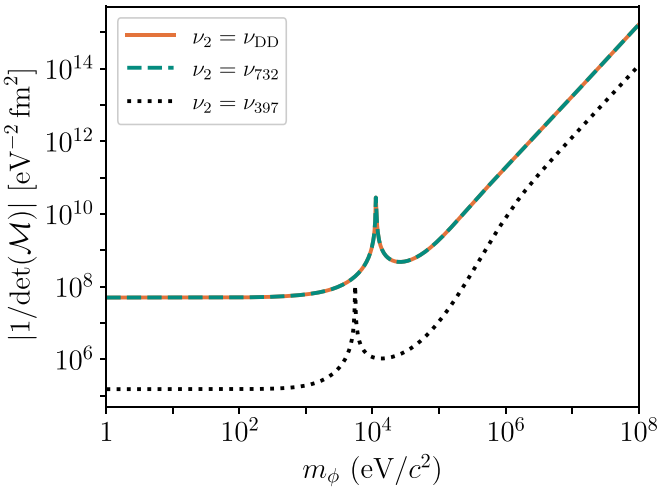


FIG. 16. Sensitivity of different transition pairs to new physics. The reference transition is fixed to $\nu_1 = \nu_{729}$, the second transitions are as specified in the legend. The inverse of the electronic dependence of $V_{\rm pred}$ [see Eq. (12)] as a function of the mass $m_\phi$ of the new boson, suggesting the combination ($\nu_{729}$, $\nu_{397}$) is more sensitive than the other two, which are equally sensitive.

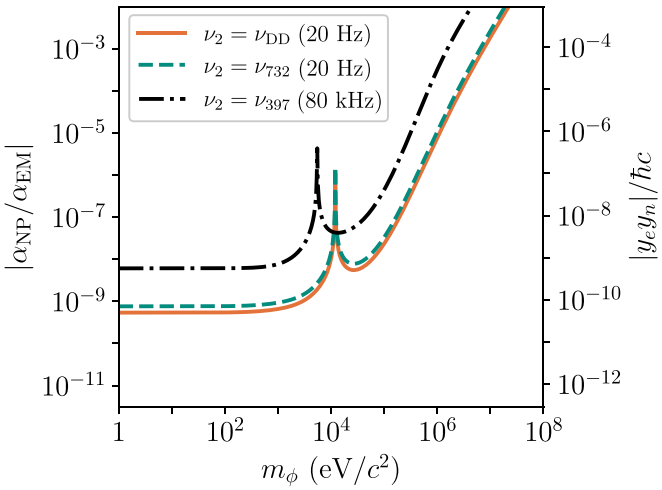


FIG. 17. Predicted $2\sigma$ upper bounds on $|\alpha_{\rm NP}/\alpha_{\rm EM}|$ for linear mock data with uncertainties as reported in the legend. Although the combination involving $\nu_{397}$ appears to be the most promising based on the behavior of $|1/\det(\mathcal{M})|$, the bounds on $|\alpha_{\rm NP}/\alpha_{\rm EM}|$ obtained for the other two combinations turn out to be more stringent due to smaller experimental uncertainties. $\nu_{\rm DD}$ wins against $\nu_{732}$ thanks to the smaller isotope shift.

that maximizes this volume suggests a high sensitivity of the associated transitions to $\alpha_{\rm NP}$. In Table IV we report our calculations of the electronic coefficients of the transitions listed above and in Fig. 16 we plot the inverse of the electronic dependence of $V_{\rm pred}$:

$$\frac{1}{V_{\rm pred}} \propto \frac{1}{\det\left(\mathcal{M}(m_\phi)\right)} = \frac{1}{F_1X_2(m_\phi) - F_2X_1(m_\phi)}, \tag{B1}$$

which determines the $m_\phi$-dependence of the bounds on $\alpha_{\rm NP}$ [see Eqs. (10) and (12)]. The $m_\phi$-independent low-mass behavior, as well as the loss of sensitivity at high mediator masses $m_\phi$, are clearly visible. Moreover, we observe peaks, which are the consequence of accidental cancellations of $\det\left(\mathcal{M}(m_\phi)\right)$ at specific values of $m_\phi$.

We identify the combination of $\nu_{729}$ and $\nu_{397}$ as the pair of transitions with the largest value for $\det\left(\mathcal{M}(m_\phi)\right)$, suggesting a high sensitivity to new physics. This can be understood as a consequence of the complementarity of the electronic levels involved in these transitions. In contrast, the combinations of $\nu_{729}$ with $\nu_{732}$ or $\nu_{\rm DD}$ yield a smaller value for the electronic part of $V_{\rm pred}$. Indeed, the similarity of the $D_{3/2}$ and $D_{5/2}$ states results in similar electronic coefficients leading to a higher degree of cancellation in $F_1X_2(m_\phi) - F_2X_1(m_\phi)$.

### 2. The perfectly linear King plot

Next, we consider the idealized case of a perfectly linear King plot ($V_{\rm dat} = 0$). To this end, we generate perfectly linear mock values for the isotope shifts, i.e., we use Eq. (1) to calculate linear isotope shift data based on experimental values for the nuclear radii [25] and masses [65], as well as on theory calculations of the SM electronic coefficients (reported in Table IV).

Clearly, in this case $\langle\alpha_{\rm NP}\rangle = 0$ and the bounds are fully determined by $\sigma[\alpha_{\rm NP}]$. We can gain some insight into the behavior of $\sigma[\alpha_{\rm NP}]$ by performing linear error propagation on Eq. (10):

$$\sigma[\alpha_{\rm NP}] = \sqrt{\left(\frac{\sigma[V_{\rm dat}]}{V_{\rm pred}}\right)^2 + \left(\frac{V_{\rm dat}}{V_{\rm pred}^2}\sigma[V_{\rm pred}]\right)^2}. \tag{B2}$$

with $V_{\rm dat}$ and $V_{\rm pred}$ as defined in Eq. (10). In linear King plots, only the first term is relevant and $\sigma[\alpha_{\rm NP}]$ is dominated by experimental uncertainties. What determines the sensitivity to new physics is thus the interplay of $V_{\rm pred}$ and $\sigma[V_{\rm dat}]$. Since the latter includes terms of the form $\tilde{v}_i^a\sigma[\tilde{v}_j^b]$, more constraining bounds can be expected from comparatively small but precisely measured isotope shifts. We assign realistic uncertainties to our mock transitions (20 Hz for $\nu_{729}$, $\nu_{\rm DD}$ and $\nu_{732}$ [41], 80 kHz for $\nu_{397}$ [26]) and compare the projections for the $2\sigma$ upper bounds in Fig. 17. Here, we limit the analysis to $|\frac{\alpha_{\rm NP}}{\alpha_{\rm EM}}|$ for simplicity. Although the combination involving $\nu_{397}$ appeared to be the most promising based on the behavior of its electronic coefficients, the higher experimental uncertainty limits its sensitivity to new physics, relative to the other combinations.

### 3. The linear King plot

Having identified the combination of the $\nu_{729}$ and $\nu_{\rm DD}$ transitions to generate the most stringent bounds to new physics, we use real data from Refs. [40,41,109], which produce a linear King plot within the experimental uncertainties ($\sigma[V_{\rm dat}]/V_{\rm dat} \lesssim 1$). In Fig. 18, we compare the resulting bounds with those from perfectly linear mock data.

Since real data predict a nonzero central value for the new physics coupling, the bounds are shifted away from zero. This effect is most pronounced in the low-mass limit, where the King plot method is most sensitive to new physics. Moreover, the second term in Eq. (B2) is now nonzero. This has a noticeable impact if the uncertainties on the

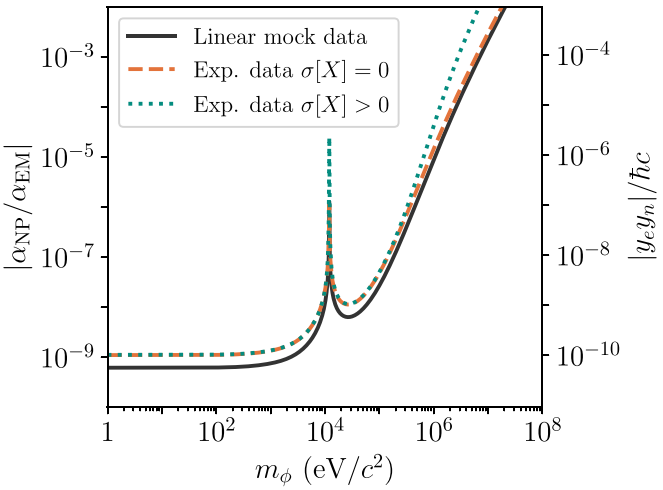


FIG. 18. The bounds from the combination of $\nu_{\rm DD}$ and $\nu_{729}$. The black curve shows the results for perfectly linear mock data while the orange dashed and teal dotted curves represent bounds derived from the experimental data reported in Refs. [40,41], with and without including uncertainties on the electronic new physics coefficient $X_i$.

electronic new physics coefficients $X$, which we take to be 10% of their computed value (see Appendix A), are introduced: Since this term scales with $1/\mathrm{V}_{\rm pred}^2$ and $\mathrm{V}_{\rm pred}$ becomes small for large values of $m_\phi$, uncertainties on the $X$ coefficients lead to a loss of sensitivity in the high-mass region. This highlights the importance of considering the uncertainty of $X$ and suggests that more precise $X$ coefficient calculations could improve the bounds, particularly in the high-mass range.

## APPENDIX C: PROJECTION OF UNCERTAINTIES

To better understand how the uncertainties on the measured isotope shifts and atomic masses propagate to the bounds on the new physics coupling, we can project the experimental uncertainties onto the directions parallel and perpendicular to the King line and evaluate their impact on the uncertainty on $\alpha_{\rm NP}$:

$$\Sigma_{\parallel}^{\alpha} = (\nabla_{\tilde{\nu}}\alpha_{\rm NP})^{\top}\boldsymbol{P}_{\parallel}\boldsymbol{\Sigma}_{\tilde{\nu}}\boldsymbol{P}_{\parallel}\nabla_{\tilde{\nu}}\alpha_{\rm NP} \equiv \left(\sigma[\alpha_{\rm NP}]^{(1)}_{\rm KP,\parallel}\right)^2,$$

$$\Sigma_{\perp}^{\alpha} = (\nabla_{\tilde{\nu}}\alpha_{\rm NP})^{\top}\boldsymbol{P}_{\perp}\boldsymbol{\Sigma}_{\tilde{\nu}}\boldsymbol{P}_{\perp}\nabla_{\tilde{\nu}}\alpha_{\rm NP} \equiv \left(\sigma[\alpha_{\rm NP}]^{(1)}_{\rm KP,\perp}\right)^2,$$

$$\Sigma_{\parallel\perp}^{\alpha} = (\nabla_{\tilde{\nu}}\alpha_{\rm NP})^{\top}\boldsymbol{P}_{\parallel}\boldsymbol{\Sigma}_{\tilde{\nu}}\boldsymbol{P}_{\perp}\nabla_{\tilde{\nu}}\alpha_{\rm NP} = (\Sigma_{\perp\parallel}^{\alpha})^{\top}. \tag{C1}$$

Here the superscript (1) indicates that we are applying linear error propagation, whereas

$$\nabla_{\tilde{\nu}}\alpha_{\rm NP} = \begin{pmatrix} \frac{\partial\alpha_{\rm NP}}{\partial\tilde{\nu}_1^1} & \cdots & \frac{\partial\alpha_{\rm NP}}{\partial\tilde{\nu}_m^1} \\ \vdots & \ddots & \vdots \\ \frac{\partial\alpha_{\rm NP}}{\partial\tilde{\nu}_1^n} & \cdots & \frac{\partial\alpha_{\rm NP}}{\partial\tilde{\nu}_m^n} \end{pmatrix} \tag{C2}$$

corresponds to the gradient of $\alpha_{\rm NP}$ with respect to the $n \times m$ mass-normalized isotope shifts $\{\tilde{\nu}_i^a\}_{1\leqslant i\leqslant m}^{1\leqslant a\leqslant n}$ (points in the King plot), and

$$\boldsymbol{\Sigma}_{\tilde{\nu}} = \begin{pmatrix} \Sigma_{\tilde{\nu}}^{11} & \cdots & \Sigma_{\tilde{\nu}}^{1n} \\ \vdots & \ddots & \vdots \\ \Sigma_{\tilde{\nu}}^{n1} & \cdots & \Sigma_{\tilde{\nu}}^{nn} \end{pmatrix} \tag{C3}$$

denotes the $(m \times m \times n \times n)$-dimensional covariance matrix of the set of $n$ mass-normalized isotope shift vectors $\{\tilde{\boldsymbol{\nu}}^a\}_{a=1}^n$. The entries of $\boldsymbol{\Sigma}_{\tilde{\nu}}$ are $(m \times m)$-dimensional covariance matrices associated with $\tilde{\boldsymbol{\nu}}^a = (\tilde{\nu}_1^a, \ldots, \tilde{\nu}_m^a)$ and $\tilde{\boldsymbol{\nu}}^b = (\tilde{\nu}_1^b, \ldots, \tilde{\nu}_m^b)$:

$$\Sigma_{\tilde{\nu}}^{ab} = \begin{pmatrix} \mathrm{Cov}(\tilde{\nu}_1^a, \tilde{\nu}_1^b) & \cdots & \mathrm{Cov}(\tilde{\nu}_1^a, \tilde{\nu}_m^b) \\ \vdots & \ddots & \vdots \\ \mathrm{Cov}(\tilde{\nu}_1^a, \tilde{\nu}_m^b) & \cdots & \mathrm{Cov}(\tilde{\nu}_m^a, \tilde{\nu}_m^b) \end{pmatrix}, \tag{C4}$$

where

$$\mathrm{Cov}(\tilde{\nu}_i^a, \tilde{\nu}_j^b) = \sum_{k=1}^{m}\sum_{c=1}^{n}\left(\frac{\partial\tilde{\nu}_i^a}{\partial\nu_k^c}\sigma[\nu_k^c]^2\frac{\partial\tilde{\nu}_j^b}{\partial\nu_k^c} + \frac{\partial\tilde{\nu}_i^a}{\partial m^c}\sigma[m^c]^2\frac{\partial\tilde{\nu}_j^b}{\partial m^c} + \frac{\partial\tilde{\nu}_i^a}{\partial m^{c'}}\sigma[m^{c'}]^2\frac{\partial\tilde{\nu}_j^b}{\partial m^{c'}}\right), \tag{C5}$$

assuming the isotope shift and mass measurements are independent. The objects $\boldsymbol{P}_{\parallel}$ and $\boldsymbol{P}_{\perp}$ in Eq. (C1) are $(n \times n \times m \times m)$-dimensional projectors onto the parallel and perpendicular directions,

$$\boldsymbol{P}_{\parallel} = \mathbb{1}_n \otimes P_{\parallel} = \mathrm{diag}(P_{\parallel}, \ldots, P_{\parallel})_n \tag{C6}$$

$$\boldsymbol{P}_{\perp} = \mathbb{1}_n \otimes P_{\perp} = \mathrm{diag}(P_{\perp}, \ldots, P_{\perp})_n. \tag{C7}$$

Here $\otimes$ denotes the tensor product and $P_{\parallel}$ and $P_{\perp}$ are the $(m \times m)$-dimensional projectors

$$P_{\parallel} = \hat{\boldsymbol{e}}_{\boldsymbol{\mathcal{F}}}\hat{\boldsymbol{e}}_{\boldsymbol{\mathcal{F}}}^{\top}, \quad P_{\perp} = \mathbb{1}_m - \hat{\boldsymbol{e}}_{\boldsymbol{\mathcal{F}}}\hat{\boldsymbol{e}}_{\boldsymbol{\mathcal{F}}}^{\top}, \tag{C8}$$

$$P_{\parallel}^2 = P_{\parallel}, \quad P_{\parallel}^{\top} = P_{\parallel}, \quad P_{\perp}^2 = P_{\perp}, \quad P_{\perp}^{\top} = P_{\perp}, \tag{C9}$$

where $\hat{\boldsymbol{e}}_{\boldsymbol{\mathcal{F}}}$ is the unit vector along the King line [see Eq. (38)] and $\mathbb{1}_m$ is the $(m \times m)$-dimensional identity matrix.

Finally, the impact of the uncertainties perpendicular to the King line on the estimation of $\sigma[\alpha_{\rm NP}]$ can be evaluated by computing

$$\sqrt{\frac{\Sigma_{\perp}^{\alpha}}{\Sigma^{\alpha}}} \equiv \frac{\sigma[\alpha_{\rm NP}]^{(1)}_{\rm KP,\perp}}{\sigma[\alpha_{\rm NP}]^{(1)}_{\rm KP}}, \tag{C10}$$

where $\sigma[\alpha_{\rm NP}]^{(1)}_{\rm KP}$ is the full uncertainty without projectors:

$$\sigma[\alpha_{\rm NP}]^{(1)}_{\rm KP} \equiv \sqrt{\Sigma_{\alpha}} \equiv \sqrt{(\nabla_{\tilde{\nu}}\alpha_{\rm NP})^{\top}\boldsymbol{\Sigma}_{\tilde{\nu}}\nabla_{\tilde{\nu}}\alpha_{\rm NP}}. \tag{C11}$$

For all elements in Table III we checked that $\sigma[\alpha_{\rm NP}]^{(1)}_{\rm KP,\perp}/\sigma[\alpha_{\rm NP}]^{(1)}_{\rm KP} \approx 1$ within numerical uncertainties.

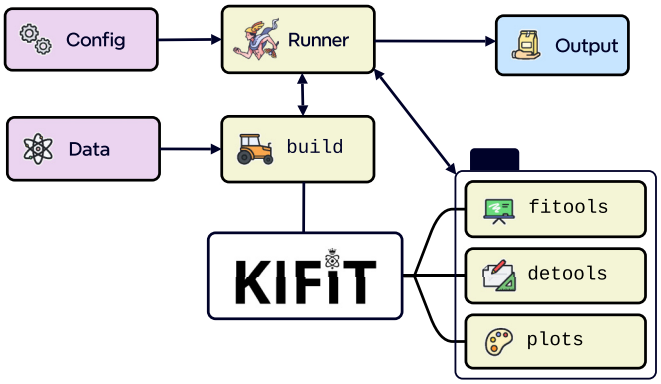


FIG. 19. Schematic structure of KIFIT 0.1.0.

## APPENDIX D: THE KIFIT PACKAGE

KIFIT is a prototype code and is published strictly for reasons of transparency and reproducibility. In this section, we briefly explain the structure of the package and give an introductory example of how to use KIFIT. We also summarize the pytests implemented in the code.

### 1. Structure of the KIFIT package

The source code of KIFIT can be divided into three main modules: build, tools, and run, which are represented with yellow boxes in the diagram of Fig. 19.

The operative module is run, where a Runner class makes use of build and tools to process data and perform either the algebraic methods and the King plot fit.

To launch the KIFIT scripts, a kifit_data folder is required, in which experimental data have to be provided in the same format as in the example which can be found in the code repository and as described below. The execution of the code can be customized by defining a set of initial parameters in an appropriate configuration file (see README.md file of our repository for more detailed information).

The module build constructs one instance of the class kifit.Elem for each experimental dataset collected in a kifit.ElemCollection. The module tools contains two sets of functions which compute the bounds on $\alpha_{\rm NP}$, either using the fit (fitools) or the algebraic methods (detools). Finally, the script plot is a compilation of plot scripts that can be used to visualize the fit and determinant results.

### 2. How to use KIFIT

#### *a. Data preparation*

First, the input data need to be organized in subfolders of the kifit_data subfolder and with names corresponding to the element identification (e.g., elem):

```
kifit/
|-- src/
|   |- kifit/
|   |   |- ...
|   |   |- user_elements.py
|   |- kifit_data/
|   |   |- elem/
|   |   |   |- binding_energies_elem.dat
|   |   |   |- isotopes_elem.dat
|   |   |   |- nu_elem.dat
|   |   |   |- sig_nu_elem.dat
|   |   |   |- sig_Xcoeffs_elem.dat
|   |   |   |- Xcoeffs_elem.dat
|   |- tests/
```

The KIFIT datafiles inside the elem subfolder are to be named as follows:

```
type_elem_ISinstitutions_massinstitution_year
.dat
```

where type refers to the type of data saved in the file (for example data files, see the code repository):

(1) binding_energies: electron binding energies, extracted from NIST [110]

(2) isotopes: isotope numbers $A, A'$, masses $(m^A, m^{A'})$, mass uncertainties $(\sigma[m^A], \sigma[m^{A'}])$.

(3) nu: isotope shift measurements $(\nu_i^a)$; (columns: transitions, rows: isotope pairs).

(4) sig_nu: uncertainties on the isotope shift measurements $(\sigma[\nu_i^a])$.

(5) Xcoeffs and sig_Xcoeffs: electronic coefficients $(X_i)$ and their uncertainties $(\sigma[X_i])$ for the transitions listed in nu datafiles, for different values of the new boson masses $m_\phi$ (each line corresponding to a separate value of $m_\phi$). In the current version of KIFIT, the sig_Xcoeffs files are not employed.

ISinstitutions and massinstitution list the institutions where the isotope shift measurements contained in nu and the isotope masses measurements contained in isotopes datafiles were respectively carried out, while year reports the year of the most recent isotope shift measurements collected in the folder. If no massinstitution is specified, isotope masses measurement are taken from either AME2020 [111] or AME2016 [65], as reported in the heading of the isotopes datafiles. Similarly, the heading of ISinstitutions datafiles reports, in shorthand notation, the publications from which we extracted the isotope shift measurements, as well as for the electronic transition. Table V provides a list of the data folders available within KIFIT, the shorthand notation adopted to refer to the institutions and the "dimension" of the dataset, i.e., number of transitions ($m$) and isotope pairs ($n$).

In order for the element elem to become a "valid" KIFIT element, its identification (e.g.,elem) needs to be added to the list of elements collected in kifit/src/user_elements.py.

TABLE V. KIFIT data folders with the corresponding references (2nd and 3rd columns) and dimensions (number of transitions $m$ and isotope pairs $n$, 4th column). The datafiles marked with an asterisk use artificially modified uncertainties for the isotope shifts and were used as test datafiles. The mock data for `Ca10pointsTEST` was generated using Eq. (1), the electronic coefficients from Table IV and the nuclear masses and charge radii from Refs. [25,65], plus small artificial King nonlinearities.

| KIFIT folder | Isotope shifts | Masses | $n \times m$ |
|---|---|---|---|
| `Ca_PTB_2015` | Gebert2015 [26] | [111] | $3 \times 2$ |
| `Ca_WT_Aarhus_2020` | Knollmann2019[40]+Solaro2020 [41] | [111] | $4 \times 2$ |
| `Ca_WT_Aarhus_2024` | Solaro2020 [41], Knollmann2023 [109], Chang2024 [42] | [111] | $4 \times 2$ |
| `Ca_WT_Aarhus_PTB_2020` | Knollmann2019 [40], Solaro2020 [41], Gebert2015 [26] | [111] | $3 \times 4$ |
| `Ca_WT_Aarhus_PTB_2024` | Knollmann2023 [109], Chang2024 [42], Gebert2015 [26] | [111] | $3 \times 4$ |
| `Ca24min` | Knollmann2023 [109], Chang2024 [42] | [65] | $3 \times 2$ |
| `Camin` | Knollmann2019 [40], Solaro2020 [41] | [65] | $3 \times 2$ |
| `Ca_testdata` | Knollmann2019 [40], Solaro2020 [41], Gebert2015 [26] | [65] | $3 \times 4$ |
| `Ca3pointsTEST` | * Knollmann2023 [109], Chang2024 [42] | [65] | $3 \times 2$ |
| `Ca4pointsTEST` | * Knollmann2023 [109], Chang2024 [42] | [65] | $4 \times 2$ |
| `Ca10pointsTEST` | Mock data | [65] | $10 \times 2$ |
| `Yb_Kyoto_MIT_GSI_2022` | Ono2022 [71], Counts2020 [48], Hur2022 [49], Figueroa2022 [47] | [65] | $4 \times 5$ |
| `Yb_Kyoto_MIT_GSI_PTB_2024` | Ono2022 [71], Door2024 [50], Counts2020 [48], Figueroa2022 [47] | [65] | $4 \times 5$ |
| `Yb_Kyoto_MIT_GSI_PTB_MPIK_2024` | Ono2022 [71], Door2024 [50], Counts2020 [48], Figueroa2022 [47] | [50] | $4 \times 5$ |
| `Yb_PTB_MPIK_2024` | Door2024 [50] | [50] | $4 \times 2$ |

#### *b. Setting up the simulation parameters*

The KIFIT run can be customised through various hyperparameters. These can be parsed by KIFIT directly via the command line, or provided in the form of a JSON file. An example KIFIT configuration could be the following:

```
#                  config.json
{
    # Here we list the elements whose data is to
     be combined:
    "element_list": ["elem", "extra_elem"],
    # When more than one element is listed above
    , use globalogrid:
    "search_mode": "globalogrid",
    # Experiments and block sizes for blocking
    "num_exp": 100,
    "block_size": 20,
    # Sampled points in the MC
    "num_alphasamples_search": 500,
    "num_elemsamples_per_alphasample_search":
    500,
    "num_elemsamples_exp": 500,
    "num_alphasamples_exp": 500,
    "min_percentile": 2,
    # The target mass indices
    "x0_fit": [0],
    "x0_det": [0],
    "gkp_dims": [3],
    # Algebraic methods' params
    "nmgkp_dims": [3],
    "proj_dims": [3],
    "num_det_samples": 5000,
    "num_sigmas": 2,
}
```

More parameters can be added to the configuration file, and we recommend referring to the official documentation for a more detailed explanation.

#### *c. Running the algorithm*

Once the input files are organized and the KIFIT configuration is defined, we can write a `python` script to compute the estimation of the new physics bounds. As shown in Fig. 19, we use a *Runner* object (`Runner.config`) to share information among the KIFIT tools.

```
from kifit.run import Runner
from kifit.config import RunParams

# Set the kifit parameters given in the
    configuration file
# (Leave the arguments empty if parsing from
    command line)
params = RunParams(configuration_file="config.
    json")

# initialize the runner
runner = Runner(params)

# Run
runner.run()

# If needed, generate plots
runner.generate_all_alphaNP_ll_plots()
```

#### *d. Collecting results*

The output of KIFIT is stored in the `kifit/results` folder, which can contain two subfolders: `output_data`, containing the numerical results in the form of JSON files, and `plots`, containing the final plots plus the real-time plots, if requested by the user. Once a KIFIT run is completed and the numerical results are collected, the user can exploit the same configuration file as above to process data and generate more plots, using the functions provided in `plot.py`. [Simply replace `runner.run()` with a command such as `runner.generate_all_alphaNP_ll_plots()`.]

### 3. Validation of the algorithm

We performed a series of validation simulations to highlight the robustness to the procedure sketched above, and to gain a better understanding of the optimal hyperparameters required to run a KIFIT experiment. Table VI lists the benchmark values, while the bar plots in Fig. 20 illustrate the

TABLE VI. Default values of the KIFIT hyperparameters set in our validation test. In Fig. 20 these values are varied one by one to investigate their impact on the KIFIT estimation.

| Hyperparameter | Value |
|---|---|
| num_elemsaples_per_alphasample_search | 500 |
| num_exp | 200 |
| block_size | 20 |
| min_percentile | 5 |
| num_alphasamples_exp | 500 |
| num_elemsamples_exp | 500 |

stability of the code as we vary one of the hyperparameters after the other.

The sensitivity of the code to the choice of the reference transition was investigated explicitly. Although the reference transition seems to play a special role in the construction of the King plot fit [see e.g., Eqs. (37), (41) or Fig. 4], the relations between the reference transition and the other transitions are symmetric and

$$\left|d^a_{ji}\right| = \left|d^a_{ij}\right|, \tag{D1}$$

where we denoted $d^a_j \equiv d^a_{ji}$ [see Eq. (48)], i.e., we explicitly mentioned the reference transition $i$.

This property is particularly easy to observe in the two-dimensional case:

$$\begin{aligned}\left|d^a_{21}\right| &= \left|\delta^a_{21}\cos\phi_{21}\right| \\ &= \left|\frac{\alpha_{\rm NP}}{\alpha_{\rm EM}}(X_2 - \tan\phi_{21}X_1)(\tilde{\gamma}^a - \langle\tilde{\gamma}\rangle^2)\cos\phi_{21}\right| \\ &\overset{(*)}{=} \left|\frac{\alpha_{\rm NP}}{\alpha_{\rm EM}}(\tan\phi_{12}X_2 - X_1)(\tilde{\gamma}^a - \langle\tilde{\gamma}\rangle^1)\cos\phi_{12}\right| \\ &= \left|\delta^a_{12}\cos\phi_{12}\right| = \left|d^a_{12}\right|,\end{aligned} \tag{D2}$$

where in $(*)$ we assumed that $\langle\tilde{\gamma}\rangle^2 = \langle\tilde{\gamma}\rangle^1$, which is the case if we employ the definition given in Eq. (47).

The symmetry of the log-likelihood construction can be observed in Fig. 21, which shows the outputs of one of the our numerical tests of KIFIT (can be found in the kifit/src/tests folder). Both were produced using the same input data (central values and uncertainties of the mass and frequency measurements) and $\alpha_{\rm NP}$ samples, but the upper plot in Fig. 21 shows the $\Delta\chi^2$ values computed using the manifestly symmetric version of $\sigma[\delta^a_{i1}]$ [Eq. (47)], while the

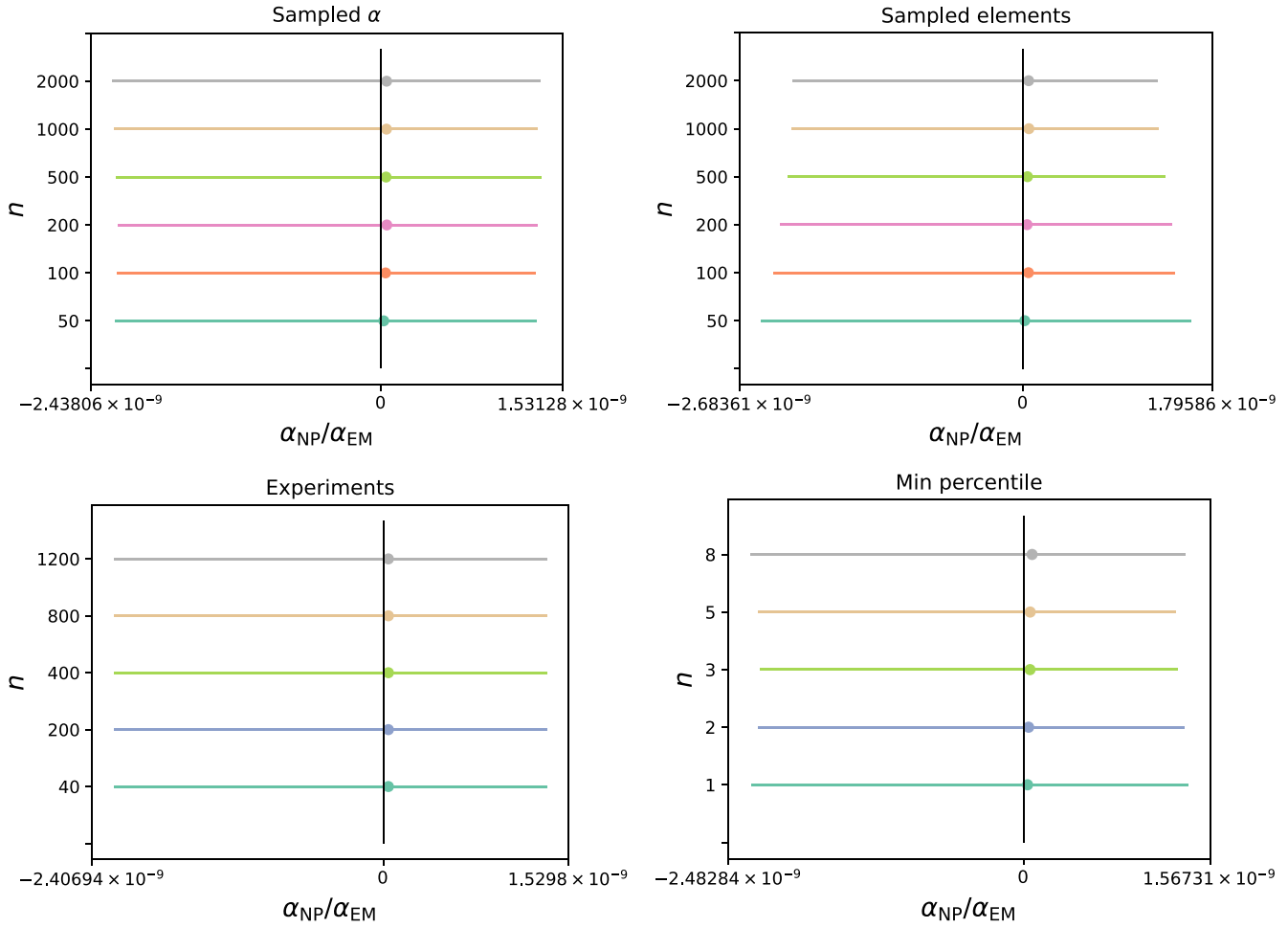


FIG. 20. Estimated $\alpha_{\rm NP}/\alpha_{\rm EM}$ values (central dots) and bounds (bars) obtained executing KIFIT. The subplots show the impact of varying one of the relevant hyperparameters at a time.

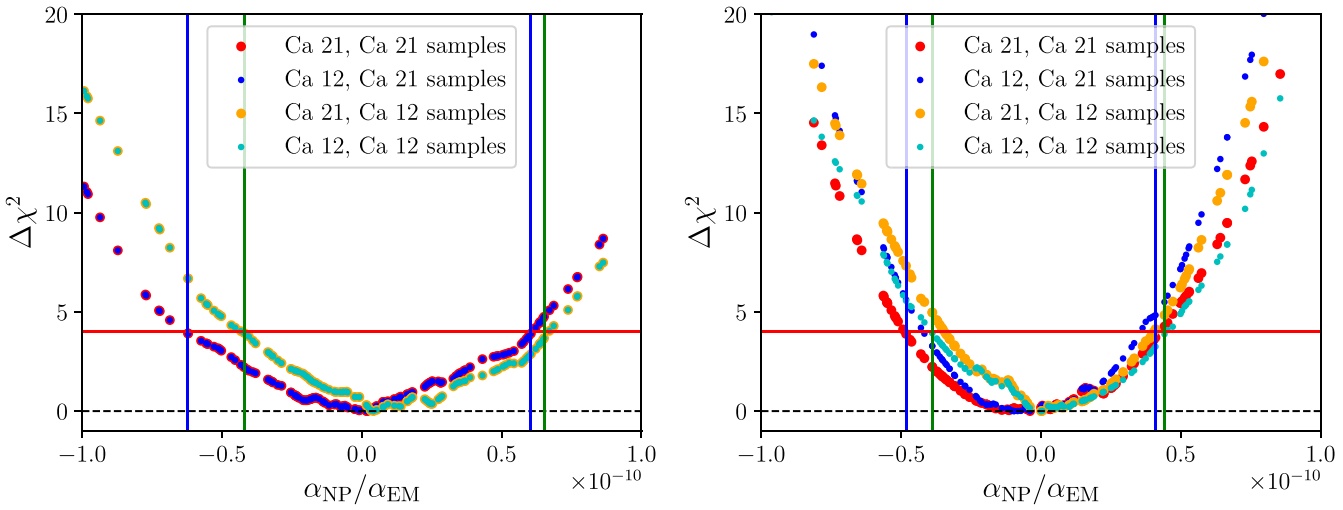


FIG. 21. Test of the symmetry of the KIFIT code with respect to exchanges of the transitions. `Ca12` and `Ca21` correspond to two test datasets that differ only in the order of the transitions, and consequently in which of the two transitions is used as a reference transition (in `Caij`, $i, j \in \{1, 2\}$, $i$ is considered to be the reference transition). `Caij samples` denote the input parameter and fit parameter samples obtained for the dataset `Caij`. Based on these samples, the $\Delta\chi^2$ values are computed for each $\alpha_{\rm NP}$ sample, once using the `kifit.Elem` setup provided by the element `Caij` and once by adapting the samples to the conventions of the "dual" element `Caji` and using the setup provided by `Caji`. The left (right) figure shows the $(\alpha_{\rm NP}/\alpha_{\rm EM}, \Delta\chi^2)$ values obtained adopting the symmetric (asymmetric) definition of $\langle\tilde{\gamma}\rangle$ [Eq. (47) vs Eq. (44)].

definition given in Eq. (44) was used in the making of the lower plot in Fig. 21. The different colors represent different sets of samples of the input parameters [transition frequencies and masses, see Eq. (14)] and fit parameters $K_{21}^{\perp}$ and $\phi_{21}$ [see Eq. (55)]: The label "Ca $ji$, Ca $lk$ samples" means that the element Ca with the set of transitions $k, l$, where $k$ is the reference transition, was used to generate samples of the input parameters and fit parameters, and that the $\Delta\chi^2$ function associated with the element Ca $ji$, where $i$ is the reference transition, was evaluated. As can be seen in Fig. 21, the manifestly symmetric version of $\langle\tilde{\gamma}\rangle$ given in Eq. (47) leads to a $\Delta\chi^2$ that is invariant under the exchange of transitions $(12 \to 21)$. The $\Delta\chi^2$ values vary slightly between different sets of samples (Ca 21 samples vs Ca 12 samples), but this is precisely the spread which is captured in the *experiment phase* (Sec. III C) and by the *blocking method* described in Sec III D. This spread is present between all four sets of results when using the definition for $\langle\tilde{\gamma}\rangle$ given in Eq. (44) (Fig. 21).

A number of complementary tests were directly implemented as `pytests` in the KIFIT code. A nonexhaustive list of the tests is given in the following. For details, please directly check the `kifit/src/tests` folder.

#### *a.* `test_build`

(1) Loading elements, checking dimensions of input data.
(2) Comparison of results of ODR and linear regression in linear fit to King plot data.
(3) Numerical cross-checks of KIFIT construction against results obtained with *Mathematica*.
(4) Numerical cross-checks of implementation of algebraic methods in KIFIT against results obtained with *Mathematica*.

#### *b.* `test_detools`

(1) Numerical cross-checks of uncertainties computed for algebraic methods in KIFIT against results obtained with *Mathematica*.
(2) Plot distribution of $\alpha_{\rm NP}$ values.

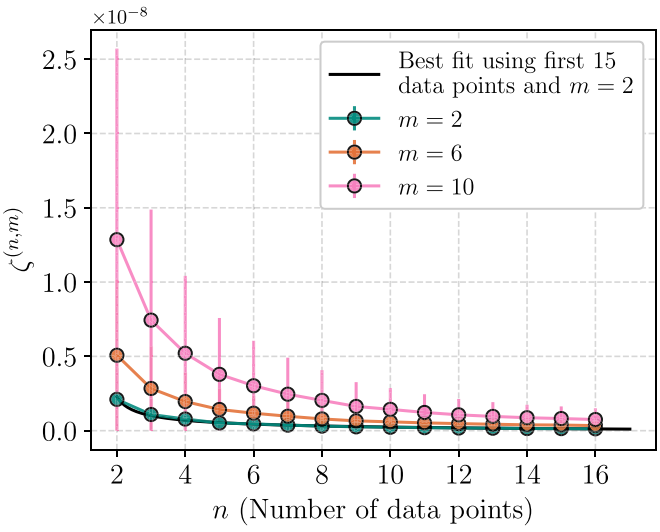


FIG. 22. Illustration of the goodness a fit to $y_j = b_j x + c_j$, $j = 1, \ldots, m$ as a function of the number $n$ of mock data points $(x, y_1, \ldots, y_m)$. $\zeta^{(n)} \equiv \langle\zeta^{(n,s)}\rangle_{(s)}$ with $\zeta^{(n,s)}$ as defined in Eq. (E3) corresponds to the average relative uncertainty on the $2(n-1)$ fit parameters $\{b_j, c_j\}_{j=2}^{m}$ used to fix the line in $m$-dimensional space. We show the results for the minimal case of $m = 2$ and for $m = 6$. For each number $n$ of data points, 500 mock datasets with Gaussian uncertainties $\sigma = \sigma_n = 10^{-10}$ were generated, leading to relative uncertainties $\sigma_x/x$, $\sigma_y/y$ of the same order. In black we show the curve defined by $f(n) = \theta_1/\sqrt{n-\theta_2} + \theta_3$, with $(\theta_1, \theta_2, \theta_3) \approx (1.5 \times 10^{-9}, 1.7, -3 \times 10^{-10})$.

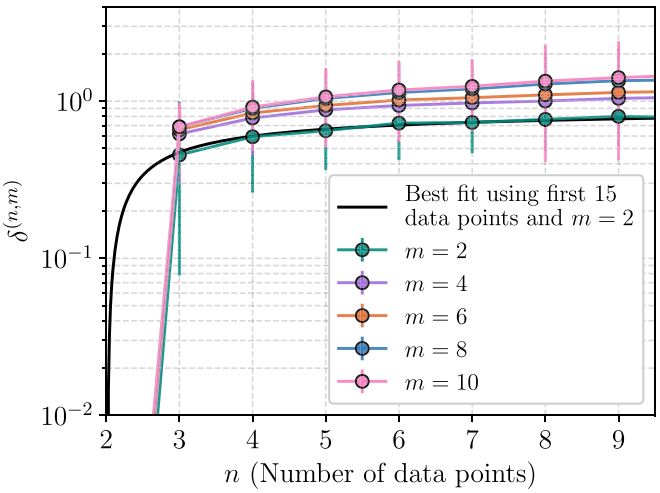


FIG. 23. $\delta^{(n,m)}$ [see Eq. (E6)] as a function of the number $n$ of the mock data points. In black we show the curve defined by $f(n) = \theta_1/\sqrt{n-\theta_2}+\theta_3$, with $(\theta_1,\theta_2,\theta_3) \approx (-0.6, 1.6, 1)$. $\delta^{(n,m)}$ can be interpreted as the average distance of a point $a$ in an $n$-dimensional dataset to the corresponding best-fit line.

#### *c.* `test_fitools`

(1) Numerical cross-checks of `KIFIT` construction for single point (sample) in parameter space against results obtained with *Mathematica*. The procedure is repeated for different values of the fit parameters $\{K_{j1}^{\perp}, \phi_{j1}\}_{j=2}^{m}$, for $\frac{\alpha_{\rm NP}}{\alpha_{\rm EM}} = 0$ and for $\frac{\alpha_{\rm NP}}{\alpha_{\rm EM}} = 10^{-11}$.

(2) Cross-check of $\|\boldsymbol{d}\|$, the covariance matrix $\boldsymbol{\Sigma_d}$, the log-likelihood and various intermediate steps against results obtained with *Mathematica*. The procedure is repeated for different values of the fit parameters $\{K_{j1}^{\perp}, \phi_{j1}\}_{j=2}^{m}$, with and without sampling of the fit parameters, for different values of $\alpha_{\rm NP}$ and for different sample numbers.

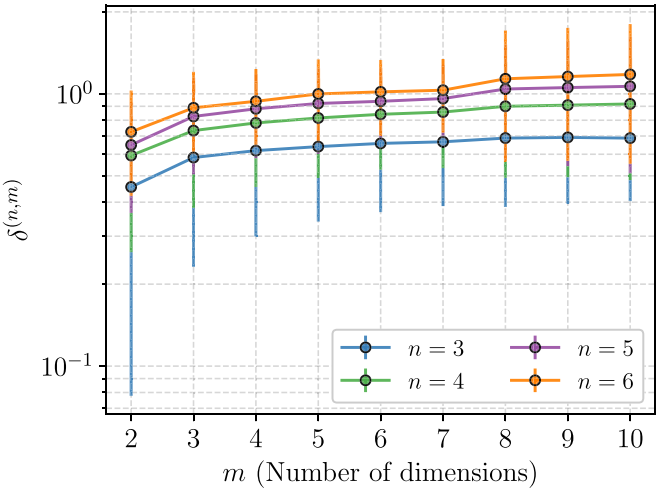


FIG. 24. $\delta^{(n,m)}$ [see Eq. (E6)] as a function of the number $m$ of dimensions, for selected sample sizes $n$. $\delta^{(n,m)}$ can be interpreted as the average distance of a point $a$ in an $n$-dimensional dataset to the corresponding best-fit line.

(3) Cross-check of $\boldsymbol{\Sigma_d}$ and the log-likelihood for $N_s = 10^2, 10^3, 10^4, 10^5$ samples. Check of the condition number of the covariance matrices and, by computing the spectral difference, Frobenius norm difference and the Kullback-Leibler divergence, comparison to the covariance matrices determined in *Mathematica*.

For $\alpha_{\rm NP} = 0$ and $\alpha_{\rm NP} = 10^{-11}$, comparison of the distribution of log-likelihood values for the $N_s$ samples obtained using `KIFIT` and *Mathematica*.

(4) Check of the numerical accuracy of the inversion of the covariance matrix $\boldsymbol{\Sigma_d}$.

(5) Tests of the symmetry of the `KIFIT` code with respect to exchange of the transitions or the choice of the reference transition (see discussion above), varying only the input parameters or varying both the input parameters and the fit parameters.

(6) Comparison of fit and algebraic methods for the test dataset `Ca24min_mod`.

(7) Test of the numerical impact of the regulation of the covariance matrix $\boldsymbol{\Sigma}_{\boldsymbol{d}}^{(\lambda)} = \boldsymbol{\Sigma_d} + \lambda \mathbf{I}_n$.

(8) Test `KIFIT` run procedure.

Finally, `test_cache_update` tests whether the `KIFIT`-internal cache is working and updated as expected.

## APPENDIX E: THE IMPACT OF DATA SPARSITY ON THE FIT

In this section we investigate how many data points (isotope pairs) are needed in a given number of dimensions (transitions) to ensure that the initial ODR is not over-fitting the data. We stress that the purpose of this analysis is to simulate the scaling of the relevant metrics in our estimation procedure with respect to the dimensionality of the King line ($m$) and the number of data points ($n$). The analysis is performed on mock data constructed from $N_s$ samples of $n$ "data points" $\{\{(x^{(a,s)}, y_1^{(a,s)}, \ldots, y_m^{(a,s)})\}_{a=1}^{n}\}_{s=1}^{N_s}$ which are normally distributed around a linear relation $y_j = b_j x + c_j$, $j = 1, \ldots, m$ with variance $\sigma_n$. The uncertainties on the mock data points are modeled using Gaussian random variables with variance $\sigma$.

Concretely, for a given number $n$ of points in $m$ dimensions, we generate the parameters

$$b_j, c_j \sim \mathcal{N}(0, 10), \quad j = 1, \ldots, m, \tag{E1}$$

which fix the linear relation $y_j = b_j x + c_j$ and then generate $N_s = 500$ samples ($s = 1, \ldots, N_s$) from the distributions

$$\begin{aligned} x^{(a,s)} &\sim \mathcal{N}(x^{(a)}, \sigma_n), \quad a = 1, \ldots, n, \\ y_j^{(a,s)} &\sim \mathcal{N}(b_j x^{(a)} + c_j, \sigma_n), \quad j = 1, \ldots, m, \\ \sigma[x^{(a,s)}], &\quad \sigma[y^{(a,s)}] \sim \mathcal{N}(0, \sigma), \end{aligned} \tag{E2}$$

where we take $\sigma_n = \sigma = 10^{-10}$. For each sample $\{(x^{(a,s)}, y_1^{(a,s)}, \ldots, y_m^{(a,s)})\}_{a=1}^{n}$ of the $n$ data points in $m$ dimensions, $2m$ fit parameters $\{(b_j^{(n,s)}, c_j^{(n,s)})\}_{j=1}^{m}$ are determined by means of orthogonal distance regression.

As a first check, we compute the combined fractional differences of the fit parameter samples with respect to the

original slopes and intercepts $\{(b_j, c_j)\}_{j=1}^{m}$,

$$\zeta^{(n,s)} = \sqrt{\sum_{j=2}^{m}\left(\frac{\left(b_j^{(n,s)} - b_j\right)^2}{b_j^2} + \frac{\left(c_j^{(n,s)} - c_j\right)^2}{c_j^2}\right)}. \quad \text{(E3)}$$

The averages and standard deviations over the samples, $\zeta^{(n)} \equiv \langle \zeta^{(n,s)} \rangle_{(s)}$ and $\sigma[\zeta^{(n,s)}]_{(s)}$ can be viewed as a measure of the error in the fit parameters due to the finite sample size $n$. They are plotted in Fig. 22 as a function of the number of points $n$. As expected, $\zeta^{(n)}$ approximately follows a relation of the form $f(n) = \theta_1/\sqrt{n-\theta_2} + \theta_3$, which is motivated by the expected asymptotic behavior of Gaussian uncertainties, by the fact that a linear fit to one point is ill-defined and by the finite number of $n$ values considered for the curve fit. The explicit parameters obtained when fitting the first 15 data points for $m = 2$ to this curve are $(\theta_1, \theta_2, \theta_3) \approx (1.5 \times 10^{-9}, 1.7, -3 \times 10^{-10})$.

Since relevant quantity for the log-likelihood in Eq. (52) is the distance of the points from the line, normalized by the respective uncertainties, we apply a definition very similar to that used in KIFIT [see Eqs. (48), (38), and (49)]:

$$\delta^{(a,m,s)} = \frac{1}{\sigma\sqrt{m}} \|\mathbf{\Delta}^{(a,m,s)} - (\mathbf{\Delta}^{(a,m,s)} \cdot \hat{\boldsymbol{e}}_f)\hat{\boldsymbol{e}}_f\|, \quad \text{(E4)}$$

with

$$\mathbf{\Delta}^{(a,m,s)} = \begin{pmatrix} 0 \\ y_1^{(a,s)} - \left(b_1^{(a,s)} x^{(a,s)} + c_1^{(a,s)}\right) \\ \vdots \\ y_m^{(a,s)} - \left(b_m^{(a,s)} x^{(a,s)} + c_m^{(a,s)}\right) \end{pmatrix}, \quad \text{(E5)}$$

and $\hat{\boldsymbol{e}}_f = (1, b_1^{(a,s)}, \ldots, b_m^{(a,s)})$, and a normalization $\sigma\sqrt{m}$ that captures the asymptotic behavior of the uncertainties on the sum. We then define

$$\delta^{(n,m)} \equiv \left\langle \frac{1}{n}\sum_{a=1}^{n} \delta^{(a,m,s)} \right\rangle_{(s)},$$

$$\sigma[\delta^{(n,m)}] \equiv \sigma\left[\frac{1}{n}\sum_{a=1}^{n} \delta^{(a,m,s)}\right]_{(s)}, \quad \text{(E6)}$$

where $\langle . \rangle_{(s)}$ and $\sigma[.]_{(s)}$ denote the average and the standard deviation over the samples $(s)$. In Fig. 23, $\delta^{(n,m)}$ and $\sigma[\delta^{(n,m)}]$ are plotted as a function of the number $n$ of points and for different dimensions $m$. $\delta^{(n,m)}$ can be viewed as the average distance, normalized by the experimental uncertainties, of a point $a$ in a dataset of size $n$ to the best-fit line. $\delta^{(n,m)}$ increases with $n$ because the uncertainty on the distance to the line receives an additional contribution from the increasing spread of the data points, which for the mock data employed here has variance $\sigma_n$ [see Eq. (E2)]. This residual $n$ dependence is again captured by a function of the form $f(n) = \theta_1/\sqrt{n-\theta_2} + \theta_3$, this time with $(\theta_1, \theta_2, \theta_3) \approx (-0.6, 1.6, 1)$ for the first 15 points in $m = 2$ dimensions. Figure 23 shows that increasing the number of data points from three by a few can significantly improve the reliability of the fit results.

The $m$ dependence of $\delta^{(n,m)}$ is less pronounced, as can be observed in Fig. 24. Nonetheless, measurements of additional transitions can improve the heterogeneity of the data and thus the reliability of the bounds on $\alpha_{\mathrm{NP}}$.

## APPENDIX F: ISOTOPE SHIFT AND ATOMIC AND NUCLEAR MASS DATA

In Tables IX and X, we collect the available isotope shift measurements for Ca and Yb. The most recent measurements for the isotope masses can be found in Tables VII and VIII. We mark with an asterisk the values that are included in the KIFIT folders.

TABLE VII. Atomic masses of Ca isotopes from Refs. [65,112]. The third column shows the ratios of bare nuclear masses to the mass of isotope $A = 40$, as reported in Ref. [43].

| Isotope A | $m_A$ [u] [112] | $m_A$ [u] [65] | $m_A/m_{40}$ [43] |
|---|---|---|---|
| 40 | 39.962 590 866(22) | 39.962 590 851(22) | 1 |
| 42 | 41.958 617 83(16) | 41.958 617 78(16) | 1.049 961 066 498(15) |
| 44 | 43.955 4815(3) | 43.955 481 5(3) | 1.099 943 105 797(15) |
| 46 | 45.953 688 0(24) | 45.953 687 7(24) | 1.149 958 773 895(30) |
| 48 | 47.952 522 90(10) | 47.952 522 654(19) | 1.199 990 087 090(40) |

TABLE VIII. Atomic masses of Yb isotopes from Refs. [65,112]. The third column shows ratios of bare nuclear masses to the mass of isotope $A = 172$, as reported in Ref. [50].

| Isotope A | $m_A$ [u] [112] | $m_A$ [u] [65] | $m_A/m_{172}$ [50] |
|---|---|---|---|
| 168 | 167.933 889 1(13) | 167.933 891 30(10) | 0.976 715 921 749(4) |
| 170 | 169.934 767 246(11) | 169.934 767 243(11) | 0.988 355 799 258(4) |
| 172 | 171.936 386 659(15) | 171.936 386 654(15) | 1 |
| 174 | 173.938 867 548(12) | 173.938 867 546(12) | 1.011 649 212 140(4) |
| 176 | 175.942 574 709(16) | 175.942 574 706(16) | 1.023 305 557 965(4) |

TABLE IX. Isotope shifts of $Ca^+$ and $Ca^{14+}$, expressed in Hz. Values included in KIFIT are marked with an asterisk. Notice that Ref. [42] reports measurements of the $4^2S_{1/2} \rightarrow 3^2D_{3/2}$ transition, and the corresponding DD-transition values are derived therein from their measurement of $4^2S_{1/2} \rightarrow 3^2D_{3/2}$ and the $4^2S_{1/2} \rightarrow 3^2D_{5/2}$ reported in Refs. [40,41,109]. Similarly, the DD-transition values reported in Ref. [43] are derived from their measurement of $4^2S_{1/2} \rightarrow 3^2D_{5/2}$ and the $4^2S_{1/2} \rightarrow 3^2D_{3/2}$ reported in Ref.[42].

| $(A, A')$ | $Ca^+$:$4^2S_{1/2} \rightarrow 3^2D_{5/2}$ [Hz] (729 nm) | $Ca^+$:$3^2D_{3/2} \rightarrow 3^2D_{5/2}$ [Hz] (DD) | $Ca^+$:$4s^2S_{1/2} \rightarrow 4p^2P_{1/2}$ [Hz] (397 nm) |
|---|---|---|---|
| (40, 42) | *2 771 872 467.6(7.6) [40] | *−3 519 896(24) [41] | *425 706 000(94 000) [26] |
| | 2 771 873 000(2 000) [41] | *−3 519 910(9.7) [42] | 425 490 000(150 000) [113] |
| | 2 771 872 430.217(27) [43] | −3 519 944.6(60) [43] | |
| (40, 44) | *5 340 887 394.6(7.8) [40] | *−6 792 470(22) [41] | *849 534 000(74 000) [26] |
| | 5 340 888 000(2 000) [41] | *−6 792 440(6) [42] | 849 000 000(140 000) [113] |
| | 5 340 887 395.288(38) [43] | −6 792 440.1(59) [43] | |
| (40, 46) | *7 768 401 000(2 000) [41] | *−9 901 524(21) [41] | *1 297 610 000(340 000) [113] |
| | 7 768 401 432.916(63) [43] | *−9 901 520(2828.43) [42] | |
| | | −9 901 524(21) [43] | |
| (40, 48) | 9 990 382 525.0(4.9) [109] | −12 746 610(27) [41] | 1 705 389 000(60 000) [26] |
| | 9 990 383 000(2 000) [41] | *−12 746 600(7.5) [42] | 1 705 460 000(140 000) [113] |
| | 9 990 382 526.834(55) [43] | −12 746 588.2(57) [43] | |
| $(A, A')$ [Hz] | $Ca^+$:$4^2S_{1/2} \rightarrow 3^2D_{3/2}$ [Hz] (732 nm) | $Ca^+$: $4^2S_{1/2} \rightarrow 4p\,^2P_{3/2}$ [Hz] (393 nm) | $Ca^+$:$3d^2D_{3/2} \rightarrow 4p^2P_{1/2}$ [Hz] (866 nm) |
| (40, 42) | 2 775 392 374.8(6.0) [42] | 426 040 000(150 000) [113] | *−2 349 974 000(99 000) [26] |
| | | 425 932 000 (71 000) [27] | 2 366 000 000(59 000 000) [114] |
| | | | 2 352 100 000(2 100 000) [38] |
| (40, 44) | 5 347 679 835.4(5.9) [42] | 850 090 000(140 000) [113] | *−4 498 883 000(80 000) [26] |
| | | 850 231 000(65 000) [27] | 4 509 000 000(24 000 000) [114] |
| | | | 4 499 300 000(2 300 000) [38] |
| (40, 46) | | 1 299 070 000(580 000) [113] | |
| | | 1 301 000 000(3 600 000) [115] | |
| (40, 48) | 10 003 129 115.1(5.7) [42] | 1 707 580 000(160 000) [113] | *−8 297 769 000(81 000) [26] |
| | | 1 707 945 000(67 000) [27] | 8 296 700 000(3 200 000) [38] |
| $(A, A')$ | $Ca^+$: $^2D_{5/2} \rightarrow ^2P_{3/2}$ [Hz] (854 nm) | $Ca^+$:$^2D_{3/2} \rightarrow ^2P_{3/2}$ [Hz] (850 nm) | $Ca^{14+}$: $^3P_0 \rightarrow ^3P_1$ [Hz] (570 nm) |
| (40, 42) | 2 272 000 000(94 000 000) [114] | 2 359 000 000(64 000 000) [114] | 539 088 421.24(12) [43] |
| | 2 347 600 000(3 900 000) [38] | 2 351 450 000(700 000) [38] | |
| (40, 44) | 4 510 000 000(19 000 000) [114] | 4 538 000 000(27 000 000) [114] | 1 030 447 731.64(11) [43] |
| | 4 489 800 000(3 600 000) [38] | 4 497 270 000(900 000) [38] | |
| (40, 46) | 6 470 100 000(2 400 000) [38] | | 1 481 135 946.74(14) [43] |
| (40, 48) | 8 277 900 000(5 000 000) [38] | 8 295 060 000(1 100 000) [38] | 1 894 297 294.53(14) [43] |

TABLE X. Isotope shifts for Yb and $Yb^+$, expressed in Hz. Values included in KIFIT are marked with an asterisk. Isotopes used in this work are organized in pairs $(A, A')$ with $A' = A + 2$. The data for the other isotope pairs can be used for cross-checks.

| $(A, A')$ | ($\alpha$) $Yb^+$:$^2S_{1/2} \rightarrow ^2 D_{5/2}$ [Hz] (411 nm) | ($\beta$) $Yb^+$:$^2S_{1/2} \rightarrow ^2 D_{3/2}$ [Hz] (436 nm) | ($\gamma$) $Yb^+$: $^2S_{1/2} \rightarrow ^2 F_{7/2}$ [Hz] (467 nm) |
|---|---|---|---|
| (168, 170) | *2 179 098 930(210) [48]<br>*2 179 098 868.0(5.3) [50] | *2 212 391 850(370) [48] | *−4 438 160 300(500) [49]<br>*−4 438 159 671.1(15.7) [50] |
| (170, 172) | *2 044 854 780(340) [48]<br>*2 044 851 281.0(4.9) [50] | *2 076 421 580(390) [48] | *−4 149 190 380(450) [49]<br>*−4 149 190 501.1(15.7) [50] |
| (172, 174) | *1 583 068 420(360) [48]<br>*1 583 064 149.3(4.8) [50] | *1 609 181 470(220) [48] | *−3 132 321 600(500) [49]<br>*−3 132 320 458.1(15.7) [50] |
| (174, 176) | *1 509 055 290(280) [48]<br>*1 509 053 195.8(4.7) [50] | *1 534 144 060(240) [48] | *−2 976 391 600(480) [49]<br>*−2 976 392 045.3(15.7) [50] |
| (168, 172) | | | −8 587 352 000(470) [49] |
| (170, 174) | 3 627 922950(500) [48] | 3 685 601950(330) [48] | −7 281 511 880(450) [49] |
| (172, 176) | | | −6 108 712 930(440) [49] |

| $(A, A')$ | ($\epsilon$) Yb:$^1S_0 \rightarrow ^1 D_2$ [Hz] (361 nm) | ($\delta$) Yb:$^1S_0 \rightarrow ^3 P_0$ [Hz] (578 nm) | Yb:$4f^{14}6s^{21}S_0 \longleftrightarrow 4f^{13}5d^6s^2$ [Hz] (431 nm) |
|---|---|---|---|
| (168, 170) | *1 781 785 360(710) [47] | *1 358 484 476.2(2.2)$_{tot}$ [71] | −1 753 930 000(3 000)$_{stat}$ [116]<br>−1 753 952 000(26 000) [72] |
| (170, 172) | *1 672 021 510(300) [47] | *1 275 772 006(2.8)$_{stat}$ [71] | −1 630 050 000(3 000)$_{stat}$ [116]<br>−1 630 028 000(26 000) [72] |
| (172, 174) | *1 294 454 440(240) [47] | *992 714 586.6(2.1)$_{tot}$ [71] | −1 180 614 000(2 000)$_{stat}$ [116]<br>−1 180 616 000(25 000) [72] |
| (174, 176) | *1 233 942 190(310) [47] | *946 921 774.9(2.9)$_{tot}$ [71] | −1 115 766 000(6 000)$_{stat}$ [116]<br>−1 115 787 000(24 000) [72] |
| (168, 172) | 3 453 805 270(83) [47] | | |
| (172, 176) | 2 528 396 500(34) [47] | | |

| $(A, A')$ | $Yb^+$: $6^2S_{1/2} \rightarrow 6^2P^o_{1/2}$ [Hz] (369 nm) | $Yb^+$:$6^2S_{1/2} \rightarrow 6^2P^o_{3/2}$ [Hz] (329 nm) | Yb: $6^1S_0 \rightarrow 6^3P^o_1$ [Hz] (556 nm) |
|---|---|---|---|
| (168, 170) | | | 1 368 630 000(500 000) [44] |
| (170, 172) | −1 623 300 000(800 000) [117] | −1 459 000 000(21 000 000) [118] | 1 286 470 000(500 000) [44] |
| (172, 174) | −1 275 300 000(700 000) [117] | −1 154 000 000(11 000 000) [118] | 1 000 280 000(500 000) [44] |
| (174, 176) | | | 954 760 000(500 000) [44]<br>954 734 000(31 000) [119] |
| (168, 176) | | | 4 610 944 000(58 000) [119] |
| (170, 176) | | | 3 241 342 000(73 000) [119] |
| (172, 176) | −2 492 800 000(1 000 000) [117] | −2 259 000 000(13 000 000) [118] | 1 955 526 000(36 000) [119] |

| $(A, A')$ | $Yb^+$: $^1S_0 \rightarrow ^1 P_1$ [Hz] (399 nm) |
|---|---|
| (174, 168) | 1 888 800 000(110 000) [46] |
| (174, 170) | 1 190 360 000(490 000) [46] |
| (174, 172) | 531 110 000(90 000) [46] |
| (174, 176) | −508 890 000(90 000) [46] |


[1] M. S. Safronova, D. Budker, D. DeMille, D. F. J. Kimball, A. Derevianko, and C. W. Clark, Search for New Physics with Atoms and Molecules, Rev. Mod. Phys. **90**, 025008 (2018).

[2] M. G. Kozlov, M. S. Safronova, J. R. Crespo López-Urrutia, and P. O. Schmidt, Highly charged ions: Optical clocks and applications in fundamental physics, Rev. Mod. Phys. **90**, 045005 (2018).

[3] D. Antypas *et al.*, New horizons: Scalar and vector ultralight dark matter, arXiv:2203.14915.

[4] T. W. Hänsch and A. L. Schawlow, Cooling of gases by laser radiation, Opt. Commun. **13**, 68 (1975).

[5] D. J. Wineland and H. Dehmelt, Proposed $10^{14}\Delta\upsilon < \upsilon$ laser fluorescence spectroscopy on $tl^+$ mono-ion oscillator iii, Bull. Am. Phys. Soc. **20**, 637 (1975).

[6] S. Stenholm, The semiclassical theory of laser cooling, Rev. Mod. Phys. **58**, 699 (1986).

[7] H. Metcalf and P. van der Straten, Cooling and trapping of neutral atoms, Phys. Rep. **244**, 203 (1994).

[8] T. W. Hänsch, Nobel lecture: Passion for precision, Rev. Mod. Phys. **78**, 1297 (2006).

[9] J. L. Hall, Nobel lecture: Defining and measuring optical frequencies, Rev. Mod. Phys. **78**, 1279 (2006).

[10] A. Ashkin, Acceleration and trapping of particles by radiation pressure, Phys. Rev. Lett. **24**, 156 (1970).

[11] A. Ashkin, J. M. Dziedzic, J. E. Bjorkholm, and S. Chu, Observation of a single-beam gradient force optical trap for dielectric particles, Opt. Lett. **11**, 288 (1986).

[12] S. Chu, J. E. Bjorkholm, A. Ashkin, and A. Cable, Experimental observation of optically trapped atoms, Phys. Rev. Lett. **57**, 314 (1986).

[13] V. S. Letokhov, Narrowing of the Doppler Width in a Standing Wave, Sov. J. Exp. Theor. Phys. Lett. **7**, 348 (1968).

[14] V I Balykin, V S Letokhov, and V G Minogin, Laser control of the motion of neutral atoms and optical atomic traps, Phys. Scr. **T22**, 119 (1988).

[15] F. Mauri and E. Arimondo, Two dimension selective coherent population trapping controlled by a phase shift, Appl. Phys. B **54**, 420 (1992).

[16] R. Grimm, M. Weidemüller, and Y. B. Ovchinnikov, Optical dipole traps for neutral atoms, Adv. At. Mol. Phys. **42**, 95 (2000).

[17] P. O. Schmidt, T. Rosenband, C. Langer, W. M. Itano, J. C. Bergquist, and D. J. Wineland, Spectroscopy using quantum logic, Science **309**, 749 (2005).

[18] D. J. Heinzen and D. J. Wineland, Quantum-limited cooling and detection of radio-frequency oscillations by laser-cooled ions, Phys. Rev. A **42**, 2977 (1990).

[19] J. I. Cirac and P. Zoller, Quantum computations with cold trapped ions, Phys. Rev. Lett. **74**, 4091 (1995).

[20] D. J. Wineland, C. Monroe, W. M. Itano, D. Leibfried, B. E. King, and D. M. Meekhof, Experimental issues in coherent quantum state manipulation of trapped atomic ions, J. Res. Natl. Inst. Stand. Technol. **103**, 259 (1998).

[21] A. Aeppli, K. Kim, W. Warfield, M. S. Safronova, and J. Ye, Clock with $8 \times 10^{-19}$ systematic uncertainty, Phys. Rev. Lett. **133**, 023401 (2024).

[22] H. N. Hausser, J. Keller, T. Nordmann, N. M. Bhatt, J. Kiethe, H. Liu, I. M. Richter, M. von Boehn, J. Rahm, S. Weyers, E. Benkler, B. Lipphardt, S. Dörscher, K. Stahl, J. Klose, C. Lisdat, M. Filzinger, N. Huntemann, E. Peik, and T. E. Mehlstäubler, $^{115}In^{+} - ^{172}Yb^{+}$ coulomb crystal clock with $2.5 \times 10^{-18}$ systematic uncertainty, Phys. Rev. Lett. **134**, 023201 (2025).

[23] W. H. King, Comments on the article "Peculiarities of the isotope shift in the samarium spectrum,"J. Opt. Soc. Am. **53**, 638 (1963).

[24] W. H. King, *Isotope Shifts in Atomic Spectra* (Springer Science & Business Media, New York, 1984).

[25] I. Angeli and K.P. Marinova, Table of experimental nuclear ground state charge radii: An update, At. Data Nucl. Data Tables **99**, 69 (2013).

[26] F. Gebert, Y. Wan, F. Wolf, C. N. Angstmann, J. C. Berengut, and P. O. Schmidt, Precision isotope shift measurements in calcium ions using quantum logic detection schemes, Phys. Rev. Lett. **115**, 053003 (2015).

[27] C. Shi, F. Gebert, .C Gorges, S. Kaufmann, W. Nörtershäuser, B. K. Sahoo, A. Surzhykov, V. A. Yerokhin, J. C. Berengut, F. Wolf *et al.*, Unexpectedly large difference of the electron density at the nucleus in the $4p^2P_{1/2,3/2}$fine-structure doublet of $Ca^{+}$, Appl. Phys. B, **123**2 (2018)..

[28] C. Delaunay, R. Ozeri, G. Perez, and Y. Soreq, Probing atomic higgs-like forces at the precision frontier, Phys. Rev. D **96**, 093001 (2017).

[29] J. C. Berengut *et al.*, Probing new long-range interactions by isotope shift spectroscopy, Phys. Rev. Lett. **120**, 091801 (2018).

[30] M. Bordag, G. L. Klimchitskaya, U. Mohideen, and V. M. Mostepanenko, *Advances in the Casimir Effect* (Oxford University Press, 2009).

[31] R. Essig, P. Schuster, and N. Toro, Probing dark forces and light hidden sectors at low-energy $e^{+}e^{-}$ colliders, Phys. Rev. D **80**, 015003 (2009).

[32] R. Essig, P. Schuster, N. Toro, and B. Wojtsekhowski, An electron fixed target experiment to search for a new vector boson A' decaying to e+e-, J. High Energy Phys. 02 (2011) 009.

[33] B. Batell, M. Pospelov, and A. Ritz, Exploring portals to a hidden sector through fixed targets, Phys. Rev. D **80**, 095024 (2009).

[34] J. P. Lees *et al.* (BaBar Collaboration), Search for $B \to K^{(*)}\nu\bar{\nu}$ and invisible quarkonium decays, Phys. Rev. D **87**, 112005 (2013).

[35] A. V. Artamonov *et al.* (E949 Collaboration), New measurement of the $K^{+} \to \pi^{+}\nu\bar{\nu}$ branching ratio, Phys. Rev. Lett. **101**, 191802 (2008).

[36] C. Frugiuele, E. Fuchs, G. Perez, and M. Schlaffer, Constraining new physics models with isotope shift spectroscopy, Phys. Rev. D **96**, 015011 (2017).

[37] S. Knapen, T. Lin, and K. M. Zurek, Light dark matter: Models and constraints, Phys. Rev. D **96**, 115021 (2017).

[38] A. Kramida, Isotope shifts in neutral and singly-ionized calcium, At. Data Nucl. Data Tables **133-134**, 101322 (2020).

[39] D. Röser, L. Möller, H. Keßler, and S. Stellmer, Isotope-shift measurement of the 423-nm transition in neutral Ca, Phys. Rev. A **110**, 032809 (2024).

[40] F. W. Knollmann, A. N. Patel, and S. Charles Doret, Part-per-billion measurement of the $4^2S_{1/2} \to 3^2D_{5/2}$ electric-quadrupole-transition isotope shifts between $^{42,44,48}Ca^{+}$ and $^{40}Ca^{+}$, Phys. Rev. A **100**, 022514 (2019).

[41] C. Solaro, S. Meyer, K. Fisher, J. C. Berengut, E. Fuchs, and M. Drewsen, Improved isotope-shift-based bounds on bosons beyond the standard model through measurements of the $^2D_{3/2} - ^2D_{5/2}$ interval in $Ca^{+}$, Phys. Rev. Lett. **125**, 123003 (2020); Erratum: Improved isotope-shift-based bounds on bosons beyond the standard model through measurements of the $^2D_{3/2} - ^2D_{5/2}$ interval in $Ca^{+}$ [Phys. Rev. Lett. 125, 123003 (2020)], **127**, 029901(E) (2021).

[42] T. T. Chang, B. B. Awazi, J. C. Berengut, E. Fuchs, and S. C. Doret, Systematic-free limit on new light scalar bosons via isotope-shift spectroscopy in $Ca^{+}$, Phys. Rev. A **110**, L030801 (2024).

[43] A. Wilzewski *et al.*, Nonlinear calcium King plot constrains new bosons and nuclear properties, Phys. Rev. Lett. **134**, 233002 (2025).

[44] D. L. Clark, M. E. Cage, D. A. Lewis, and G. W. Greenlees, Optical isotopic shifts and hyperfine splittings for Yb, Phys. Rev. A **20**, 239 (1979).

[45] C. J. Bowers, D. Budker, S. J. Freedman, G. Gwinner, J. E. Stalnaker, and D. DeMille, Experimental investigation of the $6s^2\,{}^1S_0 \rightarrow 5d6s^3D_{1,2}$ forbidden transitions in atomic ytterbium, Phys. Rev. A **59**, 3513 (1999).

[46] M. Kleinert, M. E. Gold Dahl, and S. Bergeson, Measurement of the Yb I ${}^1S_0 - {}^1P_1$ transition frequency at 399 nm using an optical frequency comb, Phys. Rev. A **94**, 052511 (2016).

[47] N. L. Figueroa, J. C. Berengut, V. A. Dzuba, V. V. Flambaum, D. Budker, and D. Antypas, Precision determination of isotope shifts in ytterbium and implications for new physics, Phys. Rev. Lett. **128**, 073001 (2022).

[48] I. Counts, J. Hur, D. P. L. Aude Craik, H. Jeon, C. Leung, J. C. Berengut, A. Geddes, A. Kawasaki, W. Jhe, and V. Vuletić, Evidence for nonlinear isotope shift in $Yb^+$ search for new boson, Phys. Rev. Lett. **125**, 123002 (2020).

[49] J. Hur *et al.*, Evidence of two-source king plot nonlinearity in spectroscopic search for new boson, Phys. Rev. Lett. **128**, 163201 (2022).

[50] M. Door *et al.*, Probing new bosons and nuclear structure with ytterbium isotope shifts, Phys. Rev. Lett. **134**, 063002 (2025).

[51] S. O. Allehabi, V. A. Dzuba, V. V. Flambaum, and A. V. Afanasjev, Nuclear deformation as a source of the nonlinearity of the King plot in the $Yb^+$ ion, Phys. Rev. A **103**, L030801 (2021).

[52] A. V. Viatkina, V. A. Yerokhin, and A. Surzhykov, Calculation of isotope shifts and King-plot nonlinearities in $Ca^+$, Phys. Rev. A **108**, 022802 (2023).

[53] J. C. Berengut, C. Delaunay, A. Geddes, and Y. Soreq, Generalized King linearity and new physics searches with isotope shifts, Phys. Rev. Res. **2**, 043444 (2020).

[54] J. C. Berengut and C. Delaunay, Precision isotope-shift spectroscopy for new physics searches and nuclear insights, Nat. Rev. Phys. **7**, 119 (2025).

[55] C. Palmer and D. N. Stacey, Theory of anomalous isotope shifts in samarium, J. Phys. B: At. Mol. Phys. **15**, 997 (1982).

[56] J. C. Berengut and N. S. Oreshkina, Second-order hyperfine structure in strontium and impact on new physics searches using isotope shift spectroscopy, arXiv:2409.01530 [physics.atom-ph].

[57] S. Hofsäss, J. E. Padilla-Castillo, S. C. Wright, S. Kray, R. Thomas, B. G. Sartakov, B. Ohayon, G. Meijer, and S. Truppe, High-resolution isotope-shift spectroscopy of Cd I, Phys. Rev. Res. **5**, 013043 (2023).

[58] D. Röser, J. E. Padilla-Castillo, B. Ohayon, R. Thomas, S. Truppe, G. Meijer, S. Stellmer, and S. C. Wright, Hyperfine structure and isotope shifts of the $(4s^2)^1S_0 \rightarrow (4s4p)^1P_1$ transition in atomic zinc, Phys. Rev. A **109**, 012806 (2024).

[59] E.V. Kahl and J.C. Berengut, ambit: A programme for high-precision relativistic atomic structure calculations, Comput. Phys. Commun. **238**, 232 (2019).

[60] G. Breit, Theory of isotope shift, Rev. Mod. Phys. **30**, 507 (1958).

[61] D N Stacey, Isotope shifts and nuclear charge distributions, Rep. Prog. Phys. **29**, 171 (1966).

[62] K. Heilig and A. Steudel, Changes in mean-square nuclear charge radii from optical isotope shifts, Rep. Prog. Phys. **14**, 613 (1974), Nuclear Charge and Moment Distributions.

[63] C. W. P. Palmer, Reformulation of the theory of the mass shift, J. Phys. B: At. Mol. Phys. **20**, 5987 (1987).

[64] S. A. Blundell, P. E. G. Baird, C. W. P. Palmer, D. N. Stacey, and G. K. Woodgate, A reformulation of the theory of field isotope shift in atoms, J. Phys. B: At. Mol. Phys. **20**, 3663 (1987).

[65] M. Wang, W. J. Huang, F. G. Kondev, G. Audi, and S. Naimi, The AME 2020 atomic mass evaluation (II). Tables, graphs and references, Chin. Phys. C **45**, 030003 (2021).

[66] A. S. J. E. Hansen and H. Walther, Isotopieverschiebung der natürlichen geraden und ungeraden Sm- und Nd-Isotope, Eur. Phys. J. A **203**, 296 (1967).

[67] C. W. P. Palmer, P. E. G. Baird, S. A. Blundell, J. R. Brandenberger, C. J. Foot, D. N. Stacey, and G. K. Woodgate, Laser spectroscopy of calcium isotopes, J. Phys. B: At. Mol. Phys. **17**, 2197 (1984).

[68] H. E. Haber, G. L. Kane, and T. Sterling, The Fermion Mass Scale and Possible Effects of Higgs Bosons on Experimental Observables, Nucl. Phys. B **161**, 493 (1979).

[69] A. R. Striganov, V. A. Katulin, and V. V. Eliseev, Peculiarities of the isotopic shift in the samarium spectrum, Opt. Spectrosc. (USSR)(Engl. Transl.) **2** (1962).

[70] D.N. Stacey, A note on the interpretation of isotope shifts, Phys. Lett. **20**, 644 (1966).

[71] K. Ono, Y. Saito, T. Ishiyama, T. Higomoto, T. Takano, Y. Takasu, Y. Yamamoto, M. Tanaka, and Y. Takahashi, Observation of nonlinearity of generalized King plot in the search for new boson, Phys. Rev. X **12**, 021033 (2022).

[72] A. Kawasaki, T. Kobayashi, A. Nishiyama, T. Tanabe, and M. Yasuda, Isotope shift analysis with the $4f^{14}6s^2\,{}^1S_0$–$4f^{13}5d6s^2(J=2)$ transition in ytterbium, Phys. Rev. A **109**, 062806 (2024).

[73] B. Ohayon, S. Hofsäss, J. E. Padilla-Castillo, S. C. Wright, G. Meijer, S. Truppe, K. Gibble, and B. K. Sahoo, Isotope shifts in cadmium as a sensitive probe for physics beyond the standard model, New J. Phys. **24**, 123040 (2022).

[74] V. V. Flambaum, A. J. Geddes, and A. V. Viatkina, Isotope shift, nonlinearity of King plots, and the search for new particles, Phys. Rev. A **97**, 032510 (2018).

[75] V. V. Flambaum and V. A. Dzuba, Sensitivity of the isotope shift to the distribution of nuclear charge density, Phys. Rev. A **100**, 032511 (2019).

[76] C. Delaunay, C. Frugiuele, E. Fuchs, and Y. Soreq, Probing new spin-independent interactions through precision spectroscopy in atoms with few electrons, Phys. Rev. D **96**, 115002 (2017).

[77] M. P. A. Jones, R. M. Potvliege, and M. Spannowsky, Probing new physics using Rydberg states of atomic hydrogen, Phys. Rev. Res. **2**, 013244 (2020).

[78] R. M. Potvliege, A. Nicolson, M. P. A. Jones, and M. Spannowsky, Deuterium spectroscopy for enhanced bounds on physics beyond the standard model, Phys. Rev. A **108**, 052825 (2023).

[79] R. M. Potvliege, Spectroscopy of light atoms and bounds on physics beyond the standard model, New J. Phys. **27**, 045002 (2025).

[80] https://github.com/QTI-TH/kifit.

[81] P. T. Boggs and J. E. Rogers, Orthogonal Distance Regression (National Institute of Standards and Technology, Gaithersburg, MD, 1990).

[82] P. Virtanen, R. Gommers, T. E. Oliphant, M. Haberland, T. Reddy, D. Cournapeau, E. Burovski, P. Peterson, W. Weckesser, J. Bright, Stéfan J. van der Walt, M. Brett, J. Wilson, K. J. Millman, N. Mayorov, A. R. J. Nelson, E. Jones, R. Kern, E. Larson, C. J. Carey *et al.*, SciPy 1.0: Fundamental algorithms for scientific computing in python, Nat. Methods **17**, 261 (2020).

[83] M. Pourahmadi, Cholesky decompositions and estimation of a covariance matrix: Orthogonality of variance–correlation parameters, Biometrika **94**, 1006 (2007).

[84] H. Flyvbjerg and H.G. Petersen, Error estimates on averages of correlated data, J. Chem. Phys. **91**, 461 (1989).

[85] A. T. Goble, J. D. Silver, and D. N. Stacey, Isotope shifts in the atomic spectrum of tin: $^{112}$Sn, $^{114}$Sn and $^{115}$Sn, J. Phys. B: At. Mol. Phys. **7**, 26 (1974).

[86] J. Choi, E. Lee, D. Yum, K. An, and J. Kim, Direct measurement of isotope shifts in the barium $6s^2\,{}^1S_0$–$5d6p\,{}^3D_1^o$ transition, Phys. Rev. A **110**, 032812 (2024).

[87] T. Ishiyama, K. Ono, H. Kawase, T. Takano, R. Asano, A. Sunaga, Y. Yamamoto, M. Tanaka, and Y. Takahashi, Orders-of-magnitude improved precision spectroscopy of an inner-shell orbital clock transition in neutral ytterbium, arXiv:2505.04154.

[88] J. Han, Y. Zheng, Y. Yu, J. Li, Z. Huang, J. Wen, L. Qian, and L. Wang, Enhanced accuracy of isotope-shift measurements of $Yb^+$ 369- and 935-nm transitions via sympathetic cooling, Phys. Rev. A **111**, 033101 (2025).

[89] N. A. Diepeveen, C. Robalo Pereira, M. Mazzanti, Z. E. D. Ackerman, L. P. H. Gallagher, T. Timmerman, R. Gerritsma, and R. X. Schüssler, Single-ion spectroscopy of four metastable-state clear-out transitions in $Yb^+$: Isotope shifts and hyperfine structure, Phys. Rev. A **110**, 042809 (2024).

[90] T. Ando, K. Yamada, A. Iwasaki, and K. Yamanouchi, Isotope shift of fine structure of $Kr^+$ and hyperfine structure of $^{83}Kr^+$ by strong-field ultrahigh-resolution Fourier-transform spectroscopy, Phys. Rev. Res. **7**, L022025 (2025).

[91] G. Zitzer, J. Tiedau, Ch. E. Düllmann, M. V. Okhapkin, and E. Peik, Laser spectroscopy on the hyperfine structure and isotope shift of sympathetically cooled $^{229}Th^{3+}$ ions, Phys. Rev. A **111**, L050802 (2025).

[92] J. S. Schelfhout and J. J. McFerran, Multiconfiguration Dirac-Hartree-Fock calculations for Hg and Cd with estimates for unknown clock-transition frequencies, Phys. Rev. A **105**, 022805 (2022).

[93] M. Witkowski, G. Kowzan, R. Munoz-Rodriguez, R. Ciuryło, P. S. Żuchowski, P. Masłowski, and M. Zawada, Absolute frequency and isotope shift measurements of mercury $^1S_0 \rightarrow {}^3P_1$ transition, Opt. Express **27**, 11069 (2019).

[94] S. Gravina, N. A. Chishti, S. Di Bernardo, E. Fasci, A. Castrillo, A. Laliotis, and L. Gianfrani, Comb-referenced doppler-free spectrometry of the $^{200}$Hg and $^{202}$Hg intercombination line at 254 nm, Phys. Rev. Lett. **132**, 213001 (2024).

[95] M. D. Rayman, C. G. Aminoff, and J. L. Hall, Precise laser frequency scanning using frequency-synthesized optical frequency sidebands: Application to isotope shifts and hyperfine structure of mercury, J. Opt. Soc. Am. B **6**, 539 (1989).

[96] A. Kramida, Re-optimized energy levels and Ritz wavelengths of $^{198}$Hg I, J. Res. Natl. Inst. Stand. Technol. **116**, 599 (2011).

[97] R. Tyumenev, M. Favier, S. Bilicki, E. Bookjans, R L. Targat, J. Lodewyck, D. Nicolodi, Y. L. Coq, M. Abgrall, J. Guéna, L D. Sarlo, and S. Bize, Comparing a mercury optical lattice clock with microwave and optical frequency standards, New J. Phys. **18**, 113002 (2016).

[98] M. Petersen, R. Chicireanu, S. T. Dawkins, D. V. Magalhães, C. Mandache, Y. Le Coq, A. Clairon, and S. Bize, Doppler-free spectroscopy of the $^1S_0$–$^3P_0$ optical clock transition in laser-cooled fermionic isotopes of neutral mercury, Phys. Rev. Lett. **101**, 183004 (2008).

[99] C. Zhang, R. Terabayashi, and S. Hasegawa, Investigation of isotope shifts and stark shifts in the strontium rydberg state via $5s^2\,{}^1S_0 \rightarrow 5s5p\,{}^1P_1^0 \rightarrow 5p_{1/2}5p_{1/2} \rightarrow 4d_{3/2}nl_j(n^* = 39.4)$, Spectrochim. Acta, Part B **225**, 107118 (2025).

[100] H. Miyake, N. C. Pisenti, P. K. Elgee, A. Sitaram, and G. K. Campbell, Isotope-shift spectroscopy of the $^1S_0 \rightarrow {}^3P_1$ and $^1S_0 \rightarrow {}^3P_0$ transitions in strontium, Phys. Rev. Res. **1**, 033113 (2019).

[101] M. Athanasakis-Kaklamanakis, S. G. Wilkins, A. A. Breier, and G. Neyens, King-Plot Analysis of Isotope Shifts in Simple Diatomic Molecules, Phys. Rev. X **13**, 011015 (2023).

[102] C. Lyu, C. H. Keitel, and Zoltán Harman, Periodic table for highly charged ions, arXiv:2504.11237.

[103] C. Lyu, C. H. Keitel, and Zoltán Harman, Ultrastable and ultra-accurate clock transitions in open-shell highly charged ions, Commun. Phys. **8**, 3 (2025).

[104] V. A. Dzuba, V. V. Flambaum, and M. G. Kozlov, Combination of the many-body perturbation theory with the configuration-interaction method, Phys. Rev. A **54**, 3948 (1996).

[105] M. G. Kozlov, S. G. Porsev, M. S. Safronova, and I. I. Tupitsyn, CI-MBPT: A package of programs for relativistic atomic calculations based on a method combining configuration interaction and many-body perturbation theory, Comput. Phys. Commun. **195**, 199 (2015).

[106] J. C. Berengut, Particle-hole configuration interaction and many-body perturbation theory: Application to $Hg^+$, Phys. Rev. A **94**, 012502 (2016).

[107] F. Torretti, A. Windberger, A. Ryabtsev, S. Dobrodey, H. Bekker, W. Ubachs, R. Hoekstra, E. V. Kahl, J. C. Berengut, J. R. Crespo López-Urrutia, and O. O. Versolato, Optical spectroscopy of complex open-4*d*-shell ions $Sn^{7+} - Sn^{10+}$, Phys. Rev. A **95**, 042503 (2017).

[108] J. Sugar and C. Corliss, Atomic energy levels of the iron-period elements: Potassium through nickel, J. Phys. Chem. Ref. Data **14** (Suppl. 2), 1 (1985).

[109] F. W. Knollmann, A. N. Patel, and S. Charles Doret, Erratum: Part-per-billion measurement of the $4\,{}^2S_{1/2} \rightarrow 3^2D_{5/2}$ electric-quadrupole-transition isotope shifts between $^{42,44,48}Ca^+$ and $^{40}Ca^+$ [Phys. Rev. A **100**, 022514 (2019)], Phys. Rev. A **107**, 069902(E) (2023).

[110] A. Kramida, Yu. Ralchenko, J. Reader *et al.*, NIST Atomic spectra Database (version 5.11) [online] (2023), https://doi.org/10.18434/T4W30F.

[111] F. G. Kondev and S. Naimi, The AME2016 atomic mass evaluation (I). Evaluation of input data; and adjustment procedures, Chin. Phys. C **41**, 030002 (2017).

[112] F. G. Kondev, and S. and Naimi, The AME2016 atomic mass evaluation (II). Tables, graphs and references, Chin. Phys. C **41**, 030003 (2017).

[113] P. Müller, K. König, P. Imgram, Jörg Krämer, and W. Nörtershäuser, Collinear laser spectroscopy of $Ca^+$: Solving the field-shift puzzle of the $4s^2S_{1/2} \rightarrow 4p^2P_{1/2,3/2}$ transitions, Phys. Rev. Res. **2**, 043351 (2020).

[114] W. Alt, M. Block, V. Schmidt, T. Nakamura, P. Seibert, X. Chu, and G. Werth, Shifts of the $3d$-$4p$ transitions in different isotopes of positive calcium ions, J. Phys. B: At., Mol. Opt. Phys. **30**, L677 (1997).

[115] R. F. Garcia Ruiz, M. L. Bissell, K. Blaum, A. Ekström, N. Frömmgen, G. Hagen, M. Hammen, K. Hebeler, J. D. Holt, G. R. Jansen *et al.*, Unexpectedly large charge radii of neutron-rich calcium isotopes, Nat. Phys. **12**, 594 (2016).

[116] T. Ishiyama, K. Ono, T. Takano, A. Sunaga, and Y. Takahashi, Observation of an inner-shell orbital clock transition in neutral ytterbium atoms, Phys. Rev. Lett. **130**, 153402 (2023).

[117] A.-M. Mårtensson-Pendrill, D. S. Gough, and P. Hannaford, Isotope shifts and hyperfine structure in the 369.4-nm 6s-$6p_{1/2}$ resonance line of singly ionized ytterbium, Phys. Rev. A **49**, 3351 (1994).

[118] R. W. Berends and L. Maleki, Hyperfine structure and isotope shifts of transitions in neutral and singly ionized ytterbium, J. Opt. Soc. Am. B **9**, 332 (1992).

[119] P. E. Atkinson, J. S. Schelfhout, and J. J. McFerran, Hyperfine constants and line separations for the $^1S_0$–$^3P_1$ intercombination line in neutral ytterbium with sub-Doppler resolution, Phys. Rev. A **100**, 042505 (2019).